UNIVERSIDAD AUTONÓMA DE MADRID

FACULTAD DE CIENCIAS

Departamento de Física de la Matería Condensada

Magnetic Force Microscopy study of layered superconductors in vectorial magnetic fields

Memoria presentada por

Alexandre Correa Orellana

para obtener el título de Doctor en Física

Directores:

Dr. Hermann Jesús Suderow

Dr. Carmen Munuera López

Madrid, 2017

Acknowledgements

En primer lugar me gustaría dar las gracias a mis directores de tesis, la Dra. Carmen Munuera y el Dr. Hermann Suderow por depositar en mí la confianza para realizar este trabajo de investigación. Vuestra dedicación, profesionalidad y amplios conocimientos han sido fundamentales para el desarrollo de esta tesis y todo un ejemplo para mí.

Doy las gracias también a la Dra. Isabel Guillamón por todo el tiempo empleado en mi tesis y por su dedicación y paciencia. También me gustaría agradecer las enseñanzas y el apoyo continuado de los Dres. Federico Mompeán, Norbert Nemes y Mar García Hernández.

Doy las gracias al personal del Instituto de Ciencia de Materiales de Madrid (ICMM) y de la Universidad Autónoma de Madrid (UAM). Doy gracias a todos los compañeros con los que he coincidido en el laboratorio, Rafa, Chema, Pepe, Edwin, Víctor, Jon, Antón, Félix, Jesús, Elena, Federico y Roberto.

I would like to thank the Weizmann Institute Collaborators, Dr. Eli Zeldov, Dr. Jonathan Anahory and Dr Lior Embon for their collaboration. I would also like to thank Dr. Kadowaki for providing us with the nice Bi-2212 single crystal measured during the thesis. I would like to thank Dr. Paul Canfield for suggesting us to measure Co doped $CaFe_2As_2$ and helping us to understand what was going on.

Me gustaría agradecer especialmente al Dr. Sebastián Vieira por darme la oportunidad de empezar mi carrera en el mundo científico hace 5 años.

Por último, me gustaría agradecer a los proyectos de investigación Anisometric

permanent hybrid magnets based on inexpensive and non-critical materials (AMPHIBIAN) (Ref. NMBP-03-2016) y Graphene Flagship (Grant No. 604391) financiados por la Unión Europea, gracias a los cuales he podido realizar mi tesis doctoral.

Abstract

This thesis is focused on the set-up and use of a cryogenic magnetic force microscope (MFM) in a three axis vector magnet. We have studied superconducting layered and quasi-two dimensional compounds. In particular, we address the superconducting properties of graphene deposited on an isotropic s-wave superconductor $\beta-Bi_2Pd$, of a layered cuprate superconductor ($BiSr_2CaCu_2O_8$), of a layered iron based material ($Ca(Fe_{0.965}Co_{0.035})_2As_2$) and of the s-wave superconductor $\beta-Bi_2Pd$.

MFM measures the magnetic properties of a surface by tracing the force when a magnetic tip is scanned over a magnetic sample. The interaction is mutual, the tip feels the magnetic properties of the sample and viceversa. By adjusting the scanning height, we can go from a non-invasive situation to manipulation, very much the same as in atomic manipulation using a STM. Here, in a MFM, the objects that are usually studied are much larger than atoms. Magnetic interactions usually extend over larger distances and therefore often the spatial resolution is of the order of the nm or above. This tool is ideal to study the magnetic profile generated by superconductors in the mixed state. Abrikosov vortices have a magnetic shape that is determined by the penetration depth, which is most often well above the nm range.

Here we are interested in the properties specific to two-dimensional and quasi two-dimensional superconducting systems. The associated confinement of superconductivity brings about new aspects. An important one is that, in the limit of extremely thin samples, the penetration depth often diverges. This makes the MFM useless to identify vortices or study magnetic textures, because the magnetic contrast decreases accordingly. Thus, instead of using single layers, we have focused on layered superconductors and hybrid structures combining a bulk superconductor with a 2D system

as graphene. Another important aspect is that vortices are no longer lines of magnetic flux but disks. This implies that their mobility and pinning properties change considerably. Also, highly anisotropic properties can produce structural transitions, which are often of first order and can lead to coexistence of superconducting and normal domains. The MFM is there an ideal tool, with which we can make combined magnetic and structural studies, the latter by measuring the non-magnetic interaction between tip and sample, and making Atomic Force Microscopy (AFM). Finally, interactions might induce novel p-wave or unconventional superconducting states. This has been a recent focus, with the discovery of Majorana end states in proximity induced small superconducting structures. The spectroscopic features of such structures are well addressed in literature and it is generally acknowledged that studying the magnetic textures is the next important step. By inducing superconductivity in graphene, we have searched for unconventional behavior.

In the third chapter of the thesis, we have focused on the exfoliation and deposition of layered superconductors and on the study of graphene/superconductor interfaces. 2D superconductivity in thin films and crystal flakes has attracted the attention of many researchers in the last decade [1–9]. For example, superconducting crystals like BSCCO or TaS_2 have been successfully exfoliated down to a single layer and deposited in a substrate in the past [10–12]. In addition, a lot of work has been done trying to induce superconductivity in graphene in contact with a superconductor due to the proximity effect [1, 2, 13–17]. In this thesis, we have measured the magnetic profile of a Bi-2212 flake below the superconducting transition, developed an experimental procedure to localize graphene flakes deposited on top of a β-Bi_2Pd single crystal and demonstrated the possibility to depositing thin flakes of the β-Bi_2Pd superconductor on a substrate.

The vortex distribution in a superconductor at very low fields is still an open debate in the scientific community. For example, bitter decoration experiments performed in the single gap, low-κ superconductor, Nb, shows areas where flux expulsion coexists with regions showing a vortex lattice. Moreover, Scanning Hall Microscopy experiments have shown vortex chains and clusters in ZrB_{12} ($0.8<\kappa<1.12$) at very low fields [18]. Both experiments were explained with the existence of an attractive

term in the vortex-vortex interaction in superconductors with $\kappa < 1.5$. This regime is known as the *Intermediate Mixed State*. On the other hand, the existence of vortex free areas between cluster and stripes of vortices at very low fields was also reported in the multigap superconductor MgB_2 [19–21]. In this case, the authors propose that this behavior corresponds to a new state that they called *type 1.5 superconductivity*, due to the existence of two different values of the Ginzburg-Landau parameter, κ, for the two gaps of the compound. In addition, a recent theoretical work has also proposed that pinning may have an important role in the formation of the vortex patterns in MgB_2 [22]. Comparatively, $\beta-Bi_2Pd$ has a small, yet sizable, value of $\kappa \approx 6$. It has very weak pinning and is a single gap isotropic superconductor [23–25]. This allows us to characterize the vortex distribution at very low fields in a material with only one gap and a moderate value of κ for the first time. We have found vortex clusters and stripes as in the case of low-κ or multigap superconductors. But, in this case, they are associated with local changes in the value of the penetration depth of the superconductor. We have also measured the vortex lattice at low temperatures of a β-Bi_2Pd single crystal with a graphene sheet deposited on top and found that the penetration depth increases, particularly at steps and wrinkles of the graphene surface. These results are presented in chapter 4.

$Ca(Fe_{0.965}Co_0.035)_2As_2$ is an iron based compound with extremely high sensitivity to pressure and strain. Due to the presence of Ca ions, small pressures result in dramatic changes in the ground state of the system. We have characterized the formation of alternating superconducting antiferromagnetic domains at low temperatures and related them with the separation of the material in two structural phases. The results are collected in chapter 5.

In the last chapter of the thesis, we focus on the local manipulation of superconducting vortices in the high-temperature cuprate superconductor $BiSr_2CaCu_2O_8$. It has a two-dimensional layered structure, with superconductivity taking place in the copper oxide planes. When a magnetic field is applied tilted with respect to the c crystallographic axis, the vortex lattice decomposes into two systems of vortices, perpendicular to each other. There are Josephson, coreless vortices parallel to the layers and Abrikosov vortices located in the copper oxide planes, called pancake vortices. In

our work, we use the MFM tip to manipulate pancake vortices at low temperatures and have determined the force needed to move combined pancake and Josephson vortex lattices.

Contents

CHAPTER 1

Introduction

1.1 Historical remarks

Superconductivity was first discovered by H. K. Onnes in 1911 [26] after he was able to liquefy He in his laboratory in 1908 opening a new branch in physics, the *low temperature physics*. Onnes expected a gradual approach of the resistivity to zero with decreasing the temperature, however he found that the resistance of Hg dropped to zero below 4.15 K. Onnes realized that he had found a new state of the matter characterized by zero resistivity, the *superconductivity*. One year later he also discovered that applying a strong magnetic field to superconducting Hg, the normal state was recovered. In the following years new superconducting materials were discovered: Pb, Nb etc. In 1933 Meissner and Ochsenfeld found that if a superconductor material is cooled down below its transition temperature, it expels any external magnetic field below a certain value called the *critical magnetic field*, H_C, [27]. This effect is called nowadays the *Meissner state*. Later, superconductors where the magnetic field can penetrate the material without loosing

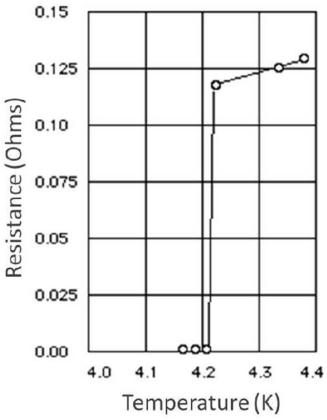

Figure 1.1: K. Onnes original measurement of the superconducting transition in Hg.

the zero resistivity were discovered and superconducting materials were split in two categories, type I and type II superconductors.

Type I superconductors present zero resistivity and perfect diamagnetism below T_C and H_C. Type II superconductors present zero resistivity below T_C and the *upper magnetic critical field*, H_{C2}, but only perfect diamagnetism below the *lower magnetic critical field*, H_{C1}. Between H_{C1} and H_{C2}, the magnetic field penetrates the material in form of magnetic vortices that carry one single magnetic quantum flux, $\phi_0 = 2.067 \cdot 10^{-15}$ Wb. This regime is called the *mixed state*. For more details see references [28, 29].

1.2 Superconducting theories

These discoveries prompted the London brothers to propose the first phenomenological theory in 1935 [30]. In 1950 a new superconducting theory was developed, the Ginzburg-Landau theory [31]. It describes the superconductivity in terms of an order parameter. Then, Bardeen Cooper and Schrieffer proposed the BCS theory, which provides a microscopic explanation of superconductivity. [32].

1.2.1 Ginzburg-Landau Theory

Ginzburg and Landau assumed that close to the transition temperature the Gibbs free energy density can be expanded as function of a complex parameter, $\psi = |\psi| e^{i\theta}$ as [31]:

$$G_S = G_N + a|\psi|^2 + \frac{b}{2}|\psi|^4 + \frac{1}{2m^*}\left|(i\hbar\nabla - e^*\vec{A})\psi\right| \tag{1.1}$$

$m^* = 2m_e$ and $e^* = 2e$ are the superelectron mass and charge (m_e and e, are the electron mass and charge. As we will see later, superconductivity occurs in the form of pairs of electrons, called Cooper pairs), $\vec{A}$ the vector potential and a and b parameters only dependent of the temperature with values $a \approx a_0[T/T_C - 1]$ and $b \approx b_0$ near T_C.

The square of the order parameter is the superconducting electron density, n_s. The order parameter ψ is zero above T_C and increases as the temperature decreases below T_C. Taking the derivative of equation 1.1 with respect to the order parameter they found what is now called the *first G-L equation*:

$$\frac{1}{2m^*}(i\hbar^2\nabla^2\psi - 2i\hbar e^*\vec{A}\cdot\nabla\psi - e^{*2}\vec{A}^2\psi) - a\psi - b|\psi|^2\psi = 0 \tag{1.2}$$

The free energy is also a minimum with respect to to the vector potential $\vec{A}$. Taking the derivative of G_S with respect to $\vec{A}$, we obtain the *second G-L equation*:

$$\nabla\times(\nabla\times\vec{A}) + \frac{i\hbar e^*}{2m^*}(\psi^*\nabla\psi - \psi\nabla\psi^*) + \frac{e^{*2}}{m^*}\vec{A}|\psi|^2 = 0 \tag{1.3}$$

The G-L equations can be used to calculate the two principal length scales in a superconductor as we will introduce in the following.

1.2.1.1 Coherence length

Let us now study the following case: a semiinfinite superconductor from $x = 0$ to $x = \infty$ and a normal metal from $x = -\infty$ to x=0. Setting $\vec{A} = 0$ in the first G-L equation we obtain:

$$-\frac{\hbar^2}{2m^*}\nabla^2\psi + a\psi + b|\psi|^2\psi = 0 \tag{1.4}$$

Since the phase, θ of the order parameter is arbitrary, we can take ψ real ($\theta = 0$) and therefore, $\psi = \psi(x)$. Now, we can simplify the equation 1.4 to the one dimensional case:

$$-\frac{\hbar^2}{2m^*}\frac{d\psi^2}{dx^2} + a\psi + b|\psi|^2\psi = 0 \tag{1.5}$$

which has the solution:

$$\psi = \psi_\infty tanh \frac{x}{\sqrt{2\xi}} \tag{1.6}$$

where ξ is a characteristic length of ψ. ξ is called the *coherence length* and is one of the two main parameters of the G-L theory. The order parameter ψ is zero inside the normal material and increases up to ψ_∞ over length scale of ξ in the superconducting material.

1.2.1.2 Penetration depth

Now, we will consider the same semi-infinite geometry than in the previous section but with a homogeneous magnetic field in the Z direction, which has a vector potential $\vec{A} = A_y(x)$.

Substituting in the second G-L equation, we find:

$$\frac{d^2 A_y(x)}{dx^2} = \frac{\mu_0 e^{*2} |\psi|^2}{m^*} A_y(x) \tag{1.7}$$

and the solution for the vector potential inside the superconductor is:

$$A_y(x) = A_0 e^{(-x/\lambda)} x \tag{1.8}$$

And therefore:

$$B_z(x) = B_0 e^{(-x/\lambda)} \tag{1.9}$$

where A_0 and B_0 are constants and λ is the *penetration depth*, the second characteristic length of the G-L theory. It represents the distance in which an external magnetic field decreases inside the superconductor a factor e^{-1}.

1.2.1.3 Type I and type II superconductors

Using the two characteristic lengths of the G-L theory, one can define the dimensionless quantity:

$$\kappa = \frac{\lambda}{\xi} \tag{1.10}$$

which is called the *G-L parameter*. Values of $\kappa < 1/\sqrt{2}$ and $\kappa > 1/\sqrt{2}$, separate the G-L equations in two different branches of solutions. For $\kappa < 1/\sqrt{2}$ the energy difference between a normal and a superconducting domain is positive and for $\kappa > 1/\sqrt{2}$ it is negative which means that for the superconductor becomes favorable the formation of many small superconducting and normal domains [28].

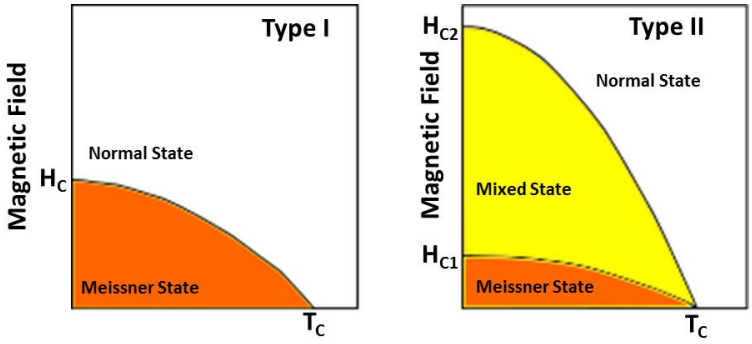

Figure 1.2: Phase diagram for type I (left) and type II (right) superconductors. In orange, the region presenting Meissner state. In white, the normal region. In yellow, the mixed state region.

Solving the G-L equations for $\kappa < 1/\sqrt{2}$ the B-T phase diagram for type I superconductors is found. In this phase diagram, there are only two regions, normal and Meissner state, separated by the critical field, with a dependence of the temperature following:

$$B_C(T) = B_C(0)[1 - \left(\frac{T}{T_C}\right)^2] \tag{1.11}$$

For $\kappa > 1/\sqrt{2}$ a B-T phase diagram with three regions is found. The phase diagram is separated in normal state, Meissner state and mixed state. The two first regions

are analogous to the regions in type I superconductors and the mixed state is a region where the magnetic flux is allowed to enter into the superconductor material in form of superconducting vortices that carry a magnetic flux ϕ_0. Vortices are singularities where the order parameter is suppressed and the material is in the normal state. The three areas of the phase diagram are separated by two critical fields, with values at zero temperature of:

$$B_{C1}(0) = \frac{\phi_0}{4\pi\lambda^2} ln(\kappa) \tag{1.12}$$

$$B_{C2}(0) = \frac{\phi_0}{2\pi\xi^2} \tag{1.13}$$

Both phase diagrams are schematized in the figure 1.2.

1.2.1.4 Vortex lattice

As we mention in the previous section, in type II superconductors, above a certain value, the magnetic field is not fully expelled from the superconducting material. It penetrates in form of magnetic vortices.

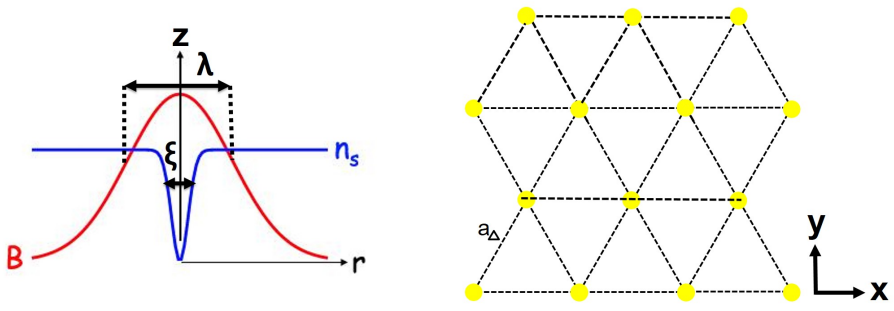

Figure 1.3: In the left panel, an scheme of the superconducting density of states (blue) and the magnetic field (red) inside a superconducting vortex. The center of the vortex is located at the center of coordinates in the scheme. In the right panel, an schematic representation of the Abrikosov vortex lattice of SC vortices with a lattice parameter $a_\triangle$. SC vortices are represented as yellow circles. The lattice is schematized with dashed black lines.

Superconducting vortices are characterized by two length scales. The first one is named ξ and provides the changes as a function of the position of the parameter ψ, which is in turn related to the superconducting density of states through microscopic theory. The vortex consists of a core region of 2ξ width where n_S is zero at the center and increases until it reaches a finite value outside this region. The other length scale is the magnetic penetration depth, λ. The magnetic field radially decreases from the center at a length scale of λ. The magnetic field is maximum at the center of the vortex. Currents flow in circular paths around the around the vortex core. Both spatial dependence of the vortex structures are shown in figure 1.3.

Vortices have a repulsive interaction between them and arrange in a hexagonal lattice called the Abrikosov lattice after Aleksei Abrikosov who first proposed the existence of superconducting vortices in type II superconductors [33]. The parameter of the vortex lattice is:

$$a_{\triangle} = 1.075\sqrt{\phi_0/B} \tag{1.14}$$

which is only dependent in the value of the magnetic field. A schematic representation of the vortex lattice is shown in figure 1.3.

1.2.2 BCS theory

In 1956, Cooper demonstrated that the normal ground state of an electron gas is unstable with respect the formation of bound electron pairs [34]. Cooper, developed his theory following an original idea of Fröhlich [35]. Fröhlich argued that an electron moving across a crystal lattice, due to its negative charge will attract the positive ions in the lattice. In the surroundings of the electron, there will be an accumulation of positive charge, changing locally the density of charge in the lattice and exciting a phonon. If a second electron is near this perturbation, it will be attracted by it absorbing a phonon (figure 1.4). Cooper considered a pair of electrons near the Fermi level whose attraction due to the phonon interaction was greater that the Coulomb repulsion, creating a bound state between both electrons. The attraction is maximum

when the momentum of the electrons is equal and has opposite sign ($\vec{k_1} = -\vec{k_2}$), the resulting cooper pair has momentum and spin equals to zero.

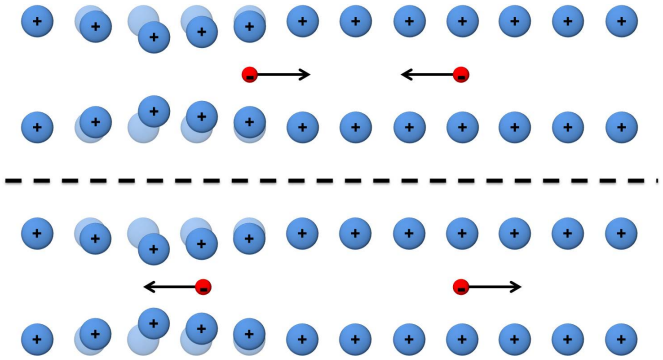

Figure 1.4: Scheme of the phonon mediated pairing of Cooper pairs. The atomic cores are represented with blue circles and the electrons with red circles. The direction of the movement of the electrons is schematized by a black arrow. The movement of the atomic lattice is represented by transparent circles. In the upper panel, an electron coming from the left, slightly distorts the atomic lattice. In the lower panel, another electron coming from the right is attracted by the accumulation of positive charge at the distortion.

One year later, J. Bardeen, L. N. Cooper y J. R. Schrieffer presented the basis of their new microscopic theory of superconductivity [32]. A theory that nowadays is known as the BCS theory. This state is described in the BCS theory with a macroscopic wave function that keeps the phase coherence a distance equal to the coherence length ξ.

1.2.2.1 Superconducting gap

Forming Cooper pairs, decreases the energy of the system a quantity equal to the energy of the bonding between electrons in the pair, 2Δ. In the ground state, Cooper pairs are condensed in a state with an energy Δ below the Fermi level and the first excited state has an energy Δ above the Fermi level. Δ is know as the superconducting gap.

1.3 Intermediate and Intermediate Mixed States

As it was presented before, below H_C (Type I SC) or H_{C1} (Type II SC) no magnetic field penetration is expected. Below this critical field, both types of superconductors should behave as perfect diamagnets. But, some works have reported flux penetration below H_C in type I SCs [36, 37] and below H_{C1} in type II SCs [19–21, 37–40]. This behaviour can be explained as a *intermediate state* (IS) in type I SCs and a *intermediate mixed state* (IMS) in type II SCs.

1.3.1 Intermediate State

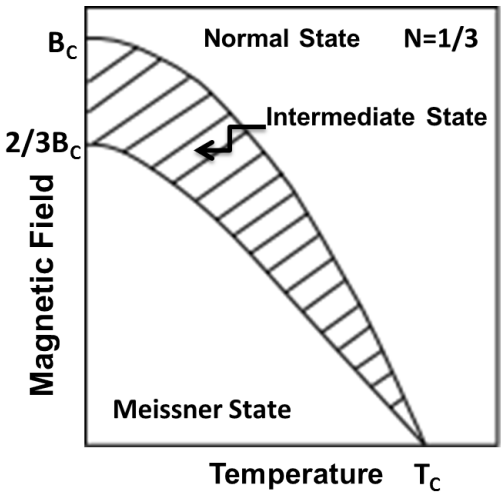

Figure 1.5: B-T phase diagram of a type I superconducting sphere. The curve B=2/3B$_C(T)$ separates the Meissner from the IS. The region where the IS takes places is dashed.

Let us consider the case of a type I superconducting sphere (demagnetization factor, N=1/3) in the presence of an external magnetic field in the Z direction. Below T_C, the magnetic field at the surface of the sphere is:

$$B_{surface} = \frac{3}{2} B_a sin\Theta \tag{1.15}$$

where B_a is the external magnetic field and Θ the polar angle in spherical coordinates. If the external magnetic field is lower than 2/3B$_C$, the surface field will be

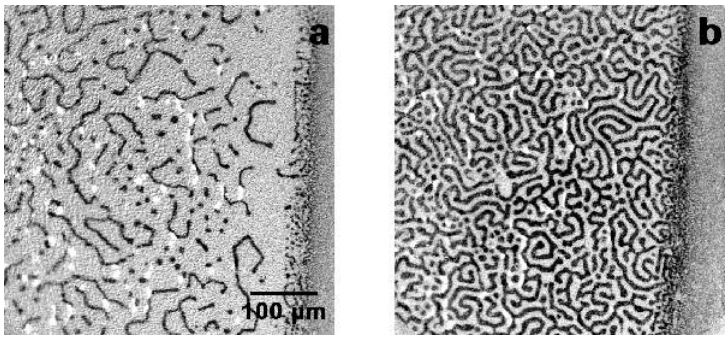

Figure 1.6: Typical IS patterns in an In sample with thickness d= 10μ m for increasing values of the applied magnetic field. Images a and b, correspond to h=0.105 and h=0.345, respectively (h=H/H_C) at $T = 1.85$ K. SC domains are represented in black and have circular or lamellar shapes. The edge of the sample is along the right edge of the image. Adapted from [41]

lower than B_C in all the surface, and the sphere will remain in the superconducting state. But, if the external magnetic field is greater than $2/3B_C$, from equation 1.15, there will be a range of angles where the surface field will exceed B_C and the sphere can not remain in the perfect superconducting state. In the range of external magnetic fields:

$$\frac{2}{3}B_C < B_a < B_C \tag{1.16}$$

The surface must decompose into superconducting and normal regions that keep the internal field below the critical value H_C in the superconducting regions at zero and in the normal regions at Hc. This state is known as the *intermediate state* (IS). The trigger of this state is the inhomogeneous distribution of the magnetic field on the surface due to the demagnetization factor of the samples. A scheme of the phase diagram for a superconducting sphere is shown in figure 1.5, where the dashed area represents the region where the IS takes place. The IS was observed in various type I superconductors in form of tongues or alternative domains of Meissner and normal states [36, 37, 41] (figure 1.6).

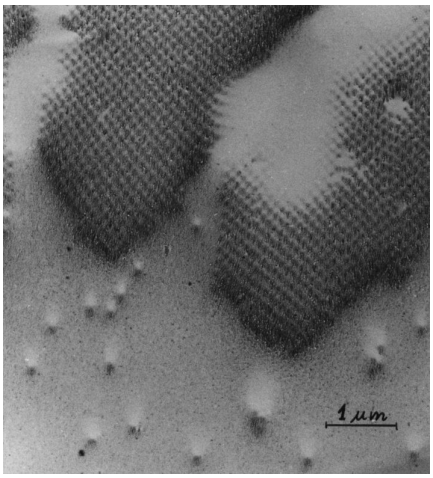

Figure 1.7: Magnetic decoration of a square disk 5 × 5 × 1 mm^3 of high purity polycrystalline Nb at 1.2 K and 1100 Oe, showing domains of Meissner and mixed states. Magnetic flux penetrates from the edges in form of fingers which are composed of vortex lattice. Adapted from [40].

1.3.2 Intermediate Mixed State

Following the same arguments than for type I SC, if a magnetic field is applied to a type II superconductor, at certain fields below B_{C1}, the SC will decompose in domains in the Meissner state and domains in the mixed state, depending on its demagnetization factor [37]. This regime is called the *intermediate mixed state* (IMS). Experimentally it was found that the intervortex distance in the IMS domains corresponds to the expected value corresponding to the inductance B_{C1} in equation 1.14. It was also found that the area occupied by the domains with zero induction decreases linearly with the magnetic field, to reach B_{C1} when entering the mixed phase [37]. An example of the IMS in a type II superconductor is presented in figure 1.7 where the magnetic flux penetrates into the Nb forming domains in the Meissner states and domains with a regular vortex lattice with $a_{\triangle} = 1.075\sqrt{\phi_0/B_{C1}}$, independent of the magnetic field.

1.4 Anisotropic Superconductors

In anisotropic superconductors, the electronic properties depend on the direction of the space and new considerations have to be taken into account in order to understand their behaviour. For example, in cuprates, Cooper pairs and vortices are confined into 2D copper oxide planes [42–48]. The penetration depth and the coherence length have to be separated in two components, one parallel ($\xi_{\parallel}$ and $\lambda_{\parallel}$) and perpendicular ($\xi_{\perp}$ and $\lambda_{\perp}$) to the superconducting planes [42, 43, 45]. Then, we can define the anisotropy factor, $\gamma = \xi_{\parallel}/\xi_{\perp} = \lambda_{\perp}/\lambda_{\parallel}$. We can also define the upper and lower critical fields for magnetic fields applied parallel or perpenticular to the CuO planes as:

$$B_{C1}(0) = \frac{\phi_0}{4\pi\lambda_{\parallel}\lambda_{\perp}} ln(\kappa_{\parallel}) \tag{1.17}$$

$$B_{C2}(0) = \frac{\phi_0}{2\pi\xi_{\parallel}\xi_{\perp}} \tag{1.18}$$

If the magnetic field is applied parallel to the CuO planes. And:

$$B_{C1}(0) = \frac{\phi_0}{4\pi\lambda_{\parallel}^2} ln(\kappa_{\perp}) \tag{1.19}$$

$$B_{C2}(0) = \frac{\phi_0}{2\pi\xi_{\parallel}^2} \tag{1.20}$$

If the magnetic field is applied perpendicular to the CuO planes. Where $\kappa_{\parallel} = \|\frac{\lambda_{\parallel}\lambda_{\perp}}{\xi_{\parallel}\xi_{\perp}}\|^{1/2}$ and $\kappa_{\perp} = \lambda_{\parallel}/\xi_{\perp}$ [29].

In highly anisotropic layered superconductors like BSCCO, when a magnetic field is applied perpendicular to the superconducting planes, it penetrates the material in form of stacks of 2D vortices in the CuO planes, called pancake vortices (PVs). If the magnetic field is applied parallel to the CuO planes, it penetrates the superconductor parallel to the CuO planes in form of Josephson vortices (JVs) [46][49].

1.4.1 Pancake vortices

In BSCCO and other highly anisotropic superconductors, the CuO planes are separated in the c-axis direction a distance $s > \xi_\perp$ and therefore they act as Josephson junctions [44–48]. A vortex perpendicular to these layers, which otherwise would be considered a uniform cylinder of confined flux, is here a stacking of 2D pancake shaped vortices (PVs), one PV per layer with surrounding currents confined to the layer [42, 50–53]. PVs are so weakly coupled that thermal agitation can decouple the stack of PVs [54]. A scheme of PVs in different layers of a highly anisotropic superconductor is presented in figure 1.8.

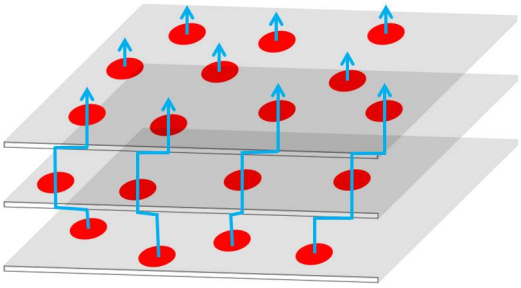

Figure 1.8: Stack of 2D pancake vortices in a layered superconductor. Red circles represents the 2D PVs while blue lines are a guide to the eye to connect the PVs at different layers (grey planes).

1.4.2 Josephson vortices

In the case of an applied magnetic field parallel to the superconducting planes, the field penetrates in highly anisotropic superconductors in form of Josephson vortices (JVs) [48]. JVs do not have normal cores and their current distribution makes rather wide loops between between two superconducting layers [46, 48]. The structure of the core is similar to the structure of the phase drop across a flux line in two-dimensional Josephson junctions, where the phase difference changes 2π between the two layers over a distance of Λ_J [48]. For 3D superconductors, this length is given by $\Lambda_J = \gamma s$, and we can think of a central region of γs wide and s high as the core of the JV [48] (figure 1.9). Beyond this core, the screening of the z-axis currents is weaker than by in-plane currents, and the flux line is stretched into and ellipsoidal shape with a large

width ($\lambda_\perp$) along the layers. A scheme of a JV is shown in figure 1.9.

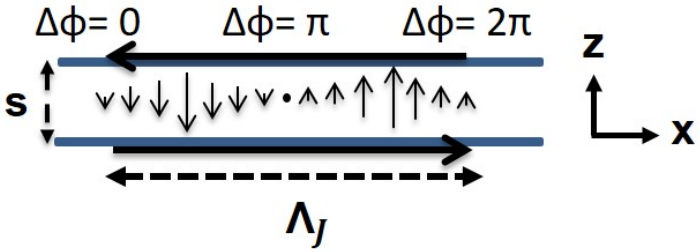

Figure 1.9: Scheme of a JV in a layered superconductor with the in plane magnetic field applied in the Y-direction. The Josephson vortex is also oriented along the Y-direction. Horizontal blue lines represents the SC planes and the black arrows the Josephson currents (vertical) and the supercurrents (horizontal) resulting from the JV. The phase difference between the SC planes is summarized in the upper part of the image. The phase difference changes 2π between the two layers over a distance of $\Lambda_J = \gamma s$, where γ is the anisotropy factor and s is the distance between CuO planes.

Under an applied magnetic field parallel to the CuO planes, in the Y direction, JVs arrange in a strongly stretched triangular lattice along the direction of the layers with lattice parameters [48]:

$$a_z = \sqrt{2\phi_0/\sqrt{3}\gamma B_y} \tag{1.21}$$

$$a_x = \sqrt{\sqrt{3}\gamma\phi_0/2B_y} \tag{1.22}$$

1.4.3 Crossing lattice

A huge variety of vortex configurations have been proposed when applying magnetic field tilted with respect the c axis in highly anisotropic superconductors [44, 46, 47, 49, 55]. We will focus in the crossing lattices of PVs and JVs. In this configuration, the JVs interact with the stacks of PVs splitting them in two branches giving a zig-zag like structure perpendicular to the CuO planes [44, 46, 47, 49].

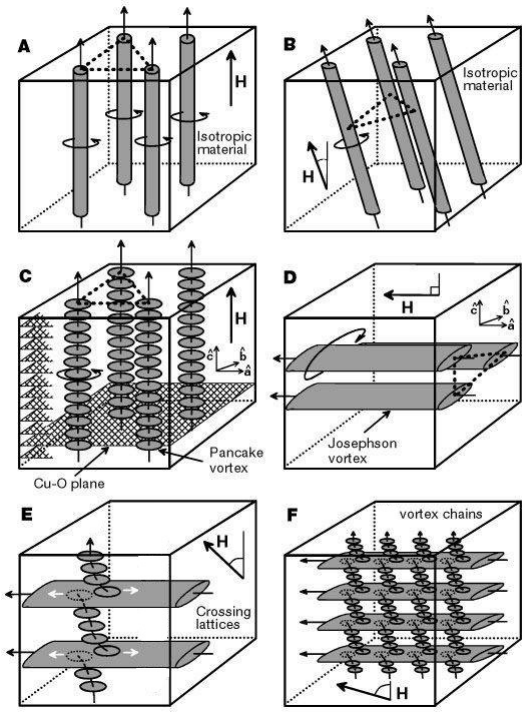

Figure 1.10: Vortices in isotropic and highly anisotropic superconductors. In a and b, the vortex lattice in an isotropic superconductor where the repulsion between vortices leads to the formation of hexagonal lattice. Curved arrows indicate circulating supercurrents around the vortex core. In c, hexagonal ordering of the vortex lattice in layered superconductors with the magnetic field applied along the c axis. In this case, vortices are formed of vertical stacks of 2D PVs situated in the CuO planes. In d, with the magnetic field parallel to the layers, crystalline anisotropy leads to the formation of elliptical JVs. In e, tilted vortices spontaneously decompose into coexisting orthogonal PVs and JVs. Where a PV stack intersects a JV stack, small PV displacements (indicated by white arrows) driven by the JV supercurrents lead to an attractive interaction. In f, the vortex chain state when all PVs stacks become trapped on vertical stacks of JVs. Adapted from [56].

A JV in the Y direction between two superconducting layers carries a current with opposite sign in the two layers ($\pm J$). The current interacts with the stack of PVs in the Z direction with a Lorenz force $+F_y$ and $-F_y$ in the two different superconductor layers. As a result the PV stack is displaced a distance $+a$ and $-a$ in the two planes in the direction of the JV, causing a zig-zag like structure in the PV stack [44, 46, 47, 49], as is represented in figure 1.10 e and f. The amplitude of the distortion has been extensively studied by [46], finding that the maximum pancake

displacement at the JV core position is:

$$a \approx \frac{2.2\lambda_{\parallel}}{\gamma s log(2\gamma s/\lambda_{\parallel})} \tag{1.23}$$

The distorted PV stack crossing a JV have less energy compared with other stacks, which makes favourable to add an extra stack on top of the JV and form PV rows along the JV [44] separated a distance[57]:

$$d \approx 2\lambda_{\parallel} log \frac{B_{\parallel}\gamma^2 s^2}{\phi_0 \lambda_{\parallel}} \tag{1.24}$$

The existence of PVs rows decorating JVs have been confirmed in previous experimental works using scanning hall probe microscopy (note that this technique is non-invasive, vortices can not be moved using a scanning hall probe microscope [58–65]).

The crossing lattice of PVs and JVs causes a rearrangement of the phase distribution on the CuO planes and therefore in the JV structure. In an isolated JV in the Y direction, the phase difference, $\Delta\phi = \phi_1 - \phi_0$ (ϕ_1 and ϕ_0 are the phases at both CuO planes), between the top and bottom CuO planes changes by 2π over a distance Λ_J in the X direction. The phase difference is 0 and 2π at the edges and π at the centre of the JV (figure 1.11 b). Adding one PV in each layer, separated by an in-plane distance $2a$ in the Y direction, causes a change in the phase in each CuO plane. The phase changes by π between the extremes of the line that crosses a PV parallel to the JV. The phase changes by π in both layers at different positions, creating a narrow region, $2a$ width, where the phase difference between CuO layers is 2π instead of π in the centre of the JV [46] (figure 1.11 c).

1.5 Iron Based Superconductors

Iron based superconductors (FeBSC) were first discovered by Kamihara et al. in 2006 [66]. They found that LaFePO transits to a superconducting state below 4 K.

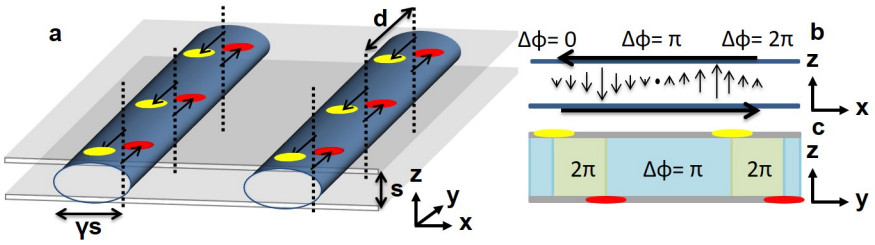

Figure 1.11: In a, we schematically describe PVs and JVs crossing lattice. The ellipse signals a Josephson vortex and the circles pancake vortices pinned to it. The relevant approximate length scales, such as JVs size and distance between pancake vortices is also shown. In b, we show a two dimensional scheme of the Josephson currents and phase difference in a JV. In c, blue areas represents areas where $\Delta\phi = \pi$ and green areas where $\Delta\phi = 2\pi$ as a consequence of the PVs displacement.

Two years later, they found superconductivity in $LaFeAsO_{1-x}F_x$ with a T_C of 26 K [67]. Fe is a well known magnetic material and magnetism was thought to damage superconductivity. Actually, magnetism and superconductivity are considered as competing states. For this reason, finding superconductors containing Fe was a big surprise. Moreover, as in the case of cuprates superconductors, the BCS phonon-mediated coupling was not able to explain the formation of Cooper pairs in these superconductors. Before 2008, the term *high-temperature superconductivity* (HTS) was reserved for the cuprates. Now the term HTS equally applies to both cuprates and FeBSC.

Among the FeBSCs, the 122 family has attracted a lot of attention in the last years. Specially the compounds derived from $BaFe_2As_2$ and $CaFe_2As_2$. Nematicity for instance, was first reported in a STM study of Co doped $CaFe_2As_2$ [69]. Nematicity is a peculiar electronic phenomenon, characterized by the formation of a uniaxial anisotropy within the FeAs planes. The anisotropy usually comes together with a structural transition. However, the modification in the structure is too small to explain the large electronic in-plane anisotropy found in different experiments. Therefore, it is thought that this is a different electronic state. Nematicity appears often in connection to high temperature superconductivity in the iron based compounds. The electronic nature of this state was studied performing resistivity measurements on detwinned single crystals of Co doped $BaFe_2As_2$ in [70]. Recently, strain induced phase

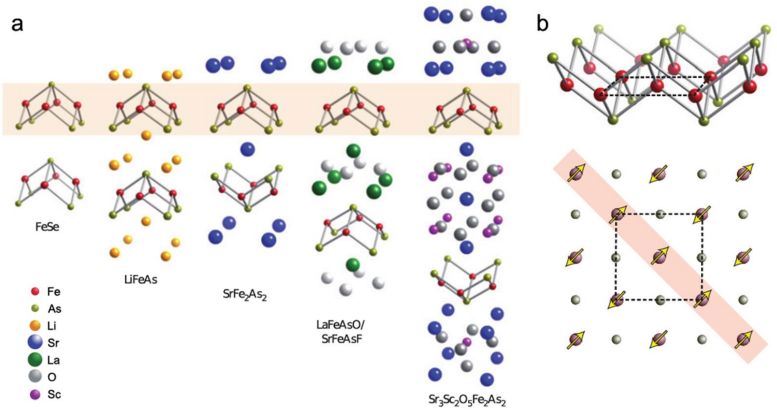

Figure 1.12: In a, crystal structure of different families of iron pnictides. Fe-As planes are highlighted as common features in all structures. In b, the FeAs plane from a frontal (top) and upper (bottom) point of view. Spins are aligned ferro and antiferromagnetic alternately in a structure called stripe like antiferromagnetic order. Adapted from [68].

separation between superconducting tetragonal domains and non-superconducting orthogonal domains was proposed in [71] in Co doped $CaFe_2As_2$.

FeBSC are also promising compounds to the study of superconductivity in the 2D limit. In FeBSC, superconductivity has its origin in the 2D Fe-As layers, similar to the CuO planes in the cuprates.

1.5.1 Phase diagram

FeBSC have 2D lattices of 3d transition metal ions as the building block, sitting in a quasi-ionic framework composed of rare earth, oxygen, alkali or alkaline earth blocking layers. They present phase diagrams with a magnetic ordered phase in the parent compound and a superconducting dome developing with doping. They also present orthorhombic transition at small doping.

Some compounds, for instance, LaFeAsO, shows first order transition between magnetic and superconducting phases and in other compounds like the 122 family, both states coexist for certain doping levels. FeBSC magnetic phases are metallic with linear dependence of the resistivity with the temperature. They also show a

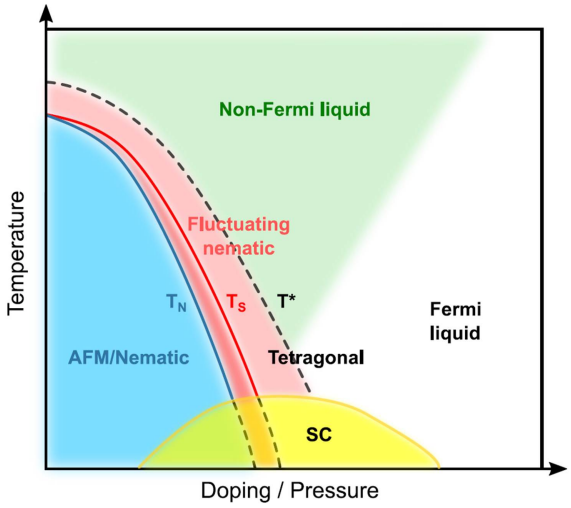

Figure 1.13: Generic temperature versus doping/pressure phase diagram for the FeBSC. The parent compound usually presents a structural/magnetic transition that reduces its temperature with increasing doping/pressure. The structural and magnetic transitions are coupled or separated depending on the compound. Above the structural transition and usually coupled to it and to the magnetic one there is an electronic nematic phase. Superconductivity emerges in a dome-shape with finite doping/pressure with the optimal doping usually coinciding with the extrapolation of the magnetic phase to zero temperature. Adapted from [72].

structural phase transition which is often coupled with the magnetic transition. Above them, the above mentioned nematic behavior has been reported in some compounds. Superconductivity emerges as a dome at finite doping levels with the optimal doping level located where the magnetic transition extrapolates to zero temperature. For some materials there is a region where magnetism and superconductivity coexist. A schematic representation of the generic phase diagram of FeBSC is presented in figure 1.13.

1.5.1.1 Electronic structure

The Fermi Surface (FS) of FeBSC is derived from the d_{xy}, d_{yz} and d_{xz} orbitals of Fe and the out of plane orbital of the As, with which Fe is in tetrahedral coordination in a 2D layer (figure 1.12).

The electronic band structure has been calculated using the local density approx-

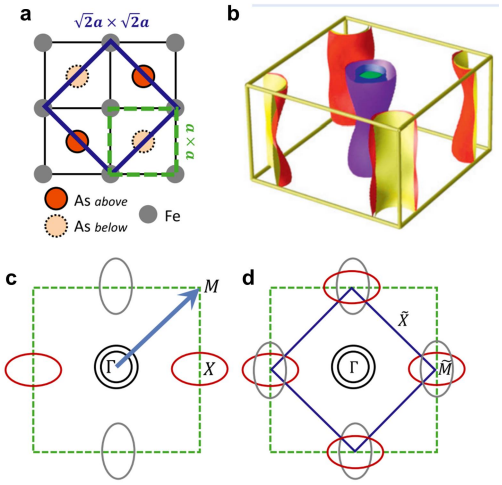

Figure 1.14: In a, FeAs lattice indicating As above and below the Fe plane. Dashed green and solid blue squares indicate 1- and 2-Fe unit cells, respectively. In b, FSs of $BaFe_2As_2$ with 10% substitution of Co, calculated using DFT using experimental atomic positions and drawn using the folded BZ representation with two Fe per unit cell. In c, schematic 2D Fermi surface in the 1-Fe BZ whose boundaries are indicated by a green dashed square. The arrow indicates folding wave vector QF. In d, Fermi sheets in the folded BZ whose boundaries are now shown by a solid blue square. Adapted from [73] and [74].

imation [75], showing that the electronic properties are dominated by five Fe d states at the Fermi energy, with a FS consisting of at least four quasi-2D electron and hole cylinders. These consist of two hole pockets centred at the Brillouin zone (BZ) centre and two electron pockets centred at $(0,\pm\pi)$ and $(\pm\pi,0)$ in the tetragonal unit cell (figure 1.14 c). Two non-equivalent As positions result in the folding of the BZ to include two Fe atoms per unit cell and to put the electron pockets at $(\pm\pi,\pm\pi)$ as shown in figure 1.14 d. A fifth hole band is also proposed to sit at $(0,\pm\pi)$ in the folded BZ, and its presence may be very sensitive to structural details [76].

1.5.1.2 Magnetism

The electronic structure suggests that the same magnetic interactions that drive the antiferromagnetic (AFM) ordering also produce the pairing interaction for superconductivity [73]. As predicted before experiments [77], AFM order in all FeAs-based

superconducting systems is found to have a wave vector directed along (π,π) in the tetragonal unit cell with a real-space spin arrangement consisting of AFM stripes along one direction of the Fe sublattice and ferromagnetic stripes along the other (figure 1.12).

It was predicted by DFT calculations [78] and confirmed by experiments [79] that the magnetic ground state of FeTe has a double-stripe-type antiferromagnetic order in which the magnetic moments are aligned ferromagnetically along a diagonal direction and antiferromagnetically along the other diagonal direction of the Fe square lattice, as shown schematically in figure 1.15 a. Meanwhile, DFT calculations predict that the ground state of FeSe has the single-stripe-type antiferromagnetic order, similar to those in LaFeAsO and BaFe2As2, as shown in figure 1.15 b.

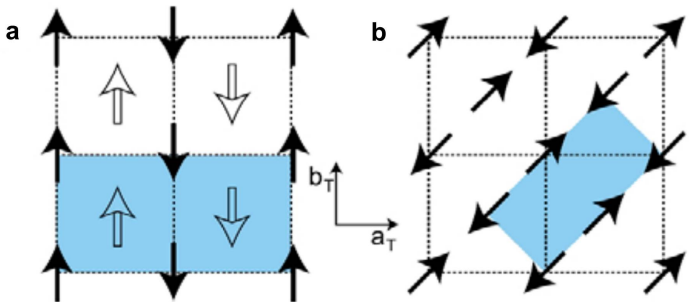

Figure 1.15: In a, double-stripe-type antiferromagnetic order in FeTe. The solid and hollow arrows represent two sublattices of spins. In b, single-stripe-type antiferromagnetic order in $BaFe_2As_2$. The shaded area indicates the magnetic unit cell. Adapted from [79]

The energetic stability of (π, 0) antiferromagnetic ordering over (π, π) ordering in FeTe has been studied in [78]. They found that it can be described by the nearest, second nearest, and third nearest neighbor exchange parameters, J1, J2, and J3, respectively, with the condition J3 > J2/2. Authors in [80] found that Te height from the Fe plane is a key factor that determines antiferromagnetic ordering patterns in FeTe, so that the magnetic ordering changes from the (π, 0) with the optimized Te height to the (π, π) patterns when Te height is lowered.

1.5.1.3 Superconducting gap

The symmetry of the superconducting gap function $\Delta(k)$ has turned out to be a subject of debate in FeBSC. Figure 1.16 schematically presents various possible scenarios. The conventional s-wave state (a) has a gap with the same sign everywhere on the FS. The simplest scenario for FeBSC is the s+- state (b) in which the gaps on hole and electron FSs are treated as constants and only differ in sign.

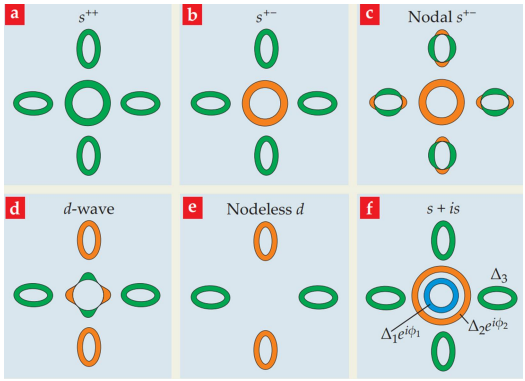

Figure 1.16: Schematic representation of the different scenarios proposed for pairing symmetries in FeBSC, colors represent the phase of the order parameter at each pocket. Adapted from [76].

Theorists realized early on, however, that because of the multiorbital nature of FeBSC, an s+- gap function on each pocket necessarily has an angular variation that may be substantial. Due to this angular variation, it is possible that four nodes develop on each FS (c). Such nodes have been called accidental, since their position is not set by symmetry. In contrast, a d-wave gap (d), by symmetry, must have its nodes along certain directions in reciprocal space. But if there is no central hole pocket, a d-wave state need not have nodes (e). The presence or absence of the nodes is highly relevant, as it completely changes the low-temperature behavior of a system compared with a conventional s-wave superconductor [81].

An even more subtle issue is the actual structure of the gap function phase in a generalized s+- state [77]. We considered the case when the phase changes by π between hole and electron pockets, but in multiband systems other cases are possible, for example, a sign change, as in s+-, but now between different hole pockets, or phase differences which are not integer multiples of π (f). In the second case,

superconducting order breaks time-reversal symmetry and is therefore dubbed s + is.

1.6 Induced superconductivity in 2D systems

Superconductivity induced in low dimensional systems attracts considerable interest of both theorists and experimentalists for many decades. Recently, one sees a revival of this interest in connection with the growing number of experiments carried out for a variety of new artificial systems which include two-dimensional electron gas, graphene, semiconducting nanowires and carbon nanotubes, topological insulators, etc [82, 83].

Authors in [84] have studied the problem of induced superconductivity in a normal thin layer in contact with a superconductor in detail. They considered several fundamental properties of the vortex matter in the systems with induced superconducting order. They argued that the proximity induced superconducting gap Δ_{2D} is responsible for appearance of a new length scale in the vortex structure, the 2D coherence length, $\xi_{2D} = \hbar v_{2F} / \Delta_{2D}$; $\xi_{2D} = \sqrt{\hbar D_{2D}/\Delta_{2D}}$ for clean or dirty limits, respectively. Here v_{2F} and D_{2D} are the Fermi velocity and diffusion constant in the 2D layer. The energy gap Δ_{2D} depends on the tunneling rate Γ; for example, $\Delta_{2D} \approx \Gamma$ for $\Gamma << \Delta$. The 2D penetration depth $\lambda_{2D} \propto 1/\Delta_{2D}^2$ increases as Δ_{2D} decreases. Therefore, a higher penetration depth is expected in the induced superconductor and a change in the local screening properties may be measurable on it using MFM, Hall microscopy or other local magnetic measurements.

1.6.1 Induced superconductivity on graphene

Graphene is a bidimensional material consisting in C atoms arranged in honeycomb arrangement. The electronic structure of an isolated C atom is $(1s)^2\ (2s)^2\ (2p)^4$. The 1s electrons remain within the isotropic s-configuration, but the 2s and 2p electrons hybridize. One possible result is four sp^3 orbitals, which naturally tend to establish a tetrahedral bonding pattern. This is what happens in diamond. However, an alternative possibility is to form three sp^2 orbitals, leaving over a more or less pure p-

orbital. In that case the natural tendency is for the sp^2 orbitals to arrange themselves in a plane at 120° angles like in the case of graphene (figure 1.17).

A calculation of graphene's band structure as early as 1947 captured the dynamics of its electrons in the crystal lattice [85]. Now, 60 years later, Geim and his collaborators [86], and separately a team from Columbia University led by Philip Kim [87], have experimentally explored the nature of graphene's conductivity and verified the exotic electrical properties. In particular, that its mobile electrons behave as if they were massless, relativistic fermions. In conventional semiconductors, electrons are ascribed an effective mass m^* that accounts for their interaction with the lattice. The energy E depends quadratically on the momentum ($E = \hbar\vec{k}^2/2m^*$, where k is the electron wavevector).

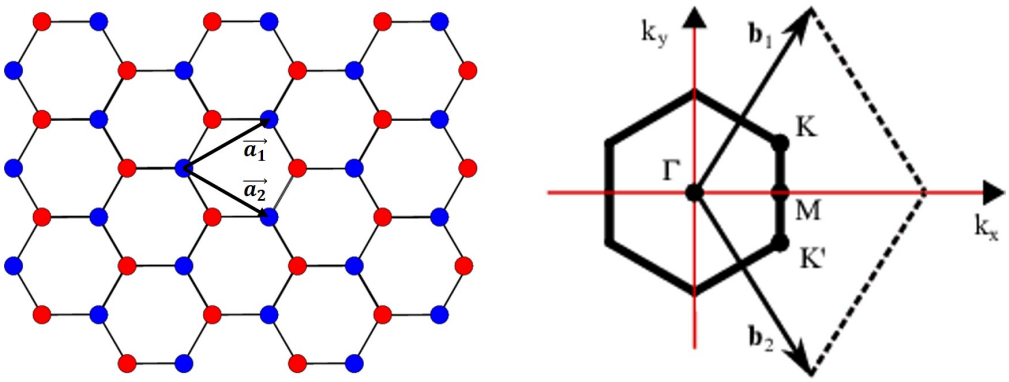

Figure 1.17: Graphene honeycomb lattice and its Brillouin zone. In the left panel, lattice structure of graphene, composed of two interpenetrating triangular lattices represented by red and blue circles ($\vec{a_1}$ and $\vec{a_2}$ are the lattice unit vectors of the lattice). In the right panel, the corresponding Brillouin zone.

Graphite, a semimetal whose bands slightly overlap and allow pockets of electrons and holes to tunnel between layers, confirm such a dispersion relation. But in a single graphene sheet, the overlap shrinks down to a single point (Dirac point), where the bands barely touch (see figure 1.18). The result is perfect symmetry between a band filled with holes and a band filled with electrons. More significantly, the dispersion of those bands is linear as they approach each other. Consequently, the electron dynamics are best modeled by a relativistic Dirac equation, which describes a linear relation between energy and momentum: $E = \hbar\vec{k}v_F$, in which the Fermi velocity v_F of electrons or holes replaces the speed of light. The dispersion curve then implies

that the electrons mass vanishes throughout a large range of momentum values in the crystal lattice.

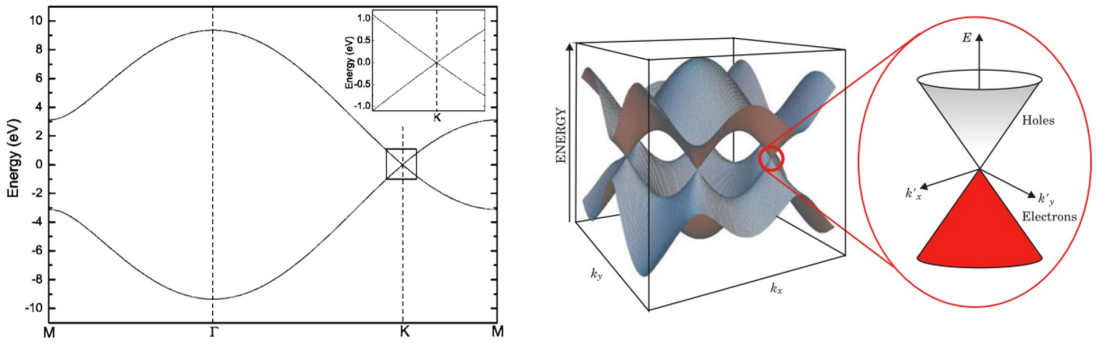

Figure 1.18: Band structure of graphene. In the left panel, the band structure of a single graphene layer along MΓKM. The inset is an enlargement of the region indicated by the square around the K point. In the right panel, a band-structure picture of the crystal describes the energy dependence of that electronic motion. A semimetal, graphene has valence and conduction bands that just touch at discrete points in the Brillouin zone. The energy-momentum dispersion relation becomes linear in the vicinity of those points, with the dispersion described by the relativistic energy equation $E = \hbar\vec{k}v_F$, where v_F is the Fermi velocity and $\vec{k}$ its momentum. Consequently, an electron has an effective mass of zero and behaves more like a photon than a conventional massive particle whose energy-momentum dispersion is parabolic. Adapted form [88] and [89]

Electrons in single-layer graphene (SLG) are predicted to condense to a superconducting state, either intrinsically by doping [78, 90–95] or by placing SLG on a superconductor with a BCS or a non-BCS pairing symmetry [96, 97]. The resulting symmetry depends on the position of the Fermi energy (E_F) with respect to the Dirac point. In particular, for FE shifts up to 1 eV, a p-wave [78, 92] state is predicted. As the doping approaches the van Hove singularity (FE $\approx$ 3 eV; ref. [95]), a singlet chiral d-wave and triplet f-wave symmetry are also predicted [93, 96]. Ref. [94] found dominant chiral d-wave superconductivity near van Hove doping and argued that weak coupling superconductivity for doping levels between half-filling and the van Hove density is of Kohn-Luttinger type and likely to be f-wave pairing for disconnected Fermi pockets. Reference [92] predicted that a non-chiral p-wave symmetry is favoured for small nearest-neighbour repulsion (<1.1 eV), small onsite interaction U ($\approx$ 8.4 eV) or large doping (above 10%), whereas the chiral p-wave state occurs as U

or V are increased or the doping level diminishes with respect to the aforementioned values (in pure SLG at half-filling U is $\approx$ 9.3 eV and V is 5.5 eV; ref. [92]). At low density (20%) and including next-nearest neighbour hopping, a chiral p-wave state can emerge [78]. Moreover, the possibility of spin-triplet s-wave pairing has been considered in bilayer graphene [98].

Although intrinsic superconductivity in SLG has not been observed [99], superconductivity has been induced by doping SLG with Li adatoms [100], intercalating SLG sheets with Ca (ref. [101]) or by placing SLG on a superconductor [102]. In the latter case, the intrinsic pairing potential for p- or chiral d-wave superconductivity can be in principle, as shown by calculations, [97, 103] to the point that a full transition to a superconducting state is triggered and manifested in the SLG superconducting density of states (DoS).

Tonnoir et al. [102] locally probed the superconducting DOS in SLG on the s-wave superconductor Re by scanning tunnelling microscopy (STM). They found induced superconductivity in SLG from the observation of a gapped DOS that matched the underlying layer of Re (s-wave). The absence of unconventional superconductivity, may indicate a modification of the SLG band structure [104, 105] due to the high carrier density of Re ($n_e \approx 4.5 \times 10^{23}$ cm^{-3}) resulting in significant charge transfer.

1.7 Motivation

The vortex distribution has been studied in a huge amount of superconducting systems like type I, BCS prototype type II or High T_C superconductors. The knowledge of their interaction and distribution has remarkably advanced in the last decades. But, there are still open questions on this matter. For example, the study of the vortex distribution is usually made on the mixed state of type II SCs at magnetic fields well above H_{C1}. Some works have advanced in the understanding of the IMS in type II SCs, but the mechanism of formation of vortex patterns below H_{C1} is still an open debate [19–21]. In particular, the possible mechanisms of the vortex distributions at very low fields and the current controversies on this matter are discussed exten-

sively in [40]. Moreover, the majority of the previous works have been focused on the "passive" characterization of the vortex lattice but not on its local manipulation with scanning techniques. Some recent works have successfully manipulated Abrikosov vortices in 3D superconductors [106–109] but the manipulation of 2D pancake vortices and Josephson vortices in highly anisotropic systems has not been achieved yet. In particular, the force exerted on a PV by a JV has not been measured yet. On the other hand, the coexistence between superconductivity and magnetism has attracted a lot of attention in the last decade. Several theoretical and experimental attempts to understand the interplay between both states have been done in the last years. But, the interplay of the magnetism in the superconducting state and the paring mechanism of the Copper pairs in these systems remains unclear [68, 73, 77, 110–112]. In addition, the local characterization of a system where magnetic and superconducting domains coexist has not been achieved yet. The recent proposal of phase separation between superconducting and antiferromagnetic domains under the action of biaxial strain in Co doped $CaFe_2As_2$, opens a good opportunity to perform the local characterization of this coexistence [71]. Finally, induced superconductivity in graphene is one of the great goals of the last few years. Several groups have reported insight of superconducting behavior in graphene by different techniques. But, there is no microscopic evidence of the magnetic properties of graphene in contact with a superconductor.

From an experimental point of view, answering those question needs a scanning probe technique capable to measures the topographic and magnetic profiles in areas of several tens of microns at low temperatures in a short period of time. Tilted magnetic fields are useful to study in-plane anisotropies or to determine the direction of, for instance, Josephson vortices. In order to manipulate the superconducting vortices in a controlled way, the scanning technique also has to be able to interact with them when necessary and avoid perturbations when not desired. For these reasons, during the thesis, a set-up with a magnetic force microscope of low temperatures working in combination with a homemade three axis superconducting magnetic coil was employed as the main technique. The magnetic force microscopy is the only technique that allows to measure simultaneously the topography and the local magnetic profile of samples. In addition MFM has probed to be an effective tool to local manipulation

of magnetic structures.

Our set-up has allowed us to characterize areas up to 20×20 μm^2 at low temperatures in a few minutes with tilted applied magnetic fields and interact with magnetic structures on the samples in a controlled way. Four systems were selected in the thesis due to their specifics properties to try to bring some light in the topics we have presented in the previous paragraphs, β-Bi_2Pd, $Bi_2Sr_2CaCu_2O_8$, $Ca(Fe_{0.965}Co_{0.35})_2As_2$ and different β-Bi_2Pd/graphene heterostructures.

CHAPTER 2

Experimental methods

In this thesis, I have used magnetic force microscopy (MFM) at low temperatures to investigate the local properties of several superconductors. MFM allows to measure the magnetic field distribution at low temperatures in large areas (20×20 μm^2 at 2 K in our case) in rough or nanostructured samples where the differences in height are too big for techniques like scanning tunnelling microscopy (STM). MFM also allows single vortex manipulation [113]. For these reasons, MFM has become one of the most interesting techniques to study the local magnetism in different systems.

This chapter has been organized in three sections. The first one is devoted to the description of our experimental set-up. The second section collects a detailed characterization of the MFM probes at low temperature. Finally, the third section describes the solution growth method used to grow several of the crystals characterized in this work

2.1 Set-up

A Low Temperature Atomic Force Microscope (LT-AFM) from Nanomagnetics Instruments Ltd. was employed during the thesis. It was used to characterize the superconducting vortex lattice and magnetic domains of several samples using the MFM mode. The microscope was used in combination with a home-designed cryostat and a

commercial variable temperature insert (VTI) provided by American Magnetics Inc. and a home-made three axis magnetic vector magnet.

2.1.1 Cryostat, VTI and vibration isolation stage

Our cryostat consists of a 80 L liquid He main chamber where the VTI and the superconducting coil are placed. To isolate the liquid He bath from room temperature, the chamber is covered on top by a 50 L liquid nitrogen bath and both chambers are surrounded by a high vacuum compartment separated by stainless steel walls. The isolation of the liquid He bath allows us to perform experiments down to 2 K for a couple of days without refilling the cryostat. The system is designed to fit a commercial VTI and a home-made magnet inside. An scheme of the cryostat is shown in figure 2.1.

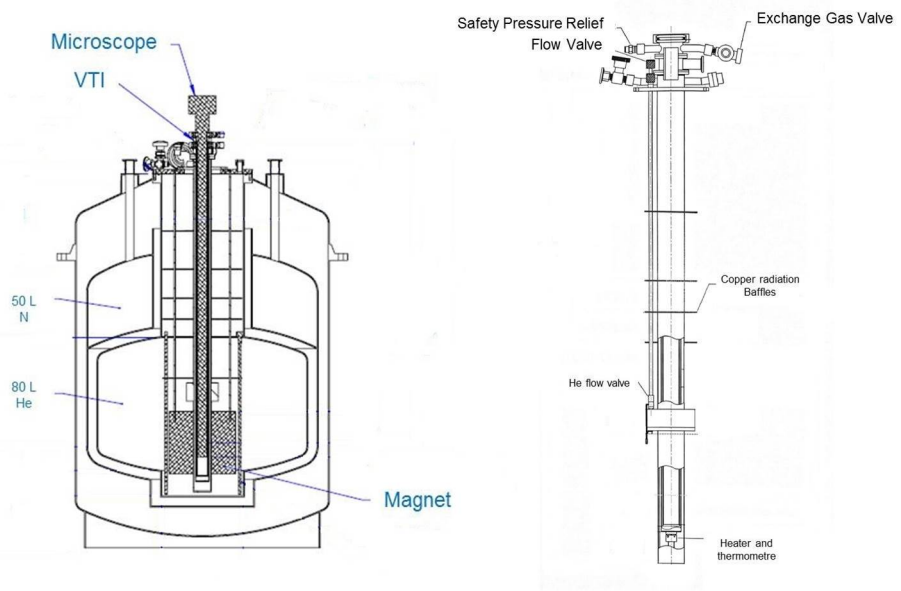

Figure 2.1: Schemes of the home-designed cryostat (left)and the VTI (right). Different chambers and walls are represented as black lines. In the left panel, the 80 L liquid He chamber is observed at the bottom, covered by the 50 L liquid Nitrogen chamber on top of it. Inside the cryostat, the position of the superconducting magnet, the microscope and the VTI are also shown. In the right panel, an scheme of the VTI shows the different valves to control the gas flow, the heater and thermometer to control its temperature and the copper radiation baffles in between.

The VTI (scheme in figure 2.1) is actually a double-layered vacuum can with two

spaces in between. It is designed to fit inside the magnetic coil in the He chamber. The inner space of the VTI is designed to accommodate our LT-AFM inside. To perform the measurements, the inner space is pumped to high vacuum and then filled with helium gas to a desired pressure (typically 0.5 atmospheres) to control the thermal contact between the liquid He bath and the microscope. The operating principle can be briefly described as follows. Through a narrow capillary, the helium liquid from the bath is siphoned into the outer space of the VTI, controlled by a needle valve. Meanwhile, the gaseous helium is pumped out through a mechanical pump. Thus, the cooling power is generated by the evaporation process of liquid helium and cold gas flowing through the outer space.

There are two working modes for the VTI, that is, one-shot mode and continuous-flow mode. In one-shot mode, the needle valve is fully opened for a while, and a large amount of liquid helium is transferred into the outer space. Then, the needle valve is totally closed and no liquid comes in. Through sustained pumping, the base temperature can be achieved with a typical value of 1.3 K, which depends on the heat load and pumping speed. In continuous-flow mode, the needle valve is kept open at a position and the liquid helium flows into the VTI continuously. As the gaseous helium is pumped out, a wide range of temperatures can be stabilized by controlling the temperature of the He gas with a 50 Ω heater on the bottom of the VTI. The heater response is fixed by a commercial Cryocon Temperature controller. The VTI provides excellent thermal response with greater sample thermal stability allowing to a perfect control of the temperature at the microscope during the experiments with oscillations below 0.01 K. The cryostat is placed on a vibration isolation system.

The He evaporated and pumped out from the cryostat is heated and directed to a recovery line to liquefy it again at the *Servicios de Apoyo a la Investigacion Experimental* (SEGAINVEX) facilities.

In figure 2.2, a picture of the cryostat, the isolation stage, the mechanical pump, the heaters, the recovery line and the control electronics is presented.

Figure 2.2: Picture of our set-up at the laboratory. In the image are shown the electronics to control the superconducting magnet (a), the temperature controller (b), the mechanical pump used to control the gas flow in the VTI (c), the isolation stage (d), the cryostat (e), the heaters to warm the cold He pumped from the VTI (f), the He recovery line (g) and the electronics of the LT-AFM (h).

2.1.2 Three axis superconducting vector magnet

A three axis homemade superconducting vector magnet is placed inside the cryostat, in the liquid He bath. The magnet design is presented in reference [114] and consists of five superconducting coils made of NbTi wire, one coil for z axis field and two sets of split coils for the xy-plane field. The five coils are mounted in an Al cage. In figure 2.3 a and b, an scheme and a real picture of the coil are presented.

The magnet allows us to generate a magnetic field in any direction of the space up to fields of 5 T in the Z direction and 1.2 T in the X and Y direction, using a current of about 100 A. We have measured the magnetic field as a function of the distance and find a homogeneous field within a sphere around the center of the coil system of 0.2% for the magnetic field along the z axis, and of 1% for the magnetic field in the plane (Fig2.3 c). The three coil system is equipped with persistent mode switches for each set of coils giving, x, y and z components of the magnetic field. This allows us to keep a constant magnetic field over long periods of time. The magnet is energized using a power supply with three independent current sources, each one has a commuted internal commercial stage of 5 V 100 A, followed by a voltage to current

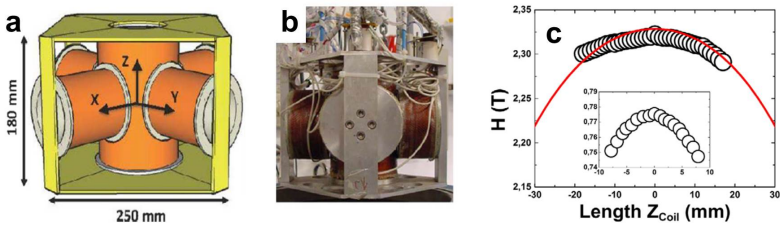

Figure 2.3: In a, an scheme of our home-made three axis vector magnet. The superconducting coils are represented in orange and the Al cage in yellow. One long coil is used to generate the z-axis magnetic field. For the in-plane field, we use two crossed split coil systems centred on the z-axis coil. The three directions of the space, X, Y and Z are marked with black arrows on the scheme of the coils, together with the real dimensions. In b, a real picture of the vector magnet. In c, we show the magnetic field vs z-axis position, with respect to the centre of the magnet when the z-coil is energized (50 A) (main panel) and when the x or y coils are energized (75 A, inset). Red line is a guide to the eye.

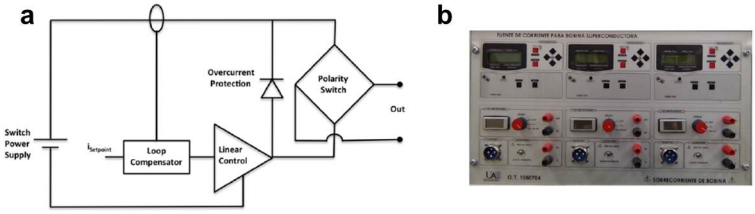

Figure 2.4: In a, we show a scheme of the current power supply for the magnet. In b, we show a photograph of the power supply. It is rather compact, 50 cm high and 80 cm long.

converter consisting of a stage providing linear regulation which uses MOSFET power transistors. Figure 2.4 shows an scheme of the circuits and a photograph of the power supply. The power supply was designed and made at SEGAINVEX mostly by M. Cuenca.

2.1.3 Low Temperature Microscope

The LT-AFM can be divided in two main parts, the insert and the head. The insert can be attached to the microscope head using low temperature connectors, allowing the exchange of different heads such as AFM, SHPM, STM etc. Radiation buffers are

placed along a stainless steel tube that gives mechanical shielding and guide to all the necessary wires. It has a KF 40/50 connector on the top that fits in the variable temperature insert (VTI) space of the cryostat. A schematic representation of the microscope is presented in figure 2.5.

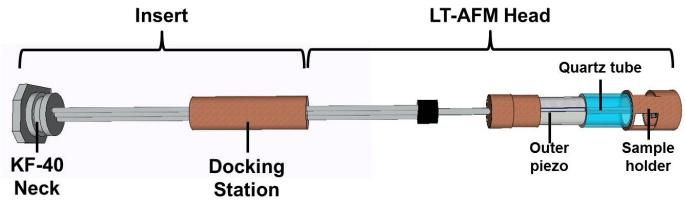

Figure 2.5: Scheme of the LT-AFM microscope. In the picture the whole microscope, insert and head, is shown. At the top of the microscope, the KF-40 neck that fits on the VTI. In the middle, the docking station to attach the insert to different microscope heads. At the bottom, the AFM head, the outer piezo, the quartz tube and the sample holder are shown.

The microscope head is formed by the AFM probe holder, two concentric lead zirconate piezotubes, a quartz tube, and the sample holder. A real picture of the LT-AFM head is shown in figure 2.6).

2.1.3.1 AFM probe holder

The AFM probe holder is attached to the inner piezotube by two screws. It has a commercial AFM alignment holder from NanoSensors, glued on top of a small piezo stack element, which is sandwiched between two alumina plates. The AFM probe is fixed on the AFM holder using a spring connected to the body of the holder. The AFM holder also has a Zirconium ferrule tube used to align the end of an optical fibre with respect the AFM probe. The optical fibre is used to control the cantilever displacement with the so-called *optical laser interferometer method* (see section 2.1.3.5). The piezo below the alignment holder is used to control the fibre-probe distance. A schematic representation of the AFM probe holder is presented in figure 2.7.

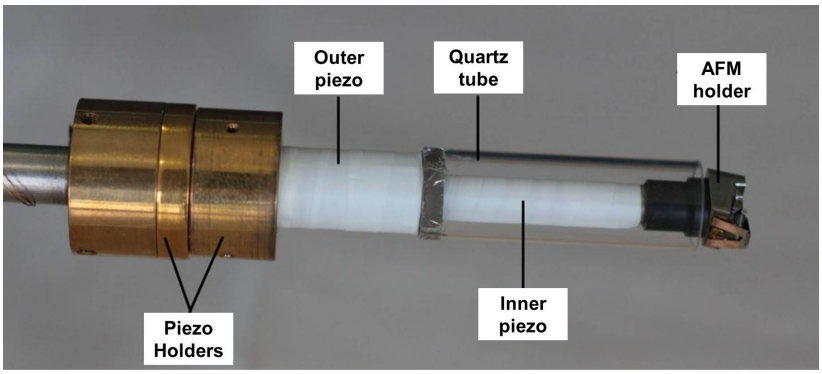

Figure 2.6: Real picture of the head of the LT-AFM. It shows the piezo holders, the two piezo tubes (wrapped in Teflon in the picture), the quartz tube and the AFM probe holder.

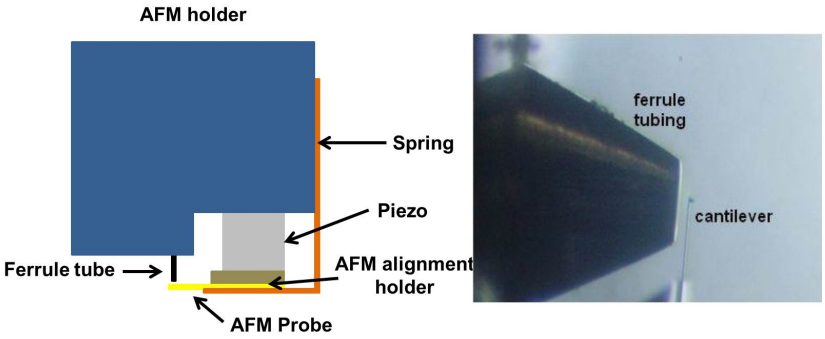

Figure 2.7: In the left panel, an scheme of the AFM probe holder. The body of the holder is represented in blue. The ferrule tube is shown in black, the AFM probe in yellow, the AFM alignment holder in brown, the piezo in grey and the spring in orange. In the right panel, a picture zoomed in the ferrule tube and the probe.

2.1.3.2 Sample holder

The sample holder is a hollow cylinder made of Phosphor bronze with a hole at the top that fits in the quartz tube. At the bottom, it has a plate where the sample is glued and a connector to bias the sample. At the side, it has a leaf spring used to attach it to the quartz tube. A picture of the sample holder is presented in figure 2.8.

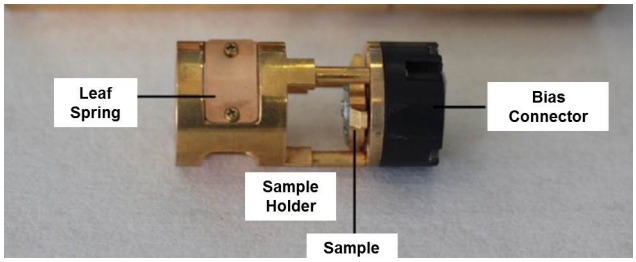

Figure 2.8: Real picture of the sample holder. In the image are visible, the leaf spring used to attach the sample slider to the quartz tube, the plate where the sample is glued and the bias connector.

2.1.3.3 Scanning and tip oscillation system

The inner piezotube is used to oscillate and scan the AFM probe over the samples. It has quadrant electrodes and a circular electrode at its apex as is schematized in figure 2.9. If an opposite voltage is applied to reciprocal electrodes, the tube will bend as is shown in figure 2.9 a. On the other hand if the same voltage is applied to all quadrant electrodes with respect to the inner electrode, the tube will extend or contract in the Z direction. It has a $\approx 20\mu m$ scan range in the XY plane and a $\approx 1.5\mu m$ retract range in the Z direction at 2 K applying a voltage difference of 200 V between electrodes. The single electrode at its apex is used to oscillate the AFM probe by applying and oscillating difference of potential to the electrode as is schematized in 2.9 c.

2.1.3.4 Approaching-retracting mechanism

The outer piezotube and the quartz tube are used to perform the approaching and retracting movement of the sample with respect to the AFM probe using the so-called

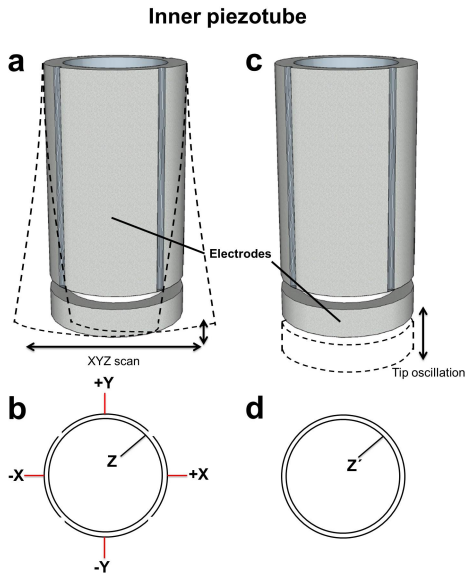

Figure 2.9: Scheme of the inner piezotube and its electrical contacts. On top, the motion of the piezotubes is schematically represented by dashed lines. On the bottom, the electrical contacts on the piezotube are shown as curved black lines. In a, an scheme of the scan movement of the inner piezotube is shown. In b, an scheme showing the five contacts to perform the scan movement, denoted by X, Y and Z. In c, an scheme of the oscillatory movement of the single electrode at the apex. In d, an schematic view of the electrical contacts of the single electrode to perform the oscillatory movement, denoted by Z′.

stick-slip method [115]. The piezotube has quadrant electrodes and the quartz tube is glued to its end.

The principle of the *stick-slip method* is schematized in figure 2.10. First, the sample holder is attached to the quartz tube with the leaf spring and is approached to a safe distance of the AFM probe by hand (A). Then, a voltage ramp is applied to the outer piezotube in about 3 ms contracting (extending) it (B). During the ramp, the sample holder moves together with the quartz tube due to the friction between them. Finally, the voltage is turned to zero in less than 1μs and the outer piezo is extended (contracted). As a consequence, the sample holder slides on the quartz tube due to its inertia, approaching (retracting) the sample to the AFM holder (C). This slider mechanism can move few hundred grams at 4 K, successfully. Note that the success of the method depends on the equilibrium between the inertia and the friction force of the sample holder, which is controlled by the pressure of the leaf

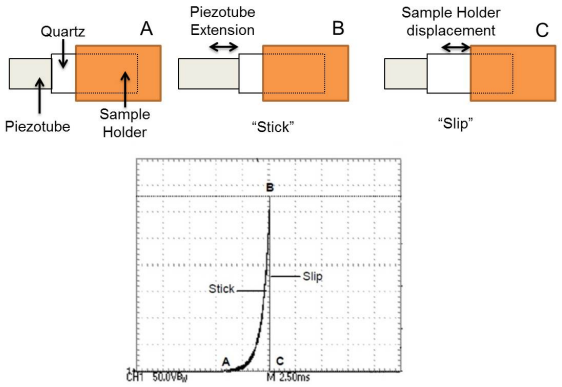

Figure 2.10: Scheme of the stick-slip method to move the sample holder. On the upper panel, an scheme of the LT-AFM head, showing the outer piezotube, the quartz tube and the sample holder. Dashed lines are used to represents the portion of the quartz tube inside the sample holder. A, B and C, represent the three steps during the sample holder displacement described in the text. In A, the sample holder is attached to the quartz tube. Then, between A and B an exponential voltage pulse is applied to the piezotube to extent or contract it. Finally between B and C the voltage is turned off to zero in less than 1 μs. As a result the sample holder is displaced a given distance. In the lower panel, a real image of the pulse on a oscilloscope, with the three steps presented on the top panel marked with A, B and C letters.

spring against the quartz tube. For this reason the quartz tube has to be carefully cleaned and the leaf spring tested at room temperature before the measurements.

2.1.3.5 Optical laser interferometer method

As it was introduced before, the optical laser interferometer method [116] [117] [118] was used in our LT-AFM to detect the displacement of the AFM probe. In this method, a laser (I) is focused at the rear part of the cantilever through an optical fibre. At the end of the fibre, some of the light is reflected by the surface (I_{rs}) and some scape the fibre and goes to the cantilever that acts as a mirror, then the laser is reflected (I_{rc}) trough the fibre, back to the source where they interfere. The interferometric pattern is a function of the optical path of each beam and therefore of the fibre cantilever separation, which allows to monitor the bending of the cantilever. It is schematically represented in figure 2.11. The photocurrent at the interferometer

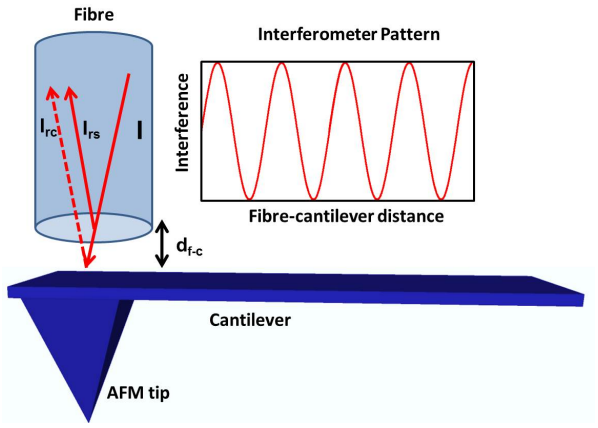

Figure 2.11: Scheme of the interferometer sensor method. The laser beam, I, travels through the fibre. At the end of the fibre, some of the light is reflected by the surface (I_{rs}) and some escapes the fibre and reaches the cantilever back that acts as a mirror, then the laser is reflected (I_{rc}) trough the fibre, back to the source where I_{rs} and I_{rc} form an interferometer pattern (red line in the plot) as a function of the fibre-cantilever distance, d_{f-c}.

can be described as follows [119]:

$$I_{inter} = I_0[1 - V cos(\frac{4\pi d_{f-c}}{\lambda})] \tag{2.1}$$

$$I_0 = \frac{I_{max} + I_{min}}{2} \tag{2.2}$$

$$V = \frac{I_{max} - I_{min}}{I_{max} + I_{min}} \tag{2.3}$$

where I_0 is the midpoint current, V the visibility, d_{f-c} the fibre-cantilever separation, R the reflectivity and λ the laser wavelength. The slope of the interference is:

$$m = 4\pi I_0 \frac{V}{\lambda} \tag{2.4}$$

As all the magnitudes except d_{f-c} are constant, the photocurrent can be used to

measure the fibre cantilever distance and therefore, the oscillation of the cantilever. To maximize the accuracy of the measurements, the equilibrium distance between the fibre and the cantilever is chosen to maximize the slope of the interferometric patter. This point is determined by measuring the interference pattern while changing the cantilever-fibre distance with the piezo beneath the cantilever. The piezo is driven between $0-125$ V forward and backward, with respect to the fibre. An example of the interferometer patter recorded at room temperature in our microscope is presented in figure 2.12.

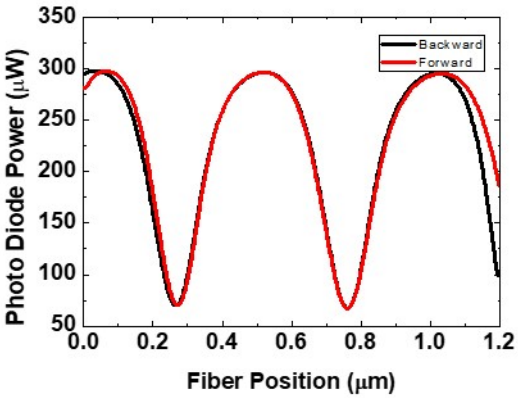

Figure 2.12: The interferometric pattern obtained by our LT-AFM at room temperature as a function of the fibre position with respect to the resting cantilever. The red and black lines represents the interferometer patter obtained when approaching and retracting the AFM probe to the fibre. The pattern is used to lock the fibre-tip distance at the maximum slope.

2.1.3.6 LT-AFM controller

The bending of the cantilever is measured by the interferometer and received by a digital Phase Lock Loop (PLL) card, which excites the cantilever at the desired frequency and measures the phase and the Amplitude of the output signal from the cantilever.

The LT-AFM controller has a very low noise power supply unit. It has four channels of low noise high voltage amplifiers to drive scan piezo. A Digital PID loop is operated at 250 kHz for the feedback. A sample slider card produces exponential

pulses up to 400 V for the stick-slip mechanism. A diagram of the control mechanism of our LT-AFM microscope is presented in figure 2.13. Both, electronics and software were developed by Nanomagnetics Instruments LTD.

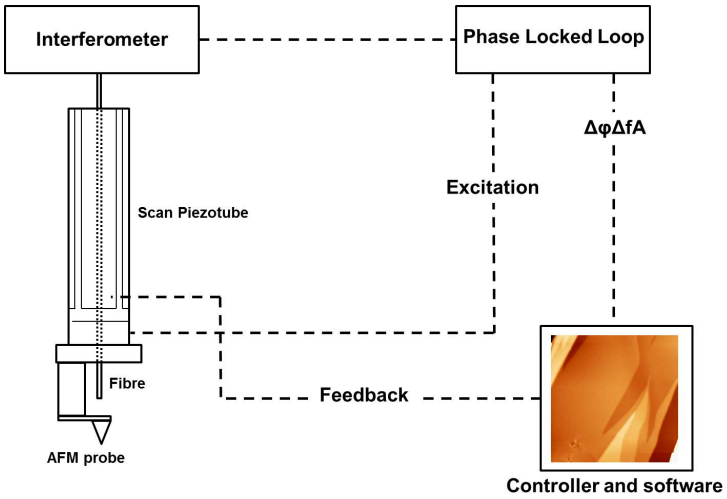

Figure 2.13: LT-AFM control scheme. In the image, different elements of the LT-AFM head are schematized using black lines. Dotted lines are used to represent the fibre position inside the piezotube. Dashed lines are used to represent the connection between the microscope and the different element in the control electronics. The information of the AFM probe displacement is recorded in the interferometer and transmitted to the Phase Locked Loop (PLL) card which excites the cantilever at the resonance frequency and measure the phase and amplitude changes. The amplitude change is used for a feedback which is operated by the controller. The scan and coarse approach mechanism is also managed by the controller.

2.1.3.7 Operational modes

Since the invention of the Atomic Force Microscopy, many different measurement modes have been developed to have access to different tip-sample interactions, and thus different sample properties, in different ambient conditions [120]. In this section we will introduce the two main modes used during the thesis in our LT-AFM, the *dynamic mode* and the *MFM mode*:

2.1.3.7.1 Dynamic mode In the dynamic mode the AFM cantilever is oscillated at a given amplitude at its resonance frequency and placed near to the sample (5-

15nm). In such scenario, the tip is near enough to the surface to interact via short range Van der Waals (VdW) forces with the surface [120, 121]. The oscillation amplitude should be large enough to ensure that the restoring force at the lower turning point is larger than the attractive force between tip and sample. This will avoid an instability, which would stop or at least seriously distort the oscillation. The tip-sample interaction causes a shift in the resonance frequency which is used to measure the force acting on the tip [120, 121].

If we approximate the cantilever and the tip as point-mass spring (figure 2.14), we can consider the AFM probe as a damped oscillator due to friction forces, with some driving force, and into a force field created by the tip sample interaction, then its movement can be described by a linear, second-order differential equation [120]:

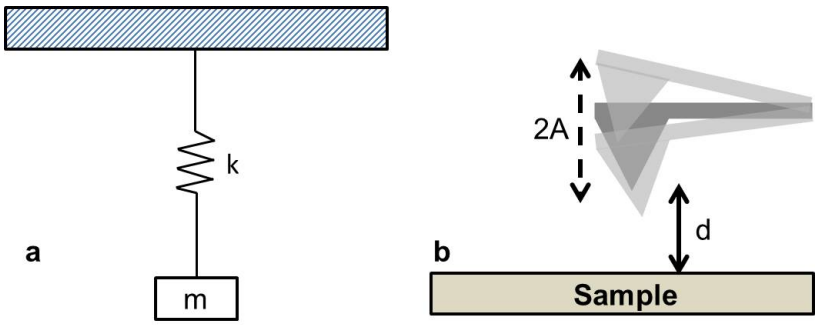

Figure 2.14: Point-like mass spring as an approximation of the AFM cantilever. In a, a simple point like mass spring as an approximation of the cantilever movement. In b, an scheme of the oscillating tip is showed.

$$m\ddot{z} + \delta\dot{z} + k(z - z_0) = F_d + F_{t-s} \tag{2.5}$$

where $F_d = F_0 cos(\omega t)$ is the driving force provided by the piezotube to oscillate the cantilever at an angular frequency ω, F_{t-s} is the force due to the tip sample interaction and δ is the damping factor which can be calculated as [120]:

$$\delta = \frac{k}{f_0 Q} \tag{2.6}$$

where Q is the quality factor of the oscillator and $f_0 = \sqrt{\frac{k}{m}}$ the resonance frequency

of the free oscillator. To solve equation 2.5, F_{t-s} is expanded into a Taylor series:

$$F_{t-s}(z) = F_{t-s}(z_0) + \frac{\delta F_{t-s}(z_0)}{\delta z}(z - z_0) \tag{2.7}$$

and equation 2.5 can be rewritten as:

$$m\ddot{z} + \delta\dot{z} + k(z - z_0) = F_d + F_{t-s}(z_0) + \frac{\delta F_{t-s}(z_0)}{\delta z}(z - z_0) \tag{2.8}$$

$$m\ddot{z} + \delta\dot{z} + [k - \frac{\delta F_{t-s}(z_0)}{\delta z}](z - z_0) = F_d + F_{t-s}(z_0) \tag{2.9}$$

The term $k - \frac{\delta F_{t-s}(z_0)}{\delta z}$ in equation 2.9 is called the effective spring constant, k_e. Solving 2.9, we will find:

$$z(t) = z_0 + Acos(2\pi f_e t - \phi) \tag{2.10}$$

Equation 2.10 represents an harmonic oscillator with angular frequency ω_e different that the angular frequency of the free oscillator and with a phase shift of ϕ. The frequency of the oscillator is:

$$f_e = \sqrt{\frac{k}{m} - \frac{1}{m}\frac{\delta F_{t-s}}{\delta z}} = \sqrt{f_0^2 - \frac{1}{m}\frac{\delta F_{t-s}}{\delta z}} \tag{2.11}$$

Taking into account that $k >> \frac{\delta F_{t-s}}{\delta z}$, equation 2.11 can be reduced to:

$$\Delta f \approx \frac{f_0}{2k}\frac{\delta F_{t-s}}{\delta z} \tag{2.12}$$

Therefore, when the cantilever is brought into a force field, the resonance frequency will be shifted and the force gradient can be measured by measuring the shift

in the resonance frequency or if the excitation frequency is kept constant, by measuring the change in amplitude (ΔA) or the change in phase ($\Delta\phi$) of the oscillation as is seen in Figure 2.15.

In our system, in the dynamic mode, topographic images are measured by keeping constant the excitation frequency and the amplitude of the oscillation. A feedback is used to keep the amplitude constant by changing the length of the scan piezotube. The topography is measured using the change in the length of the piezotube.

2.1.3.7.2 MFM mode In MFM, the interaction between a magnetic probe and a magnetic sample is measured.

The topography and the magnetism of a magnetic sample can be measured independently using an extension of the dynamic mode, called *two pass mode*. In this mode, the operational parameters are chosen such that either, the non-magnetic or the magnetic interaction becomes dominant. This is achieved due to the small contribution of the magnetic forces at small distances ($< 5nm$) and the VdW forces at large distances ($> 50nm$) [120].

In the MFM two pass mode, the topography is measured in a first scan (forward) in the same way that in the dynamic mode. Then, the probe is retraced a large distance and a second scan is performed following the profile recorded during the first scan (backward). In the second scan, the tip is oscillated at the same frequency that the first scan but with the amplitude feedback opened. In this case, the length of the piezotube is used to keep the tip-sample separation constant, using the information of the topographic scan. Then, the tip-sample magnetic interaction is recorded by measuring $\Delta\phi$. An scheme of the two pass mode is presented in figure 2.16.

The MFM contrast is associated to the magnetic domains in the sample. Assuming that the magnetization of the tip is in the axial direction, when the stray field from the sample is parallel to the tip magnetization there is a repulsive force which is typically represented in MFM images as dark contrast and if the stray field is antiparallel the contrast will be bright.

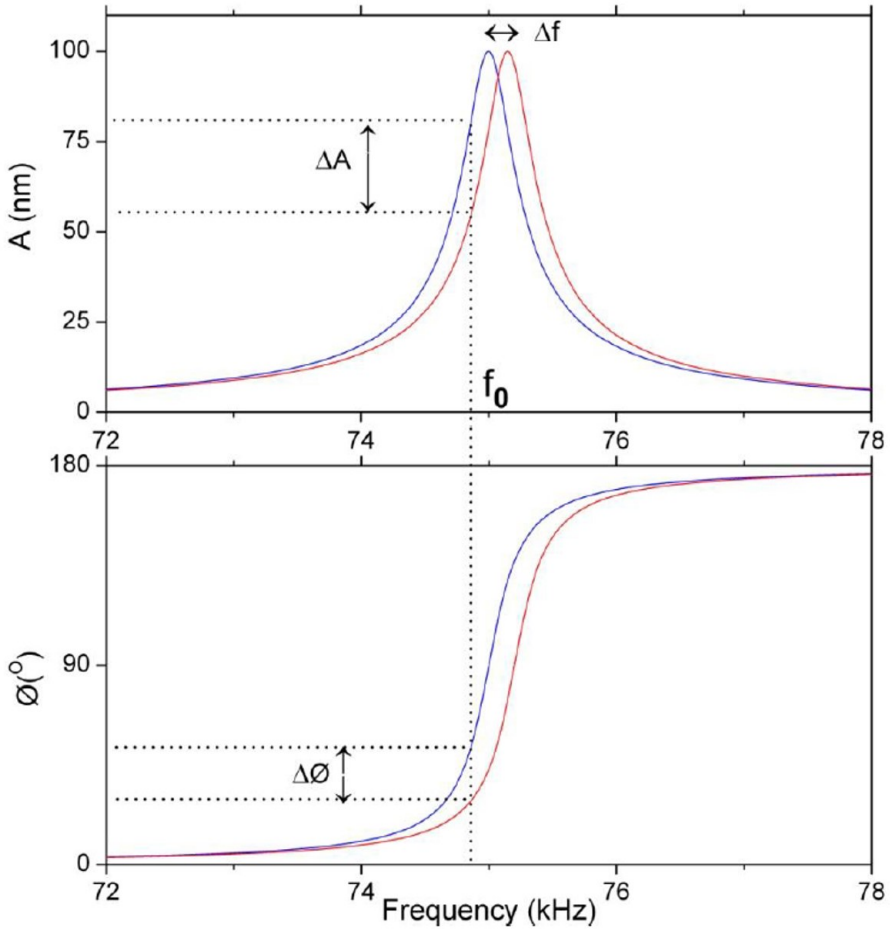

Figure 2.15: Oscillation amplitude (A) and phase (ϕ) versus frequency. In the plots, the blue line represents the amplitude and phase of the cantilever far from the surface and the red line their shift due to the interaction with the sample. In the upper panel, the oscillation amplitude decreases by ΔA when the tip os oscillated at a frequency f_0 due to the shift in the oscillation frequency Δf. In the lower panel, the corresponding change in the oscillation phase $\Delta\phi$ is shown.

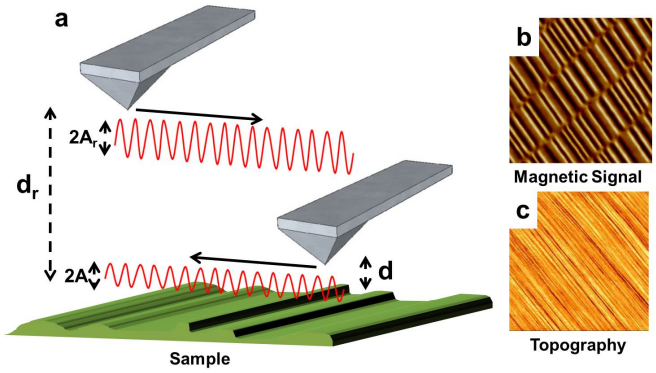

Figure 2.16: In a, an schematic representation of the MFM two pass mode. A first scan near the surface at a distance, d, and amplitude, A, is made to record the topographic profile. Then, the tip is retraced a distance d_r and scans the same profile at a constant height, d_r, and amplitude A_r to measure the long range magnetic interaction. The trajectory of the tip during the scans is represented with a red line. In b and c two examples of the magnetic and topographic images obtained in a Hard Disk Drive (HDD).

2.2 Characterization of MFM probes for low temperature experiments

During the thesis mainly two types of AFM probes were used: *Nanosensors Point Probe Plus Force Modulation Mode - Reflex Coating* (PPP-FMR) and *Nanosensors Point Probe Plus Magnetic Force Microscopy - Reflex Coating* (PPP-MFMR) probes. Both kind of probes are made of Silicon with a cantilever length of 225 μm, width of 30 μm, thickness of 3 μm and spring constant of 3 nN/nm. The difference between them is that PPP-MFMR probes have a CrCo alloy layer of $\approx 20nm$ deposited on the tip and the cantilever, allowing the magnetic characterization of the samples. PPP-FMR probes were used for preliminary topographic characterization and PPP-MFMR probes for magnetic characterization. Figure 2.17 shows the AFM probes geometry with a rectangular cantilever and a sharp tip at the end.

The CrCo alloy that covers the PPP-MFMR probes is a ferromagnetic material, and therefore it presents an hysteresis cycle in its magnetization when changing the magnetic field. At room temperature the coercive field ($\approx 300Oe$) and magnetic moment (10^{-13} emu) are provided by the manufactured, but for lower temperatures a

magnetic characterization of the probe must be done in order to obtain its coercive field for a proper tip magnetization. For this purpose we have measured the ferromagnetic domains of a Hard Disk Drive (HDD) as a function of the temperature from 300 K to 2 K [122].

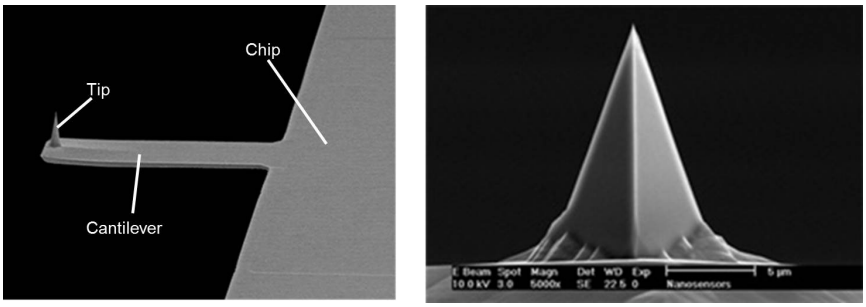

Figure 2.17: SEM images of an AFM probe. In the left panel, the silicon chip where the probe is lithographed, the rectangular cantilever and the pyramidal tip. In the right panel, a zoom on the tip showing its pyramidal shape.

Ferromagnetic domains of HDD are known to have coercive fields much greater (2000-5000 Oe) [123] than typical MFM probes. This makes them the perfect candidates to characterize de hysteresis cycle of MFM probes as their magnetic state will not be changed by the small magnetic fields needed to switch the state of the tip.

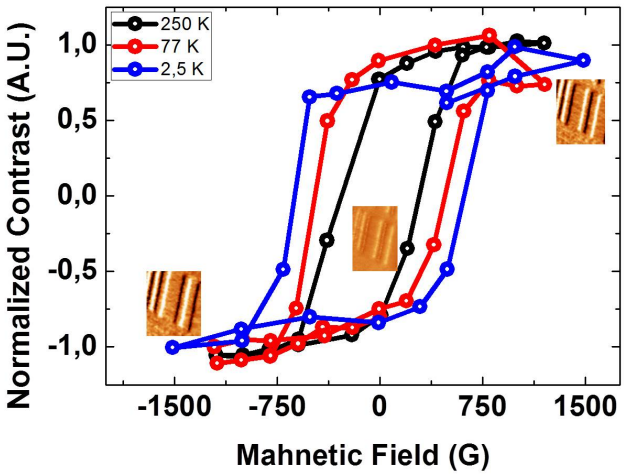

Figure 2.18: Ferromagnetic cycles of a PPP-MFMR tip measured at 250 K, 77 K and 2.5 K, using a HDD as a sample. Three MFM images of the magnetic domains at 1500, 0 and -1500 Oe at 2.5 K of the HDD are also shown as inset. In the images, the switching of the tip magnetization is revealed by the change in the contrast from dark to bright and vice versa in the magnetic domains of the HDD.

The hysteresis cycle of a typical PPP-MFMR probe was recorded by measuring the surface of a HDD at different fields and constant temperature for several temperatures. We have calculated the magnetic moment of the tip (in arbitrary units) as the difference in contrast between domains walls of the HDD in the MFM image [124]. The hysteresis cycles for 250 K, 77 K and 2.5 K are represented in figure 2.18. The coercive field of the tip changes from $\approx$ 300 Oe at RT to $\approx$ 1000 Oe at 2.5 K.

This characterization is extremely important for a proper interpretation of the MFM images, as they are the result of the interaction of the tip magnetization and the stray field of the sample [120].

2.2.0.1 MFM features

To illustrate the importance of the characterization of the MFM tips at low temperatures, we will present the particular cases of MFM images of superconducting vortices when a PPP-MFMR tip is magnetized below and above its coercive field.

If the tip is not magnetized above its coercive field, different domains with different orientation can appear at the tip [125–127]. For example, let us discuss the images shown in figure 2.19. In the images, superconducting vortices were measured in $\beta - Bi_2Pd$ at 2 K with a tip magnetized with 500 Oe at 5 K, which is well below the coercive field. As it was presented in the introduction of the thesis, superconducting vortices are known to have circular shapes with radius determined by λ. In our experiment, the superconducting vortices appear as star-like features instead of as circles, pointing out the existence of a several magnetic domains on the tip, probably at the sides of the pyramid (see figure 2.20 a). A simple explanation of the origin of the star-like features will be discussed in the following:

The tip-vortex interaction can be approximately written as [128]:

$$\frac{\delta F}{\delta z} = m_x \frac{\delta^2 H_x}{\delta x^2} + m_y \frac{\delta^2 H_y}{\delta y^2} + m_z \frac{\delta^2 H_z}{\delta z^2}. \tag{2.13}$$

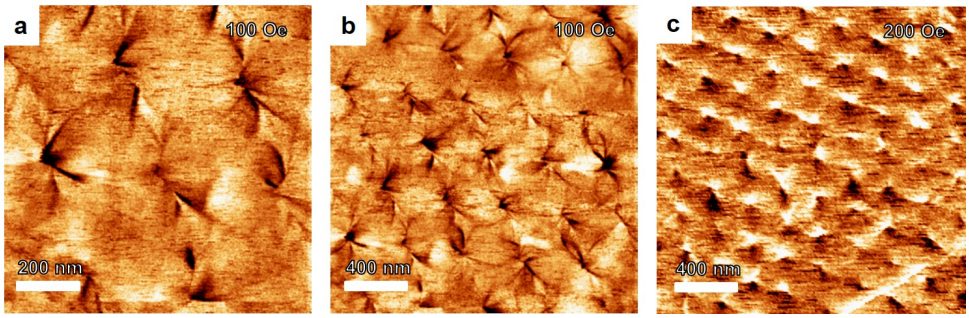

Figure 2.19: Examples of star-like features at superconducting vortex positions when a MFM tip is not magnetized up to its coercive field. The three MFM images where taken at 2 K. Images a and b were taken at 100 Oe while c was taken at 200 Oe.

Where $m_i; i = x, y, z$ are the components of the magnetic dipolar moment of the tip and $H_i; i = x, y, z$ are the components of the field created by the vortex. The field created by a vortex can be described as [28]:

$$B = \frac{\phi_0}{2\pi\lambda^2} K_0((r/\lambda)e^{\frac{-2\pi z}{d}} \tag{2.14}$$

where K_0 is the modified Bessel functions of second order and r and z the radial and vertical distances from the vortex core.

Most often, the X and Y components of the dipolar moment of the tip are neglected [127]. This is justified, because the predominant magnetization of the tip is along the z-axis. Here, however, we will take into account an in-plane magnetization. This will lead to the observed star-shaped vortices. We consider a tip with non zero X an Y components. By calculating spatial maps of the force gradient sensed by the cantilever using equation 2.13, we find that indeed finite x and y components of the magnetization provide star shaped vortices as is shown in Fig.2.20 c. The star-like features obtained by our simple model, are very similar to the vortex shapes obtained in the experiments. Real MFM images of star-like vortices are shown in figures 2.20 b and d together with the result of the simulations.

In order to compare the images obtained by a MFM tip magnetized below and above its coercive field, we have measured the vortex lattice at the same area and the

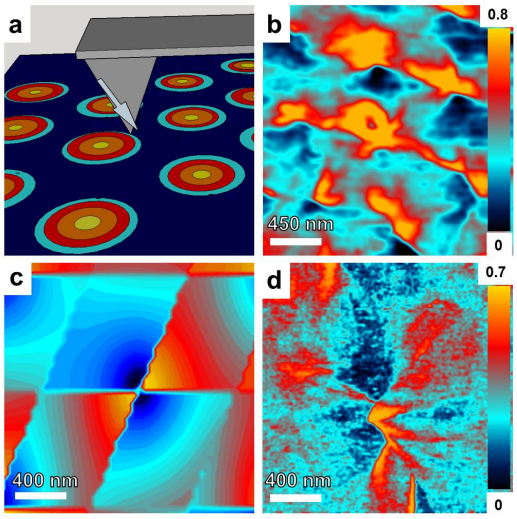

Figure 2.20: In a, we schematically show a MFM tip with a non-zero in plane component of the dipolar moment (grey arrow on the tip) and the vortex lattice (coloured circles below). In b, we show star like vortices obtained at 2 K and 100 Oe with a tip magnetized with 300 Oe at 5 K. In c and d we compare a simulation and an MFM image of a single vortex measured with a tip with an in-plane magnetization component. The same colour scale is used at the scheme, the simulation and the MFM images.

same applied magnetic field with different tip magnetization conditions. In figure 2.21 two cases are shown, one with the tip magnetized at 500 Oe (below its coercive field) and another with the tip magnetized at 1500 Oe (above its coercive field). When the tip is magnetized below its coercive field, we observe in the images the features provided by the interaction between the in-plane symmetric magnetic field of the vortex and the tip's anisotropic magnetic field distribution. Each vortex, imaged in such conditions, thus mirrors the magnetic configuration of the tip.

2.3 Crystal growth

Binary phase diagrams contain the information of all known crystallographic structures for a pair of elements as a function of the composition and the temperature. An example of a simple binary phase diagram for arbitrary elements, A and B, is presented in figure 2.22.

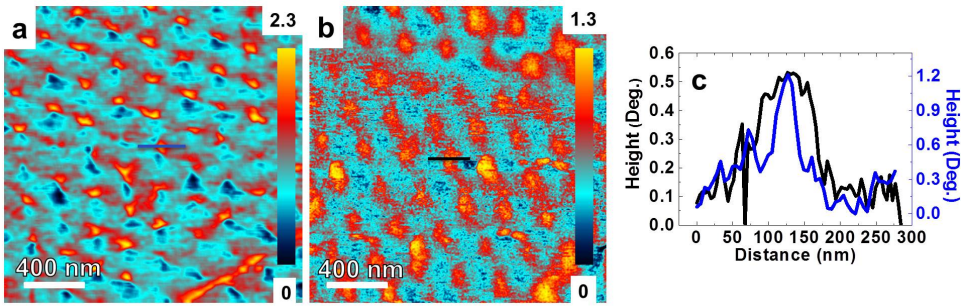

Figure 2.21: Here we show images taken at the same temperature (2 K) and magnetic fields (300 Oe) with a tip having in-plane components of the magnetization (a) and only z-component (b). The blue and black profiles shown in c were taken at the lines with the same colour in a and b. The profiles provides a measure of the spatial resolution, which is improved when the tip has an in-plane anisotropy.

The phase diagram in figure 2.22, consists in a series of vertical, horizontal and curved lines. The vertical lines, represent different known stable compositions of A-B crystals. Curved lines are the solid-liquid equilibrium lines of the compounds, meaning that at a given composition, above this line, the mixture will be in the liquid phase and below this line, a particular solid phase or phases will grow. The horizontal lines represents the temperatures where a different solid will grow.

The *solution growth method* is a powerful technique to grown single crystals using the information provided by binary phase diagrams [129]. In order to grow single crystal of a particular composition, the desired amount of A and B is placed inside two alumina crucibles with glass wool in between and sealed in a quartz ampoule in a He atmosphere using a blowtorch. The mixture is heated up to melt it, and then cooled down to the desired temperature where the crystals will start to grow, for example, for a composition of 80 percent of B in figure 2.22, 340°C (1). Then, the ampoule is slowly cooled down to a temperature above the eutectic point, as the temperature decreases, the crystal becomes bigger and the liquid mixture composition varies following the liquid line (2). If the temperature is decreased below the eutectic point (3), the remnant liquid will solidify enclosing the B crystals, making especially hard to separate them. For this reason, the alumina crucibles have the glass wool in between. Taking quickly the ampoule from the furnace and spinning it, will separate the liquid and the solid phases at both sides of the glass wool that acts as a filter.

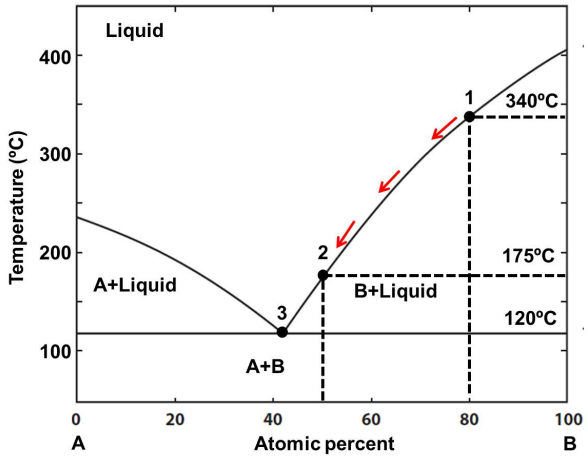

Figure 2.22: Example of a binary phase diagram. Black curved line represent the solid-liquid equilibrium line. Point 1 and 2 are the initial and final points in the growing process described in the text and 3 is the eutectic point. Dashed lines are used to point the exact temperature and composition of points 1 and 2. The red arrows represents the evolution of the composition of the liquid phase as explained in the text.

Then, clean and intact B crystals can be obtained for their research. A schematic representation of the growing process is presented in figure 2.23. Advantages of this method are two-fold. First, the presence of a mixture instead of a pure element decreases the melting line, making it easier to grow crystals. Second, the crystal grows surrounded by liquid, and we can leave it there for many weeks. It is thus extremely pure and growth is natural, without any constraints. Thus, we can obtain single crystals of extremely high quality.

Sometimes, the interesting phase of a given crystal is not stable at ambient conditions. In this case, is still possible to obtain the desired crystals by forcing them to cool down very quickly from a temperature where they are stable to the room temperature by immersing them in water or liquid nitrogen for example. Doing so, the crystal will not transit to the low temperature phase and will remain in the desired phase [129]. With this process, the remnant liquid is not filtered and the crystals will be immersed in an amorphous solid with the composition of the remnant liquid.

In conclusion, knowing the binary phase diagram of two elements allows to grow binary crystals using the *solution growth method* in a simple way.

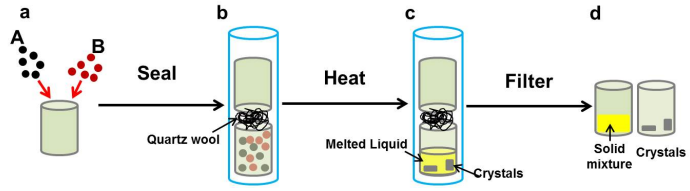

Figure 2.23: Scheme of the solution growth method. Alumina crucibles are represented as beige cylinders and the quartz tubes with blue lines. In a, the desired elements A and B (black and red circles) are placed inside the alumina crucibles. Then in B, they are encapsulated between two alumina crucibles with quartz wool in between (black line) and sealed in a quart tube in vacuum. In c, the quartz ampoule is heated in a furnace to melt the elements inside and grow the crystals. Finally, in d, the crystals are separated from the flux excess by spinning the quartz ampoule.

2.3.1 $\beta - Bi_2Pd$ single crystals growth

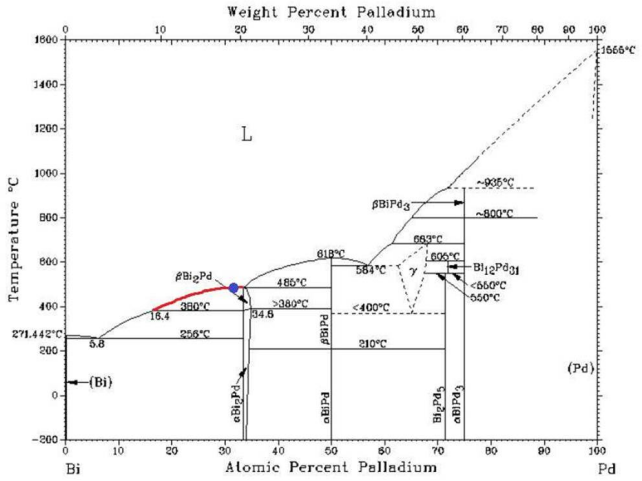

Figure 2.24: Phase diagram of Bismuth and Palladium system. The red line represents the liquid-solid equilibrium line for $\beta - Bi_2Pd$ and the purple circle the initial liquid concentration during the growth.

During the thesis, single crystals of $\beta - Bi_2Pd$ were grown using slight excess of Bi [130], [131]. We grew our samples from high purity Bi (Alfa Aesar 99.99%) and Pd (Alfa Aesar 99.95%). Bi and Pd were introduced in alumina crucibles and sealed in quartz ampoules at 140 mbar of He gas using a blowtorch. Then, the ampoules were heated from room temperature to $900°C$ in 3 h, maintained 24 h at this temperature, slowly cooled down to $490°C$ in 96 h and finally cooled down to $395°C$ in 200 h in a furnace. This temperature is about $15°C$ above the temperature for the formation

of the $\alpha - Bi_2Pd$ phase [132] (figure 2.24). To avoid formation of the α phase, we quenched the crystals down to ambient temperature by immersion in cold water. We obtained large crystals of $5mm \times 5mm \times 3mm$ (inset in figure 2.25).

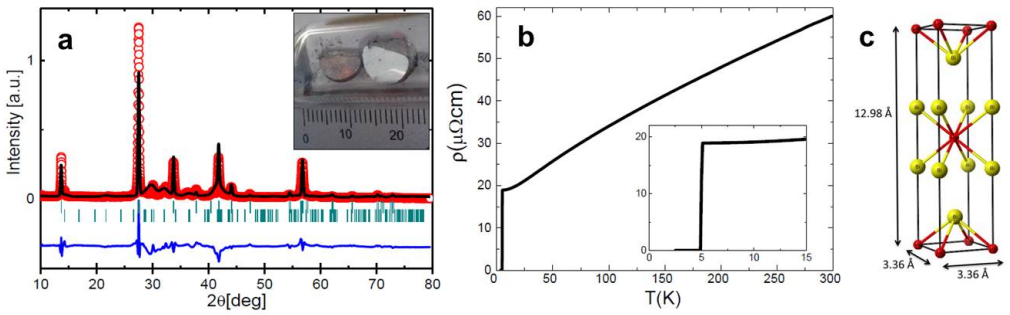

Figure 2.25: Powder diffraction pattern of $\beta - Bi_2Pd$. Red symbols are the experimental points. The black line is the best fit to $\beta - Bi_2Pd$ diffraction pattern [133]. Residuals are given by the blue line. The two series (upper and lower) of vertical green strikes represent, respectively, the position in 2θ scale of the reflections from the $\beta - Bi_2Pd$ $(I4/mmm)$ and $\alpha - Bi_2Pd$ $(C12 = m1)$ phases. The inset show a photograph of one $\beta - Bi_2Pd$ crystal. In b, the temperature dependence of the resistivity. In c, the unit cell with the lattice parameters of $\beta - Bi_2Pd$

To characterize them, we made x-ray diffraction on crystals milled down to powder (Fig.2.25, using x rays with wavelength 1.54 Å). We find $\beta - Bi_2Pd$ (I4/mmm, see Ref.[134]) with refined lattice parameters $a = b = 3.36(8)$ Å and $c = 12.97(2)$ Å and no trace of $\alpha - Bi_2Pd$. We made in total twelve growths, varying slightly the conditions for the quench, growth temperature and initial composition, and obtained always crystals with a resistivity vs temperature very similar to the one shown in Fig 2.25.

To ensure that the crystals composition is homogeneous on the whole crystal and discard the presence of Bismuth or Pd clusters in it, we have performed Energy-dispersive X-ray spectroscopy (EDX) measurements in a scanning electron microscope (SEM) at the *Servicio Interdepartamental de Investigacion* (SIdI) of the Universidad Autonoma de Madrid. We found that the 2:1 stoichiometry is constant in the whole crystal and that there is not any presence of Bi or Pd precipitates on it. We have measured the very same sample before and after exfoliating it using the Scotch tape method, finding the same results in the outer and inner layers of the $\beta - Bi_2Pd$ crystals. A SEM image of the crystal with the three different areas where EDX

experiments were performed is presented in figure 2.26.

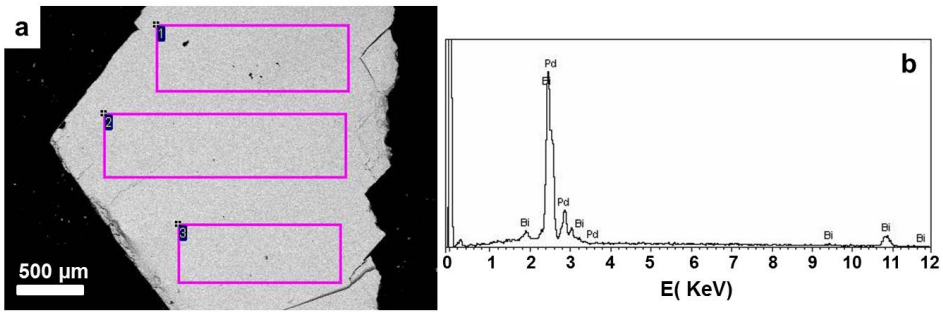

Figure 2.26: In a, a SEM image of an $\beta - Bi_2Pd$ crystal. The pink rectangles points the areas where different EDX spectres were measured. In b, the EDX spectra measured in the area marked with a 2 in the SEM image. Each peak of the EDX spectra is marked with the symbol of the corresponding element. The spectra at different areas of the crystal show a perfect match with the Bi_2Pd composition.

EDX experiments reveals and almost constant composition of $\approx 65at.\%$ of Bi and $\approx 35at.\%$ of Pd on the whole sample, pointing out the very good quality of our crystals. An example of the EDX spectra on the crystals is also presented in figure 2.26 b.

The superconducting vortex lattice in $\beta - Bi_2Pd$ at very low fields was measured during the thesis and our result will be presented in chapter 4.

2.4 Summary and conclusions

In conclusion, we have successfully implemented an experimental set up that allows us to perform AFM-MFM measurements between 1.8 K and 300 K, applying magnetic fields in any direction of the space up to 5 T in the Z direction and 1.2 T in the X and Y directions. With this set up, we have characterized the hysteresis cycle of MFM commercial probes as a function of the temperature from 1.8 to 300 K. We have also found that the MFM images of superconducting vortices show star-like features at vortex positions when the MFM tip is magnetized below its coercive field. In addition, during the thesis, single crystals of $\beta - Bi_2Pd$ were successfully grown via the solution growth method and characterized.

CHAPTER 3

Exfoliation and characterization of layered superconductors and graphene/superconductor heterostructures

3.1 Introduction

The pioneering work published by Novoselov et al. [135] gave rise to the isolation of single layers of graphene. They reported the repeated peeling of highly oriented pyrolytic graphite (HOPG) on a photoresist layer and the final release of the resulting thin flakes in acetone. This method was later improved with the *dry* exfoliation of several layered materials by simply pressing the surface of crystalline samples against different surfaces [136]. This basic methodology gave access to large surface area flakes of atomically-thin graphene and also to flakes of certain transition metals dichalcogenides (TMDCs) like the superconducting $NbSe_2$ or MoS_2 among others [3–6]. The technique was implemented in a variety of different ways under the generic name of micromechanical cleavage also known in informal terms as the *Scotch tape method*.

During the last decade a great variety of different mechanical cleavage methods were developed for the clean deposition of 2D materials on different surfaces. Among them, we can highlight micromechanical exfoliation techniques based on the use of

silicone stamps that do not present any glue on their surfaces that could contaminate the sample as in the case of the scotch tape method [137, 138].

2D superconductivity in thin films and flakes of crystals has attracted the attention of many researchers in the last decade [1–9]. For example, superconducting crystals like BSCCO or TaS_2 have been successfully exfoliated down to a single layer and deposited in a substrate in the past [10–12]. In addition, a lot of work has been done trying to induce superconductivity in graphene in contact with a superconductor due to the proximity effect [1, 2, 13–17].

During the thesis, we have used both, the silicone stamp method and the scotch tape method to prepare thin flakes of several superconductors and graphene. The main method employed was the silicon stamp method due to its of great simplicity, cleanness and relatively high efficiency. For BSCCO crystals, we used however the scotch method, as in this material it was easier to obtain large flakes with this method.

3.2 Micromechanical exfoliation

In order to transfer microscopic flakes of a macroscopic crystal on top of a substrate we have used Polydimethylsiloxane (PDMS) stamps, a well known viscoelastic material used to exfoliate and transfer crystal flakes in the last years [137, 138].

In this method, first, the PDMS stamp is gently placed on top of the crystal and an small pressure is applied by hand (figure 3.1 a and b). Then, the stamp is removed from the crystal surface with some flakes of the crystal attached to it (figure 3.1 c). Next, the PDMS stamp is placed on top of a the desired substrate applying again an small pressure by hand (figure 3.1 d). Finally, the stamp is removed, leaving small flakes of the crystal deposited on the substrate (figure 3.1 e). The PDMS stamp facilitates the accommodation of the crystal to the substrate when they are put in contact, thanks to its viscoelastic properties. It is important to note that the PDMS stamps do not have any glue on their surfaces, the crystals remains attached to the stamp due to its viscoelastic properties. Thus, the crystal flakes deposited with this technique are free of the contaminants that typically appear with the regular scotch

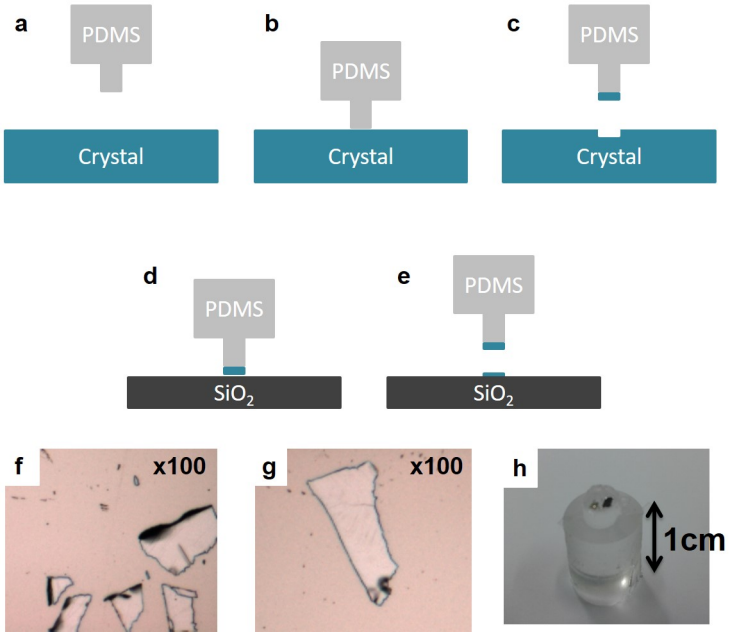

Figure 3.1: In a, b and c, we show the exfoliation process using a PDMS stamp. First, the stamp is gently pushed against the clean crystal surface and then they are separated. Some crystals flakes are attached to the stamp after separating it from the crystal. In d and e, we schematically show the deposition of the crystal flakes on top of a substrate. The PDMS stamp is pushed against the substrate and few flakes are deposited on top of it. In f and g, we show two optical images of arbitrary β-Bi_2Pd flakes deposited on a SiO_2 substrate. In h, we show a real picture of the PDMS stamp with some crystal flakes attached on top.

tape method [139]. A schematic representation of the exfoliation-transfer method is represented in figure 3.1 together with some pictures of the deposited flakes and the stamp.

After depositing the crystal flakes on top of a substrate, they are localized using an optical microscope using a combination of x10, x50 and x100 zoom lenses (figure 3.2 a and b). Then, the sample is moved to our room temperature AFM (RT-AFM) and the same area is localized with another optical microscope integrated with the RT-AFM (figure 3.2 c). Finally, the flakes are measured with the RT-AFM to determine their height.

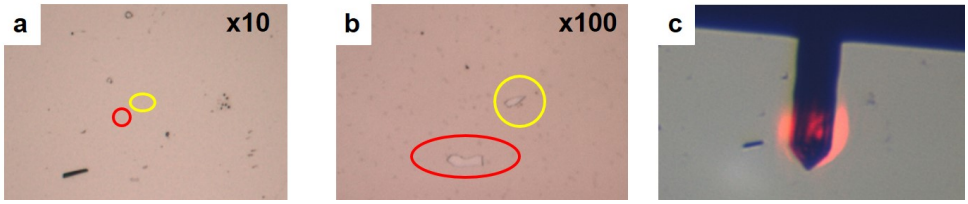

Figure 3.2: In a and b, we show two pictures of two β-Bi_2Pd flakes deposited on top of a SiO_2 substrate with zooms x10 and x100 respectively. In both images the position of the flakes are highlighted with yellow and red circles or ellipses. In c, the same area imaged with an optical microscope integrated with our RT-AFM showing the AFM cantilever above the area where the crystal flakes are deposited.

3.2.1 BSCCO on SiO_2

We have exfoliated BSCCO crystals down to a few layers and deposited them on a Si substrate with a SiO_2 layer of 300 nm on top, following the same procedure described in the previous section. We have successfully localized and measured a 25 nm thick flake at low temperatures under different magnetic applied fields in our LT-MFM.

3.2.1.1 Moderate magnetic fields

First, we have localized the flake at 10 K and measured its topography and magnetic profile under an applied magnetic field of 100 Oe in the out of plane direction, as is shown in figure 3.3. We have found that the magnetic profile was homogeneous in the whole field of view. This homogeneity can be understood as an increment in the size of the superconducting vortices in very thin samples proposed by Pearl in 1964 [140].

The main problem of magnetic images in thin superconducting material is the evolution of the penetration depth as the thickness of the superconductor decreases. The thin-film problem differs from the behavior of currents and vortices in bulk superconductors by the dominating role of the magnetic stray field outside the film. The interaction between vortices occurs mainly by this stray field, while in bulk superconductors the vortex currents and the vortex interaction are screened and thus decrease exponentially over the length λ [140–142].

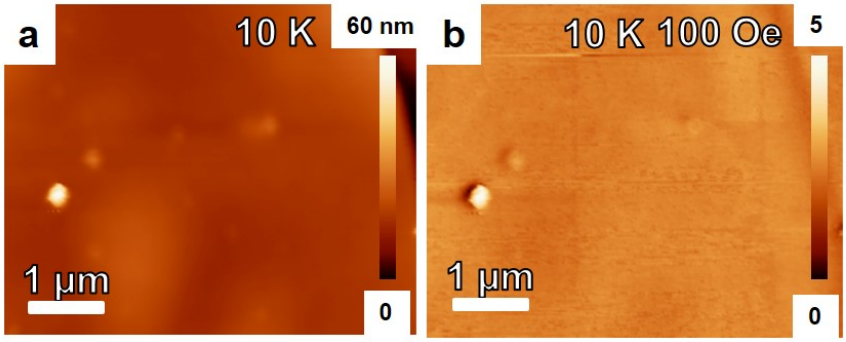

Figure 3.3: In a, we show the topographic image measured at 10 K of a BSCCO flake deposited on a SiO_2 substrate. In b, we show the corresponding magnetic image measured under an applied magnetic field of 100 Oe at 10 K. From the images is clear that the magnetic profile is homogeneous at the BSCCO flake surface.

If we consider one vortex in the center of a large circular film with infinite radius and in the limit of zero λ. The point vortex behaves like a magnetic dipole, composed of two magnetic monopoles: one above and another below the film. The magnetic field lines of this point-vortex are straight radial lines, all passing through this point. The magnitude of this magnetic stray field is $\phi_0/2\pi r^2$ above and $-\phi_0/2\pi r^2$ below the film. The magnetic field parallel to the film suffers a discontinuity and a sheet current circulates around the vortex with J $= \phi_0/\mu_0\pi r^2$. This result differs form the strong decay of screening currents of bulk superconductors, $J = \frac{\phi_0}{2\pi\mu_0\lambda^3}K_1(r/\lambda)$ [28], where K_1 is the first order modified Bessel function. In his original paper, Pearl found and effective penetration depth for superconductors when $d < \lambda$ (d the thickness of the superconductor). This effective penetration depth is $\Lambda = 2\lambda^2/d$. Where Λ is known as the *Pearl penetration depth.*

The expected penetration depth for a BSCCO crystal is $\approx$ 200 nm [143–145], in good agreement with our LT-MFM measurements in chapter 6. Therefore, for a flake 25 nm thick, a Pearl penetration depth of $\approx 5\ \mu m$ is expected. From equation 1.14, the intervortex distance at a magnetic field of 100 Oe is expected to be $\approx$ 500 nm. Thus, the magnetic profile on the superconductor is expected to become homogeneous, in good agreement with our measurements.

3.2.1.2 Very low magnetic fields

At very low fields, for example 1 Oe, the intervortex distance is expected to be $\approx$ 5 μm. This corresponds to the value of the Pearl penetration depth for our flake. Thus, at 1 Oe, the magnetic profiles of the superconducting vortices will not have such a strong overlap. The expected magnetic field variation will be of order of the applied magnetic field. However, it is difficult to achieve a magnetic resolution as good as 1 Oe in MFM. As an example, superconducting vortices between 50-100 Oe produces a displacement of the phase of the oscillation of about 1-5 degrees in our system. In addition, this signal also depends on factors such as the quality of the tip, the Q factor or the cross-talk with the electrostatic and topographic background in the MFM image.

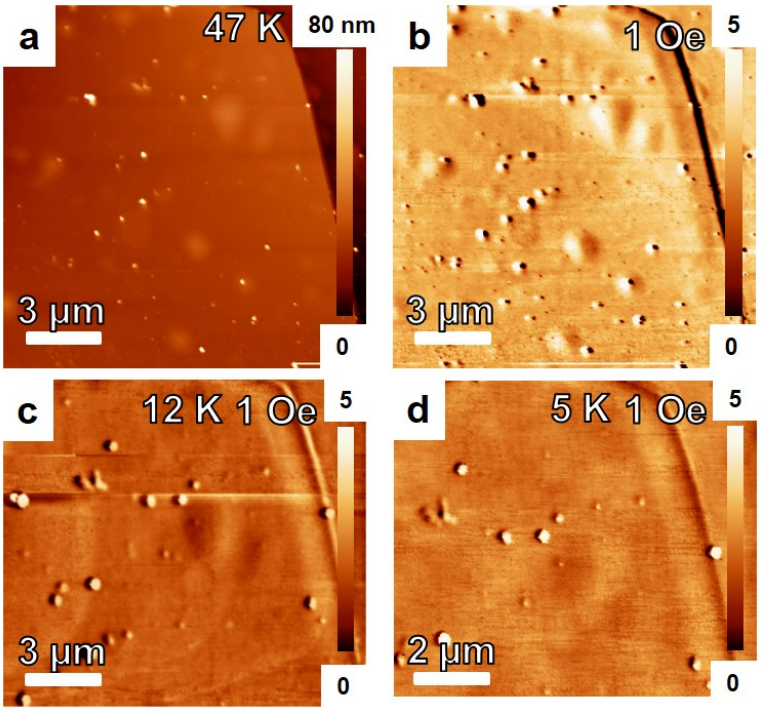

Figure 3.4: In a, we show the topographic image measured at 47 K on a BSCCO flake deposited on a SiO_2 substrate, showing some contamination deposited on the flake during the deposition. In b, c and d, the corresponding magnetic images measured under an applied magnetic field of 1 Oe at 47, 12 and 5 K respectively. The magnetic profile is homogeneous at the BSCCO surface at the three temperatures. There are only few inhomogeneities at the positions of the contaminations, probably related with the cross-talk between magnetic and topographic signal.

We have imaged again the magnetic profile of the same flake at very low applied magnetic fields (1 Oe) and different temperatures. Our results are summarized in figure 3.4 and 3.5. In figure 3.4, we show three magnetic images with a magnetic field of 1 Oe at 47, 12 and 5 K together with the corresponding topographic image. As it is clear from the images, the magnetic profiles are homogeneous in the whole field of view at the three temperatures, presenting only small variations probably of non-magnetic origin and related with the contamination deposited on top of the flake during the exfoliation. The homogeneity of the magnetic profiles indicates that besides all our efforts, our magnetic resolution is not good enough to allow single vortex resolution at 1 Oe. From the images is clear that the cross-talk with the topographic profile of the sample is stronger that the magnetic signal.

We have also measured a region where the edge of the BSCCO flake and the SiO_2 substrate are clearly visible to determine if there is any measurable screening of the magnetic field in the superconducting flake with respect to the substrate. Our results are presented in figure 3.5. The magnetic image in figure 3.5 shows that the magnetic profile is homogeneous in the whole field of view. There is not measurable difference between the region occupied by the superconductor with respect to the substrate. There is only some contrast in the magnetic image at the positions of the edge of the BSCCO flake and of a longitudinal topographic feature in the right part of the image, due to the cross-talk with the topographic profile at this locations.

Unfortunately, the screening of the magnetic field in the superconducting flake with respect to the substrate is below our experimental resolution at this thickness. Thus, we were not able to measure the existence of Pearl vortices or another superconducting effect related with the thickness in our experiments on BSCCO. Nevertheless, we were able to deposit thin flakes of this material and localize them at low temperatures opening the possibility for further experiment in BSCCO flakes of different thicknesses in the future.

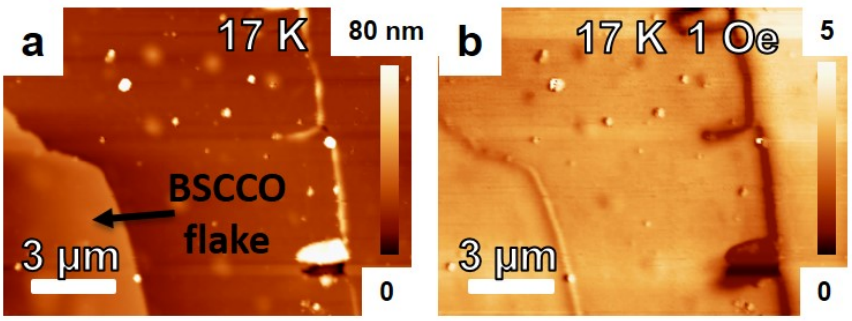

Figure 3.5: In a, we show the topographic image measured at 17 K of the edge of the BSCCO flake (left) and the SiO_2 substrate (right). In b, we show the corresponding magnetic image measured under an applied magnetic fields of 1 Oe at 17 K. From the image is clear that the magnetic profile is homogeneous at the BSCCO flake and at the substrate, indicating that there is not a measurable difference in the magnetic field between the two systems. There is only contrast at the edge of the flake and at the position of longitudinal topographic feature on the right of the image due to the cross-talk with the topographic profile.

3.2.2 β-Bi_2Pd on SiO_2

As it will be shown in chapter 4, β-Bi_2Pd is a layered compound that can be easily exfoliated using the regular scotch tape method. In contrast with layered crystals that were successfully exfoliated down to a single monolayer, the layers of β-Bi_2Pd are not weakly coupled via Van de Waals interactions but strongly coupled via covalent bonds [146]. Nevertheless, a recent theoretical work shows that the bonds between Bi layers in the crystal are much weaker that the Bi-Pd or Pd-Pd bonds and therefore, the crystal is expected to cleave in this planes. This theoretical calculation was demonstrated experimentally by [23] and [24] and also corroborated in this thesis in chapter 4. We have tried to exfoliate our β-Bi_2Pd crystals to the minimum possible thickness to open the possibility of studying superconductivity in the 2D limit.

3.2.2.1 Exfoliation down to few tens of nanometers

Using the PDMS stamp method described before, we have successfully deposited several β-Bi_2Pd flakes of different thickness on SiO_2 substrates, as is shown in figure

3.6.

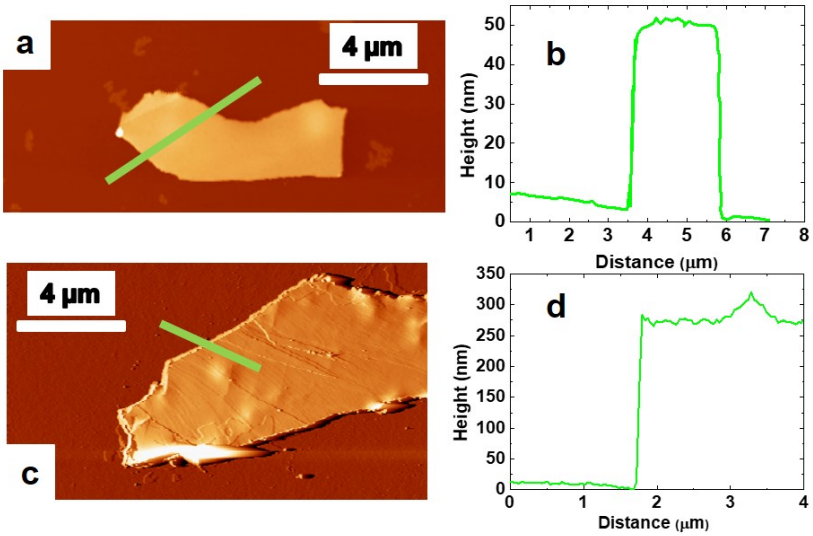

Figure 3.6: In the left panel, two AFM images of two β-Bi_2Pd flakes deposited on top of a SiO_2 substrate. In the right panel, the corresponding topographic profiles marked as green lines on the images in the left. The images show the possibility of depositing flake of β-Bi_2Pd of different thicknesses.

In the image, two examples of β-Bi_2Pd flakes are presented, one thick flake of several hundreds of nanometers and a thin flake of just some tens of nanometers. The thin flake reveals that it is possible to exfoliate a β-Bi_2Pd single crystal down to very small thicknesses. Unfortunately, the density of thin flakes of β-Bi_2Pd that we achieved with the stamp method was not enough to allow us to localize one of these flakes at low temperatures. The thermal drift of our LT-MFM prevents us to locate a β-Bi_2Pd flakes at low temperature despite all our efforts. More work is need in this direction to investigate the superconducting behavior of β-Bi_2Pd thin flakes. In particular, improving the deposition technique to increase the ratio of success and reduce the thermal drift of the microscope are of particular interest in this or any other system in form of flakes of small lateral sizes.

3.2.3 Graphene on β-Bi_2Pd

We have successfully exfoliated several graphene and few-layers-graphene (FLG) flakes and deposited them on top of a single crystal of the superconductor β-Bi_2Pd. The

flakes were characterized with our RT-AFM after localizing them with an optical microscope. An example is shown in figure 3.7, where three pictures at different magnifications are presented together with a topographic AFM image. The AFM topographic measurements show a combination of several FLG flakes at the edge of the big graphite flake.

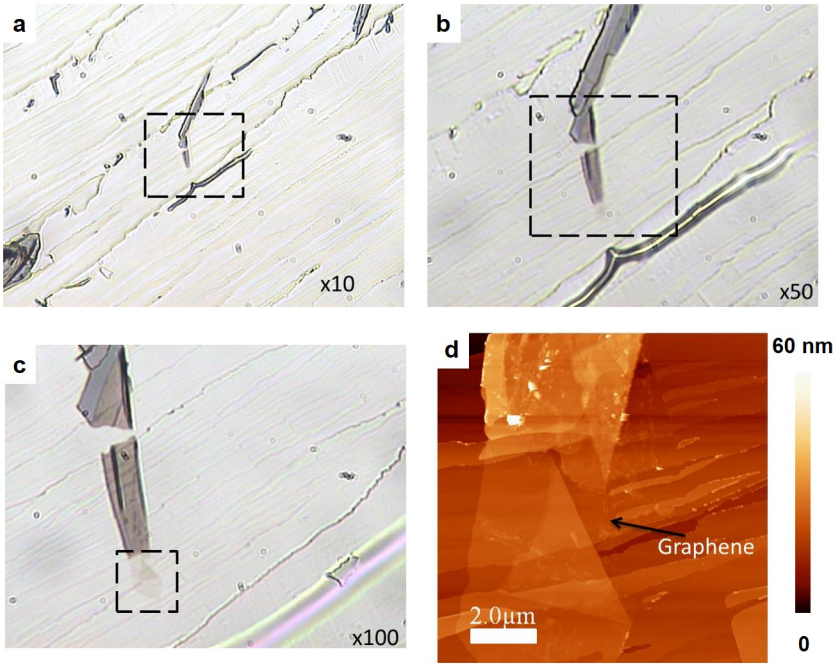

Figure 3.7: In a b and c, three optical images with magnifications x10, x50 and x100, used to localize the graphene flakes deposited on to of the β-Bi_2Pd crystal. In d, the corresponding topographic image of the area highlighted with a black square in c. It shows flakes with different thicknesses with a graphene flake marked with a black arrow

3.2.3.1 Friction measurements

It is know that graphene has lubricant properties [147]. TThis facilitates the location of the flakes via friction images, as the contrast in friction images between graphene, FLG and the substrates is often large [148]. For this reason, we have performed a combination of topographic and friction measurements at the same flake to localize the different graphene or FLG flakes.

The physical basics of the friction measurements in AFM are as follows. When

scanning in the contact mode at a constant force, besides the cantilever's deflection in the normal direction, an additional torsion of the cantilever takes place. When moving over a flat surface with zones of different friction factors, the angle of torsion will be changing in every new zone. This allows measuring of the local friction force (for a detailed study of friction measurements in AFM see reference [120]).

In figure 3.8 b, there are several FLG flakes on the right of the image that are not easily visible in the topographic image. They appear as a clear dark contrast in the friction image. In our case, we have not found mayor differences between friction images on graphene and FLG on top of the β-Bi_2Pd crystal, probably due to surface contamination during the exfoliation-transfer method. Friction images do not allow us to distinguish between graphene or FLG flakes on top of β-Bi_2Pd but is still the best technique to quickly localize FLG flakes on top of β-Bi_2Pd that are not visible in the topographic image.

3.2.3.2 Kelvin Probe Microscopy (KPM) measurements

We have used a different approach to establish a experimental procedure that unambiguously distinguishes between graphene and FLG flakes deposited on β-Bi_2Pd. We have performed Kelvin Probe Microscopy (KPM) measurements on the same flake to characterize the surface potential difference between the β-Bi_2Pd substrate, graphene and FLG flakes. KPM is a tool that enables nanometer-scale imaging of the surface potential of a broad range of materials. KPM measures the Surface Potential Difference (SPD) between a conducting tip and the sample.

$$V_{SPD} = \frac{\phi_{tip} - \phi_{sample}}{-e} \tag{3.1}$$

Where ϕ_{tip} and ϕ_{sample} are the work functions of the tip and the sample (for a more detailed study of the KPM see reference [120]).

In figure 3.8 c and d, KPM maps at the same areas that the topographic and friction images are shown. In this case, is clear that the difference in surface potential

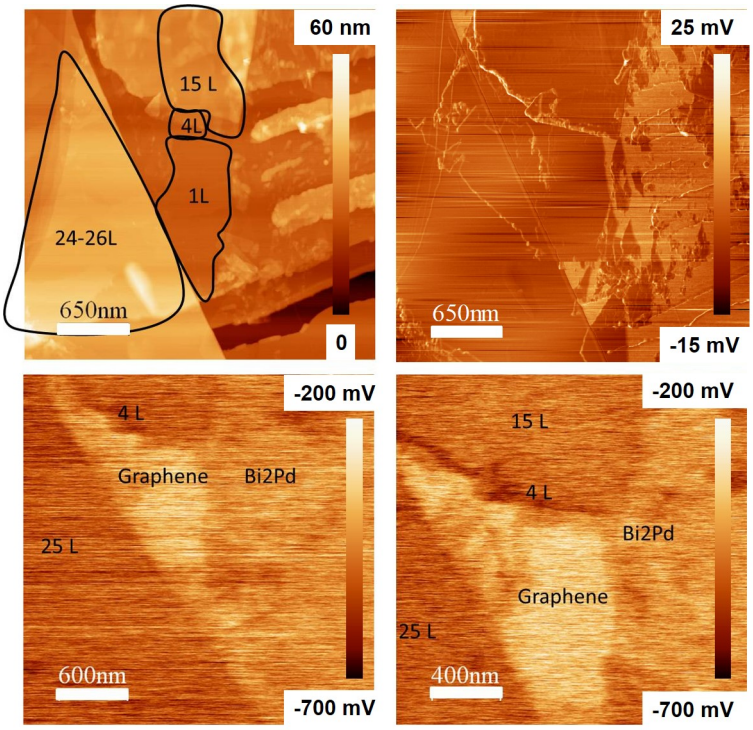

Figure 3.8: In a, a topographic image of some graphene flakes with different thicknesses, from 25 to 1 layers. The area occupied by different flakes is approximately marked with black lines. In b, the simultaneous friction map showing two different regions, one on top of the graphene flakes (dark area) and another corresponding to the β-Bi_2Pd crystal (bright area). In c and d two KPM images revealing a clear contrast between the β-Bi_2Pd crystal, the single layer graphene flake and thicker graphene flakes.

between graphene, different FLG flakes and β-Bi_2Pd is measurable. More important, the surface potential in a single layer graphene is higher that the surface potential of the β-Bi_2Pd crystal and the surface potential of thicker flakes is higher that in the β-Bi_2Pd. This allows to unambiguously distinguish between single layer graphene and thicker flakes by simply comparing the value of the surface potential of a flake and the β-Bi_2Pd substrate.

KPM surface potential measurement are often affected by adsorbates on the surfaces of study. As oxygen, hydrogen and another adsorbates present in the atmosphere attached to the graphene and β-Bi_2Pd surfaces. For this reason, we have sealed our AFM in a crystal chamber with a continuous flux of Nitrogen for several hours to minimize humidity effects. Nitrogen flux is expected to dramatically decrease the

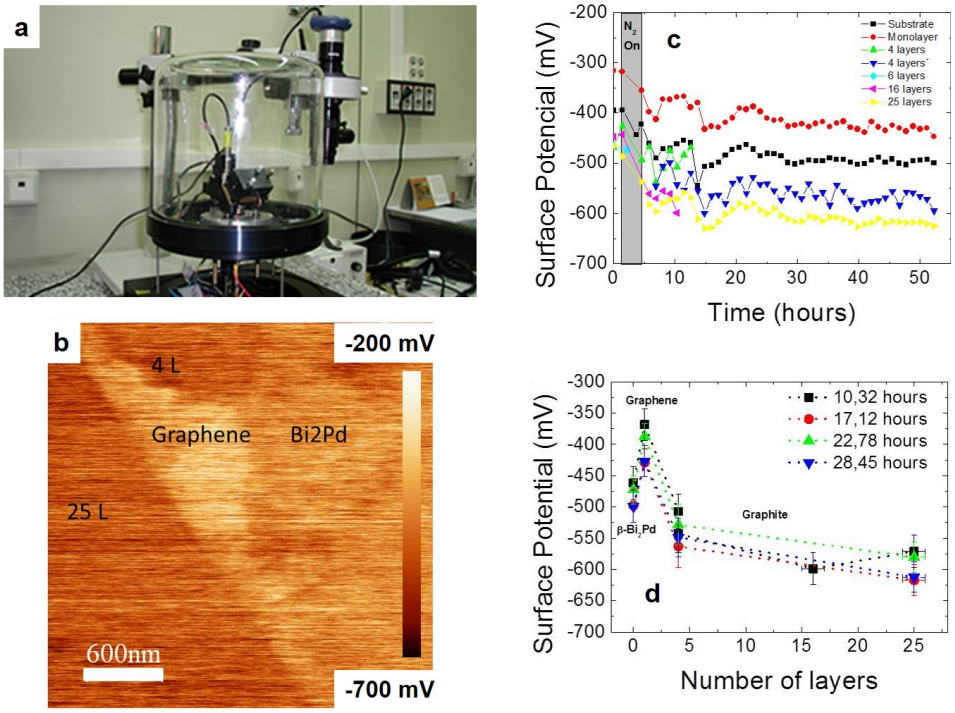

Figure 3.9: In a, our RT-AFM with the crystal chamber used to control the ambient humidity with the N_2 flux. In b, a KPM image measured during the experiment as an example. In c, the evolution of the surface potential for the substrate (β-Bi_2Pd), graphene and FLG after decrease the humidity of the sample chamber by applying a constant flux of N_2. The moment when the N_2 flux was switch on is marked in gray. In d, the evolution of the surface potential of the same system as a function of the number of layers of graphene for four different times after decreasing the humidity. Both plots show that the surface potential difference between the β-Bi_2Pd, the graphene and the FLG remains almost constant with the time.

humidity inside the crystal chamber and partially remove the adsorbates from the sample. We have maintained the Nitrogen flux for 50 hours, performing several KPM measurement during the process. We have found that the Surface potential of all FLG, graphene and β-Bi_2Pd decreases with the time and approaches an stable value after turning on the N_2 flux. After reaching a stable value, the difference between the surface potential of the different flakes and the β-Bi_2Pd substrate, is almost the same than before, showing that this technique allows to localize graphene flakes even at ambient conditions with contaminants deposited on the surface. The results of this experiment are summarized in figure 3.9.

Our results shows that KPM a suitable experimental microscopic technique to individual localize graphene flakes on top of the superconductor β-Bi_2Pd. By contrast friction maps have probed to be a valuable tool to localize graphene and FLG flakes on top of β-Bi_2Pd but no dot allow to unambiguously determine the number of graphene layers.

3.3 Conclusions

In conclusion, we have successfully exfoliated several superconducting crystals and graphene and deposit them in different substrates using a combination of PDMS silicon stamps and the regular scotch tape method. We have investigated three different system with this method, BSCCO on SiO_2, β-Bi_2Pd on SiO_2 and graphene and FLG on β-Bi_2Pd.

In the case of BSCCO flakes deposited in SiO_2, we were able to measure one thick flake at low temperatures and characterize its magnetic profile in the superconducting state at different magnetic fields and temperatures. We have found that the screening of the magnetic field in this flakes is bellow our experimental resolution at moderate (100 Oe) and very low fields (1 Oe).

For β-Bi_2Pd flakes deposited on SiO_2, we were able to exfoliate and deposit flakes of this system for the very first time, down to some tens of nanometers. These results open the possibility to study the superconducting behavior in the 2D limit in this system in the future.

We have also transferred graphene and FLG flakes on top of a β-Bi_2Pd single crystal and developed a experimental procedure to unambiguously localize graphene and FLG flakes on top of β-Bi_2Pd using a combination of friction and KPM measurements with an AFM. We have also probed that this method allow to localize the flakes at ambient and at low humidity conditions.

CHAPTER 4

Vortex lattice at very low fields in the low κ superconductor $\beta - Bi_2Pd$ and $\beta - Bi_2Pd/graphene$ heterostructures

4.1 Introduction

Historically, magnetic microscopy techniques have been of huge importance in the study of superconducting materials. The first visualization of the vortex lattice was achieved by Essman and Trauble [149] in Pb by Bitter magnetic decoration in 1967 (figure 4.1 a). The Bitter decoration technique consists in depositing small magnetic particles on the surface of the superconductor. Under a magnetic field, the magnetic particles arrange at the positions of the flux lines, indicating the location of individual vortices. Bitter decoration was also the first technique used to visualize the vortex lattice in high T_C superconductors in 1987 by Gammel et al. [150] in YBCO (figure 4.1 b). The MFM was used for first time to measure the vortex lattice in a superconductor in YBCO by Moser et al. [151] in 1995 (figure 4.1 c).

A few pioneering works of magnetic bitter decoration have studied the *intermediate state* in Type I and the *intermediate mixed state* (IMS) in Type II superconductors, proving the coexistence between domains of normal and Meissner state in type I and between Meissner and mixed state in type II superconductors [37, 39, 40, 152, 153].

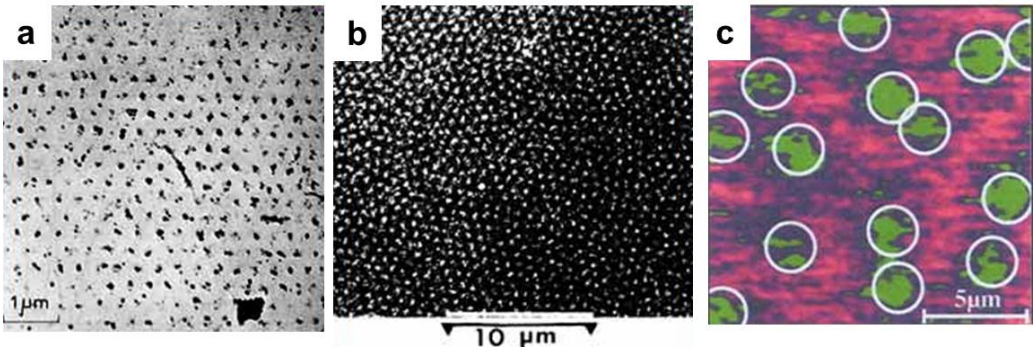

Figure 4.1: a shows the first magnetic image of superconducting vortices reported in 1967, it was obtained by bitter decoration technique in Nb. Black dots points the position of the vortices, revealing an hexagonal lattice. b shows the first visualization of the vortex lattice in a High Tc superconductor (YBCO) in 1987, also by bitter decoration technique. White dots points the position of the vortices. c shows the first image of superconducting vortices measured by MFM in YBCO in 1995. Vortices are shown as green spots, in this case showing disordered arrangement. Images from references [149] [150] and [151]

4.1.1 Single and multi band superconductors in the IMS

At fields below H_{c1}, in type II superconductors, the internal magnetic field can be strongly inhomogeneous. Because of the full flux expulsion of the Meissner state, demagnetizing effects can dominate the magnetic field behaviour. The sample separates into domains with zero induction $B = 0$ and an induction close to $\mu_0 H_{c1}$ between $(1-N)\mu_0 H_0 < \mu_0 H < \mu_0 H_0$ [37].

Thin films of Nb, TaN, PbIn and other materials show a IMS [37–40]. In high quality single crystal of Nb with $\kappa = 1.1\sqrt{\frac{1}{2}}$, flux expulsion coexists with regions showing a vortex lattice. Small angle neutron scattering finds exactly the intervortex distance expected at H_{c1} in the vortex domains [39]. The area occupied by the domains with zero induction decreases linearly with the magnetic field, so that the magnetic induction reaches the value corresponding to the mixed phase [39, 40]. The morphology of the IMS domains is mainly governed by geometric barriers preventing domain nucleation [153], surface barriers which hamper the entrance of flux lines into the sample [154, 155], vortex lattice (VL) anisotropies [39] as well as pinning forces [156]. A few selected images of different domains geometries in the intermediate

mixed state in Nb are presented in figure 4.2. Nb has a highly complex Fermi surface with three bands crossing the Fermi level [39].

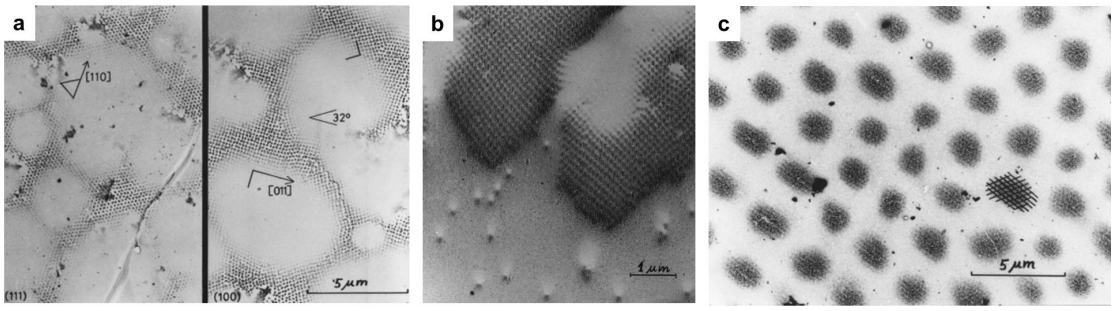

Figure 4.2: Different domains morphologies in the IMS observed in Nb by bitter decoration technique. In a, a high purity Nb disk 1 mm thick, 4 mm diameter, at 1.2 K and 600 Oe ($H_{c1} = 1400$ Oe). Round islands of Meissner phase are surrounded by a regular vortex lattice. In b, a square disk 5 × 5 × 1 mm^3 of high purity polycrystalline Nb at 1.2 K and 1100 Oe. Magnetic flux penetrates from the edges in form of fingers which are composed of vortex lattice. In c, high-purity Nb foil 0.16 mm thick at 1.2 K and 173 Oe. It shows round islands of vortex lattice embedded in a Meissner phase. Images adapted from [40, 157].

Recently, the interest in the IMS in low-κ superconductors has been renewed thanks to the advances in the studies of new materials and visualization techniques. SHPM experiments have shown vortex chains and clusters in ZrB_{12} ($0.8<\kappa<1.12$) at very low fields [18]. SHPM measurements showed two different behaviours in ZrB_{12}, one at temperatures close to T_C, characterized by an Abrikosov lattice with a first neighbour distance, $d = (0.75)^{1/4}\left(\frac{\Phi_0}{B}\right)^{1/2}$ and another at lower temperatures characterized by the formation of vortex clusters and stripes with first neighbour distances almost independent of the magnetic field.

Authors in [18] claim that the formation of vortex chains and clusters arises from the combined effect of quenched disorder and the attractive vortex-vortex interaction in the type-II/1 phase at lower temperatures. They observed that at the clusters, non-pinned vortices tend to form the triangular arrangement with pinned vortices at the centre (figure 4.3). The averaged first-neighbour distance inside the cluster exhibits a very weak dependence on the external field (figure 4.3). They associated the regular Abrikosov lattice observed at higher temperatures with the type-II/2 phase dominant at these temperatures.

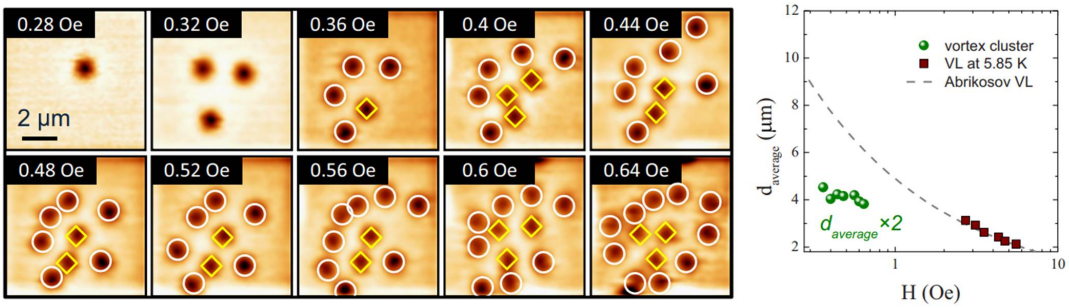

Figure 4.3: Vortex cluster formation in ZrB_{12}. In the left panel, SHPM images observed at 4.2 K after FC with progressively increasing magnetic fields, showing the formation of a vortex cluster. The symbols indicate the location of the vortices. Squares points the position of vortices pinned on defects and circles of vortices not pinned on defects. In the right panel, averaged nearest-neighbour distance as a function of the applied magnetic field for the vortex cluster (green circles). The nearest-neighbour distance for the VL at 5.85 K is shown by the squares, which follows the triangular arrangement of the Abrikosov VL (dashed line). Adapted from [18]

On the other hand, 2H-$NbSe_2$ and MgB_2 show two superconducting gaps. In MgB_2, interband interactions are weak, whereas they appear to be stronger in $NbSe_2$ [158–160]. Both are extreme type II superconductors, with $\kappa \gg \frac{1}{\sqrt{2}}$ [161]. Several experiments to characterize the vortex lattice below H_{C1} have been done in these two materials using different magnetic microscopic techniques [19–21].

Bitter decoration studies at very low fields showed a remarkable different behaviour between 2H-$NbSe_2$ and MgB_2 [19]. Decoration measurements in 2H-$NbSe_2$ show a distorted hexagonal lattice (figure 4.4 a) while in MgB_2, they show vortex accumulation in clusters at H=1 Oe and in stripes at H=5 Oe (figure 4.4 b and c). Clusters and stripes are separated by vortex free areas, whose size is of a few intervortex distances. Further Scanning SQUID measurements in MgB_2 showed accumulation of vortices in clusters with an intervortex distance almost independent of the magnetic field [21]. Moreover, SHPM measurements at very low fields showed a hexagonal lattice for $NbSe_2$ with the intervortex distance expected for the applied magnetic field (figure 4.5 a and b) and vortex accumulation in clusters and stripes in MgB_2 [20] (figure 4.5 c and d).

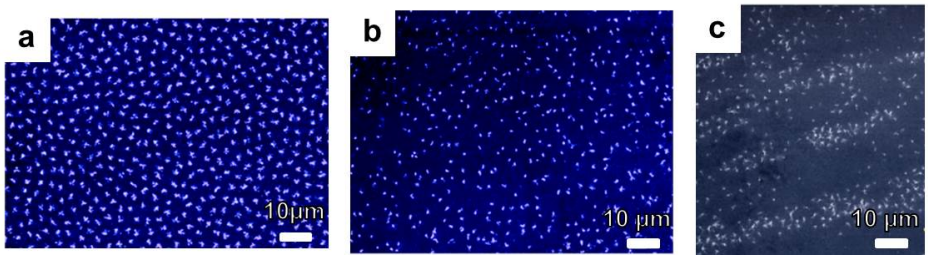

Figure 4.4: Bitter decoration images of the vortex structure at very low fields in 2H-$NbSe_2$ and MgB_2. Vortex positions are shown as white dots on the blue background. In a, vortices in $NbSe_2$ in a distorted triangular lattice at T = 4.2 K and H = 1 Oe. In b, vortices in MgB_2 are accumulated in clusters at T = 4.2 K and H = 1 Oe. In c, vortices in MgB_2 are accumulated in stripes at T = 4.2 K and H = 5 Oe. Images adapted form [19].

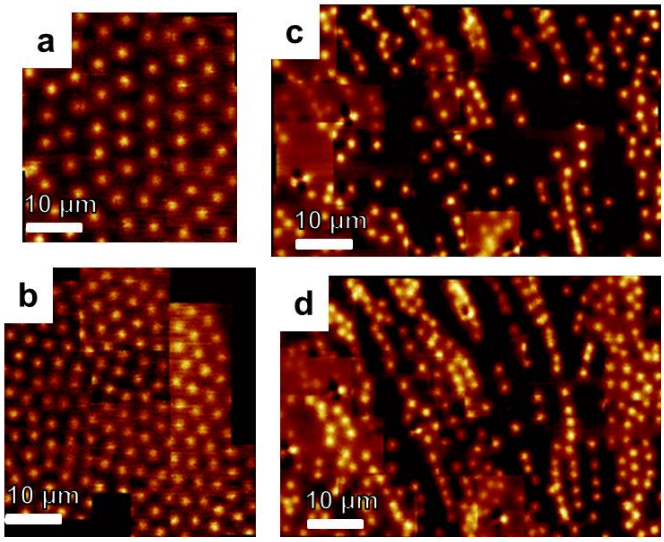

Figure 4.5: Scanning Hall Microscopy images of the vortex structure at very low fields in 2H-$NbSe_2$ and MgB_2. In a and b, SHPM images of a distorted triangular vortex lattice in $NbSe_2$ at 4.2 K and 2 Oe. In c and d, SHPM images of stripes and clusters of vortices in MgB_2 at 4.2K and 2 Oe.

The hexagonal lattice found in 2H-$NbSe_2$ was ascribed to vortices nucleated in the mixed state at temperatures where $H_0 = 0$[20]. Vortices are formed at high temperatures, when $H_{c1}(T)$ is negligible and remain trapped when cooling. Vortices then, form hexagonal lattice with a first neighbour distance, $d = (0.75)^{1/4}\left(\frac{\Phi_0}{B}\right)^{1/2}$ and are retained at low temperatures by surface barriers [162]. No vortex free areas have been reported in 2H-$NbSe_2$.

Authors in [19–21] propose that the existence of vortex free areas between cluster and stripes in MgB_2 can be explained in term of a new state that they called Type 1.5 superconductivity, based on the semi-Meissner state predicted by [163]. They argue that the two gaps of MgB_2 have different λ and ξ and subsequently different κ, one below $\sqrt{\frac{1}{2}}$ and another above $\sqrt{\frac{1}{2}}$. As a consequence, the vortex-vortex interaction is the result of the competition between short-range repulsion and long-range attraction. This, leads to the appearance of vortex clusters and stripes. They also argue that the vortex stripes are independent of the crystal lattice and therefore they can not be related to pinning due to topographic features.

A recent theoretical work has proposed that the vortex patterns in MgB_2 can be also explained as a result of the interplay between repulsive-attractive vortex-vortex interaction, due to vortex-core deformations and pinning [22].

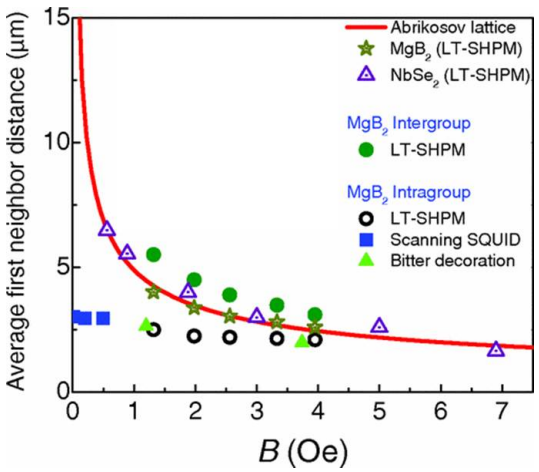

Figure 4.6: Plot of the theoretical and experimental values of the intervortex distances in $NbSe_2$ and MgB_2 obtained by different techniques at very low fields. Intervortex distances in $NbSe_2$ show good agreement with the expected Abrikosov lattice (red line). Vortices in MgB_2 show two different intervortex distances, one intergroup distance which agrees with the expected evolution of the Abrikosov lattice and another intragroup distance which remains almost independent of the magnetic field. Adapted from reference [20].

Figure 4.6 summarizes intervortex distances obtained from the experiments mentioned above in $NbSe_2$ and MgB_2. In $NbSe_2$, the intervortex distance fits the expected evolution with the applied magnetic field for an Abrikosov lattice. The intervortex distance in MgB_2 is separated in two groups, the intragroup and the intergroup dis-

tances. The intragroup distance remains almost constant when changing the magnetic field while the intergroup distance follows the expected behavior of the Abrikosov lattice [20].

Comparatively, $\beta-Bi_2Pd$ has a small, yet sizable, value of $\kappa \approx 6$. It has very weak pinning and is a single gap isotropic superconductor [23–25].

4.1.2 Previous works on $\beta - Bi_2$Pd crystals

In 2012 Imai et al. [164] grew $\beta - Bi_2Pd$ single crystals and suggested the possibility of a multigap behaviour. Their macroscopic measurements appeared to be consistent with multigap superconductivity. Their specific heat measurements showed a peculiar behaviour below T_C when changing the temperature, similar to the observed in the two gap superconductors MgB_2 and $Lu_2Fe_3Si_5$ (the magnitude of the discontinuity at T_C, a fast increase at low-temperature and a small shoulder in between) [165–167] (figure 4.7 b). Moreover, their H_{C2} measurements as a function of temperature were also consistent with the two gap scenario as they showed positive curvature near the critical temperature similar to other multi-gap superconductors [168–171] (figure 4.7 c).

The results mentioned in the last paragraph can be explained as follows. The curvature of the upper critical field is due to the presence of a surface sheet that influences the resistive transition [25] and the curvature of the specific heat probably due to the difficulties associated to the extraction of the superconducting specific heat from the phonon component, as the measurements in [25] suggest. Thus, beta-Bi2Pd is clearly a superconductor with a single gap value.

4.1.2.1 STM and specific heat measurements

Recent STM and specific heat measurements performed in $\beta - Bi_2Pd$ single crystals grown in the LBTUAM have probed the single gap behaviour of $\beta - Bi_2Pd$ [23, 25]. STM measurements were done by Dr. Edwin Herrera at the LBTUAM and specific

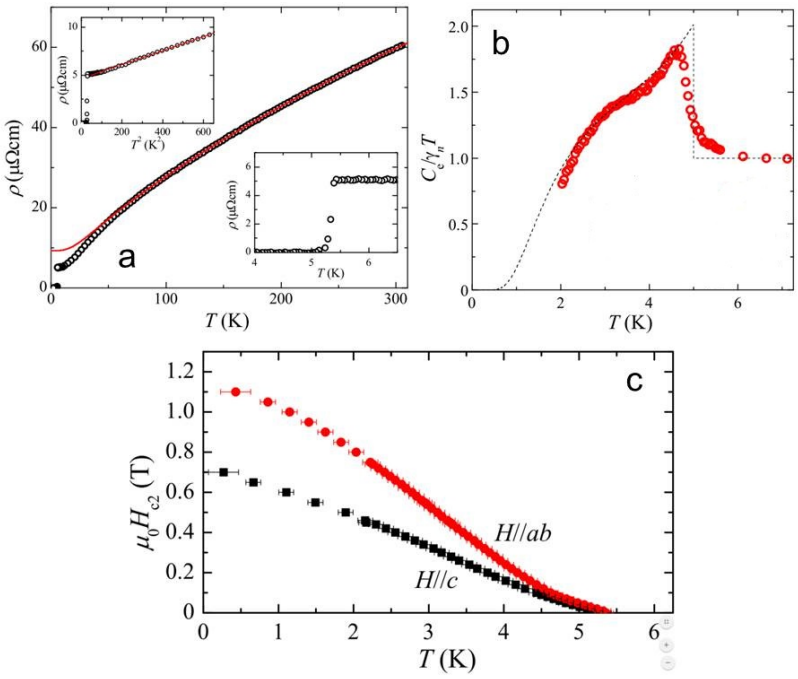

Figure 4.7: In a, the evolution of the resistivity with the temperature for $\beta - Bi_2Pd$ obtained by [164]. Insets show ρ near T_C and ρ at temperatures lower than 25 K plotted as a function of T^2. Black circles represents the experimental data and red line a fit proportional to T^2. b shows the behavior at low temperatures of the normalized electronic specific heat at zero field. The red circles are the experimental data and the dashed black curve was calculated using the two-band model [164]. In c, the evolution of the upper critical field with the temperature [164]. It was later shown [25] that these results do not represent the bulk behavior of this system, as discussed in the text.

heat measurements were done by the group of Prof. Peter Samuely at the *Centre of Low Temperature Studies* in Slovakia. Both measurements were done in $\beta - Bi_2Pd$ samples of the same series that we have grown and measured in this work (see section 2.3). In figure 4.8 a the evolution with the temperature of the normalized experimental tunnelling conductance in $\beta - Bi_2Pd$ is presented, together with the evolution of the superconducting gap with the temperature extracted from it (Figure 4.8 b). Both, conductance measurements and gap evolution are consistent with a single gap BCS superconductor with $\Delta = 0.76$ meV [23]. The specific heat represented in figure 4.8 c was obtained using an ac technique [172, 173]. The electronic contribution of the specific heat perfectly fits the BCS single gap theory [25]. The fit reproduces very well the jump at the anomaly and the shape of the experimental curve. In the data

there is no signature of an additional second gap.

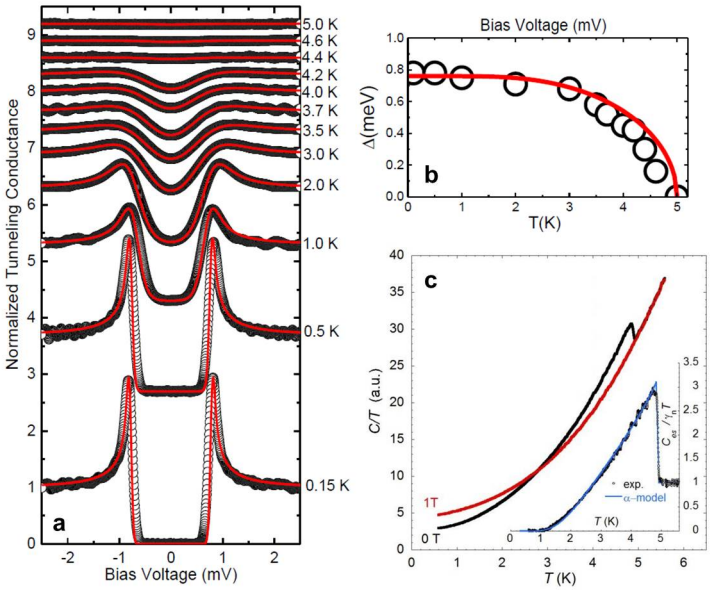

Figure 4.8: In a, the normalized tunnelling conductance curves for $\beta - Bi_2Pd$ at different temperatures are presented. Experimental data (black circles) matches the BCS single gap fit (red line). The evolution of the superconducting gap obtained from the curves in a is shown in b (black circles), matching the prototypical BCS single gap behaviour (red line). In c the evolution of the specific heat with the temperature at 0 and 1 T [25]. The inset shows the normalized electronic specific heat showing the sharp jump in the superconducting transition. The continuous blue line is the theoretical curve based on the BCS theory. Adapted from references [23, 25].

In a recent STM experiment in epitaxially grown thin films, authors find superconducting properties that are very different from the bulk behaviour [174]. The critical temperature is somewhat larger and two gaps appear in the tunnelling conductance. Furthermore, a zero bias peak appears in the centre of the vortex cores, indicating the formation of vortex bound states [158, 175, 176]. Authors argue on the basis of the spatial dependence of the tunneling conductance curves, that these states could be topologically non-trivial.

4.1.2.2 Fermi Surface

The first calculation of the electronic band structure and Fermi surface (FS) in $\beta - Bi_2Pd$ were made by Shein and Ivanovskii [146] (figure 4.9 a), finding that the Pd 4d and Bi 6p states are responsible for the metallic character of the material. They studied the system with and without spin orbit coupling (SOC) determining that the effect of the SOC is of minor importance. The FS can be divided in four main structures: a 2D hole-like deformed cylinder parallel to the K_z direction (green colour in 4.9 a), a hole-like pocket centred in the Γ -point, electron-like 3D pockets overlapping the 2D hole like deformed cylinder and one pocket inside the 3D electron like pockets (yellow in 4.9 a) [146]. FS calculations have probed that there are anisotropies of chemical bonding which causes that Bi/Bi layers are less coupled than Bi/Pd layers. This result is also consistent with STM topographic measurements of [23] and with our own result as it will be discussed.

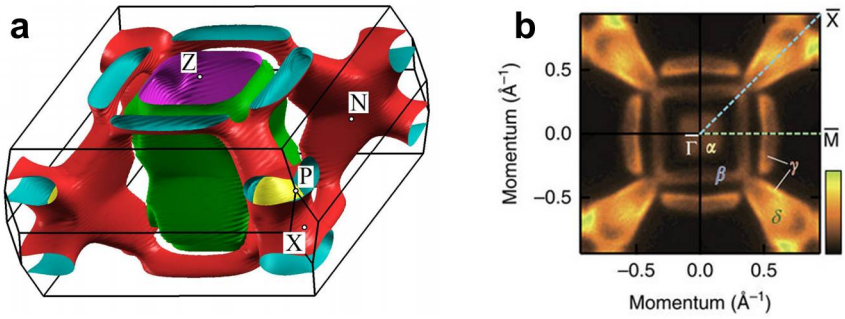

Figure 4.9: In a, the calculated Fermi surface of $\beta - Bi_2Pd$ is shown with the first Brillouin zone [146] and in b, the Fermi surface of $\beta - Bi_2Pd$ recorded by angle-resolved photoemission spectroscopy (ARPES). Two electron-like and two hole-like Fermi surfaces are denoted by α, β and γ, δ, respectively [177].

A following work [177] has also found topological protected states in $\beta - Bi_2Pd$ using angle-resolved photoemission spectroscopy (ARPES). The FS obtained by ARPES mostly agrees with the calculations of [146]. The resulting FS obtained in [177] is presented in figure 4.9 b. It represents the projection in the K_x-K_y plane of the 3D FS. Photoemission reveals a Dirac cone well below the Fermi level[177]. Spin resolved measurements provide polarized bands close to the Dirac cone. The same authors suggest that topologically non-trivial spin polarized bands crossing the Fermi level

might rise up to the surface. Moreover, a recent experimental work has proposed the existence of topological p-wave superconductivity at the surface [178].

4.2 MFM and SOT characterization

Previous works have studied the bulk properties and the vortex lattice at high fields with STM [23, 24]. However, prior to our work, the study of the vortex lattice below and near H_{C1} has not been reported yet. This was our main motivation and the starting point of our study in this compound.

4.2.1 Topographic characterization

For topographic characterization of the sample, AFM measurements were made in a disk like sample approximately 1 mm thick and 1 cm radius, glued with low temperature silver epoxy to our LT-AFM sample holder and exfoliated at room temperature using scocht tape. Topographic measurements were taken using the dynamic mode described in section 2.1.3.7.1 with typical sample tip separation around 10 nm.

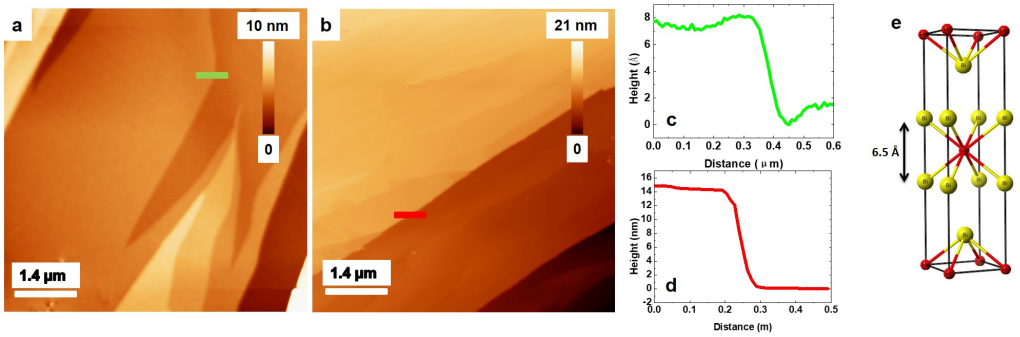

Figure 4.10: Different areas of the $\beta - Bi_2Pd$ crystals after exfoliation with scotch tape at RT. Both images were measured at 2K. In c and d, the topographic profiles corresponding to the green and red lines in the a and b images are shown. Image a has atomic flat areas separated by steps of few Armstrongs while b has steps up to tens of nanometres. In e, the unit cell of $\beta - Bi_2Pd$ with the distance between Bi layers highlighted.

After exfoliation, the sample presents a combination of very clean areas with flat terraces and atomic steps and areas with steps up to some tens of nanometres. The atomic flatness of the surface makes it a very good candidate to SPM measurements including MFM. Figure 4.10 a and b show two $7 \times 7 \mu m^2$ topographic images measured at 2 K. In c, the profiles of the green and red lines on the images are shown. The heigh of the step marked with the green line corresponds with the distance between Bi atoms in the unit cell as it is shown in figure 4.10 e, pointing out that the surface is terminated by Bi as it was observed in STM measurements by [23]. The flatness of the sample allows measuring, at 2K, areas up to $10 \times 10 \mu m^2$ large.

4.2.2 Magnetic characterization

The magnetic profile of the sample was mapped together with its topography using the MFM mode described in section 2.1.3.7.2. For magnetic imaging, the tip-sample separation was kept constant at 120 nm during the scan and the MFM probe magnetized up to 1500 Oe at 10 K.

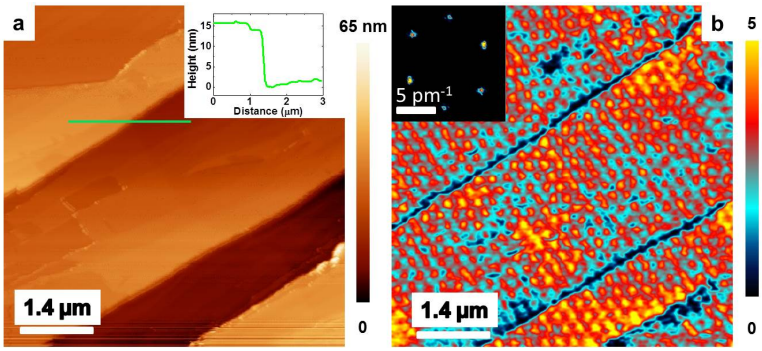

Figure 4.11: In a, we show a topographic image, with a line cut in the inset. Note that the height of the observed steps is of about 10 nm. In b, we show a vortex lattice image taken with MFM at 2K and 300 Oe in the same area, together with its Fourier transform (inset). The lattice is hexagonal over the whole area. The diagonal blue lines in the magnetic image are features due to cross-talk between topography and magnetic signals.

Fig.4.11 shows simultaneous topographic and magnetic images acquired at 2 K and 300 Oe after field cooling (FC). The topography shows terraces separated by steps of $\approx 10nm$, produced during the cleaving of the sample. In the simultaneous

magnetic signal a vortex lattice is observed over the complete scanned area. We observe a hexagonal vortex lattice over the whole image. Dark blue contrast is also seen in the magnetic images at the position of the topographic steps due to cross-talk between topography and magnetic measurements at the steps [124, 179].

4.2.2.1 Evolution of the vortex lattice with the applied magnetic field

We report here too of measurements made elsewhere, using a SQUID on a tip (SOT) set-up described in [180] and our MFM measurements. SOT measurements were done always in FC conditions by Dr. Yonathan Anahory and Dr Lior Embon in the group of Prof. Eli Zeldov at the *Weizmann Institute* in Israel with a tip-sample separation of several microns.

The measurements at very low magnetic fields using SOT and at higher fields with MFM provide a radically different behaviour. The vortex lattice is disordered at the lowest fields and becomes gradually more ordered, reaching the hexagonal arrangement for fields close to 100 Oe. Above this field, vortices always arrange in a hexagonal lattice. Selected SOT and MFM images are shown in Figure 4.12. From visual inspection it is clear that, at the lower fields, the vortices are randomly arranged. Upon increasing the field, the flux line lattice becomes gradually more ordered in a hexagonal arrangement, expected for Abrikosov flux line lattice as is clearly seen in the images above 100 Oe.

To quantitatively describe the vortex distribution, Delaunay triangulation was performed for all SOT and MFM images. In the SOT images, along the defects, above H $\approx$ 10 Oe, we do not fully resolve isolated vortices. We have used the small peaks observed in the local magnetic field profile to identify vortex positions. To independently verify that the count is right, we have integrated the magnetic field in the SOT images along the defects and verified that the resulting flux coincides with expected value from the number of vortices we use in the triangulation. A few images are shown in Fig. 4.13 as an example, together with a Delaunay triangulation scheme.

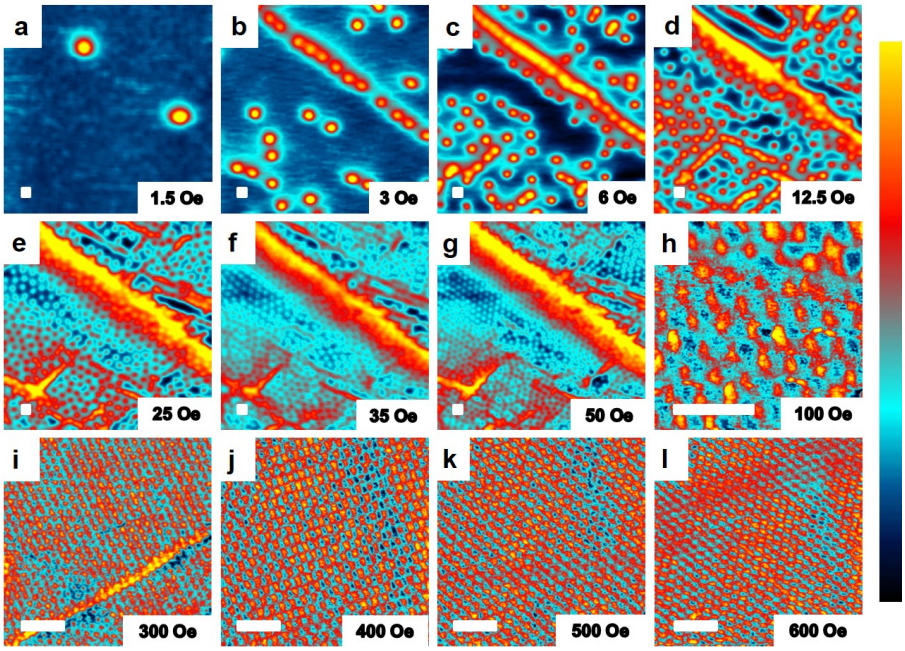

Figure 4.12: Evolution of the vortex distribution in $\beta - Bi_2Pd$ with the applied magnetic field. Images a-g were taken with SOT and present a disordered distribution at the lowest field that becomes more orderer at higher fields, vortex accumulation in clusters and linear features are observed. Images from h-l were taken with MFM. A regular Abrikosov lattice is clearly shown in all images. The lattice becomes denser as the magnetic field increases, as expected. The color scale represents the out-of-plane field, with span of 2 in a, 3.5 in b-c, 8.4 in d, 7.2 in e and 7.0 in f-g Oe in the SOT images and of 2 Degrees in the MFM images, h-l. The white scale bar represents 1μm.

With a Delaunay triangulation, we identify, measuring the distances between close-by vortices, the nearest neighbors of each vortex. These can be six, as in a hexagonal lattice, or more or less, when the lattice is disordered. Using the Delaunay triangulation, we can find the intervortex distances over the whole image and identify positions with defects in the vortex lattice, as positions with a number of nearest neighbors different from six.

The results of the triangulation are presented in in figure 4.14. The colour map corresponds to the distribution of intervortex distances extracted from the Delaunay triangulation. For fields below ~ 100 Oe, the histogram broadens and the distances between vortices become widespread. At very low magnetic fields we can observe intervortex distances ranging between half and twice the expected intervortex distance

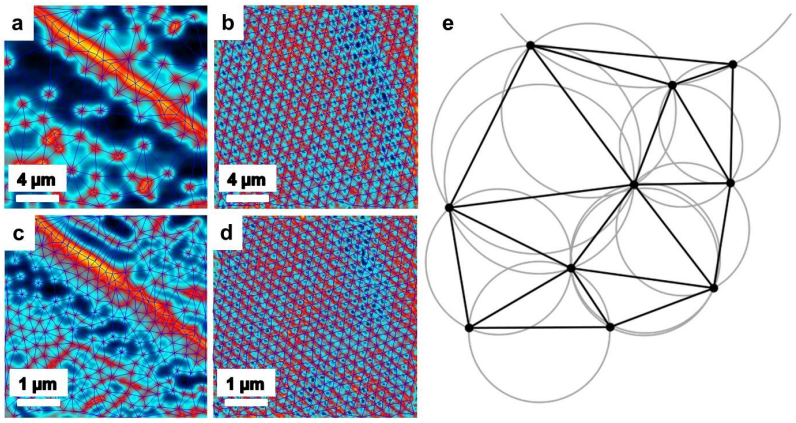

Figure 4.13: Examples of Delaunay triangulated images. Images at the left column were taken with scanning SQUID at low fields (5 Oe and 12.5 Oe) and images in the right column were taken with MFM (300 and 400 Oe). In e, an example of the Delaunay triangulation method. Black dots represents the vortex positions and and black straight lines the intervortex distances, black circles are the circumcircle corresponding to each triangle formed be three vortices.

for a hexagonal lattice ($d = (\frac{4}{3})^{1/4}\sqrt{\frac{\phi_0}{B}}$). Image inspection shows the strong spread in distances is due to location of vortices at lines, with the formation of vortex chains. This accumulation leaves vortex-free areas in between. Interestingly, the histogram is peaked at the expected intervortex distance d, although it is skewed at large distances, reflecting that pinning is limited by intervortex repulsion. It is important to note that the vortices arrange in a hexagonal lattice well below the H_{C1} of the sample, 225 Oe [25].

4.2.2.2 Penetration depth at defects

Vortices located at defects give weaker spots in the SOT images. The value of the magnetic field at the vortex centre is smaller than the value we find for vortices located far from the defect. This is nicely visible at lower fields when vortices are well separated and do not overlap, (see figure 4.15 b), where the vortices arranged in a chain like structure, present weaker spots that the ones far from the chain. There are a few vortices in the SOT images that are not arranged along the main line and also show weaker spots, for example the one marked by an yellow arrow in figure 4.15 c. At higher magnetic fields, vortices cluster along lines close to these positions are

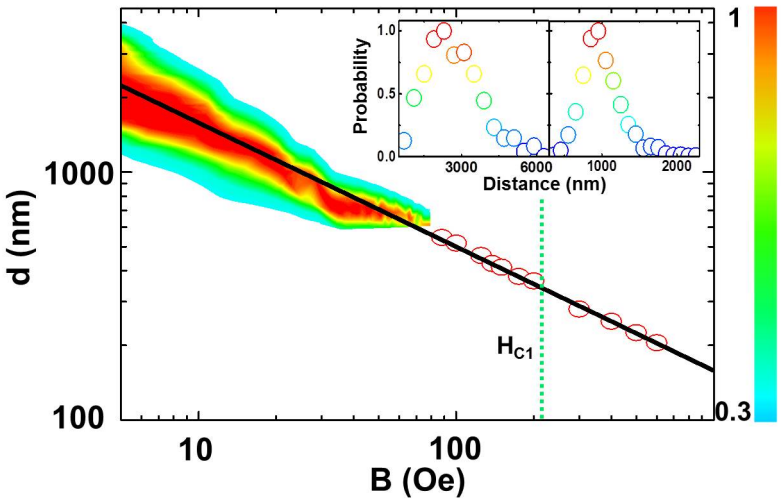

Figure 4.14: Intervortex distances vs the applied magnetic field. The black line represents the expected intervortex distance ($d(nm) = (\frac{4}{3})^{1/4}\sqrt{\frac{\phi_0}{B}}$), the red circles the measured intervortex distances with the MFM and the colour map the distribution of probabilities of intervortex distances obtained with the triangulation of the SOT images. Two different regimes are found, one at fields below $H_{C1} \approx 100$ Oe, where the vortex distribution is widespread and other above $H_{C1} \approx 100$ Oe, where the vortices are ordered forming the Abrikosov lattice. The lower critical field measured in [25] is represented by the green doted line. Colour scale is as represented by the bar at the right. In the insets, the histograms obtained for 3 and 25 Oe.

found (figure 4.15 d). These vortices are thus also located close to a defect.

In the inset of Fig. 4.15 a we show magnetic field profiles along two vortices showing weak and bright spots respectively. The profile of the isolated vortex can be fitted to a monopole located at a distance $\lambda + d_{SOT}$ from the SOT where λ is the penetration depth and d_{SOT} is the distance from the tip to the sample surface. Since the value of lambda is known, $\lambda = 132 \pm 20$ nm [25], the value of d_{SOT} can be estimated for the brighter spot. This analysis was performed by Dr Anahory, who left the penetration depth as a free parameter to fit the profile of the weak spots and find $\lambda_D = 270 \pm 40$ nm which is about two times the value found elsewhere.

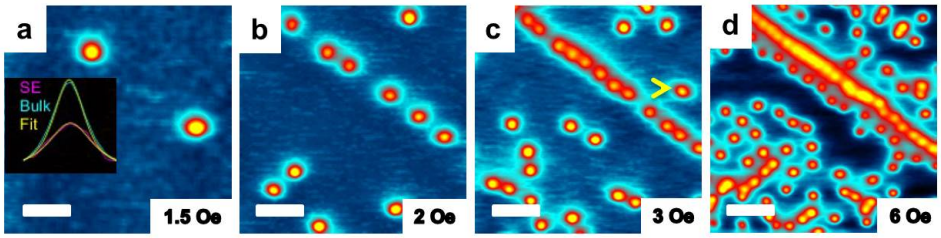

Figure 4.15: Selected images of SOT in $\beta - Bi_2Pd$. In a, two vortices on a defect. In b, c and d the evolution of the same area when increasing magnetic field. Vortices on the defects have weaker spots. In the inset the profiles of two vortices, one on the defect and another far from it together with the fitting described in the text. In c, the yellow arrow points a vortex far from the stripe which also shows a weaker spot. Visual inspection of d, shows that there is a vortex cluster at this position at higher fields, pointing out that there is also a defect at this position. 2 (a), 3.5 (b-d). The scale bar is white is 4μm

4.2.3 Origin of the variation in λ

As a possible origin for the observed behavior, let us consider strain close to defects. The dependence of λ and ξ with the strain produces an effective interaction between the crystal and the vortex lattices [181]. Also, the stress produced by flux pinning has been proposed as a source of magnetostriction effects in superconductors [182]. A recent theoretical work has demonstrated that strain can induce a square vortex lattice in the tetragonal superconductors [183]. The coupling between crystalline elasticity and the vortex lattice can be treated using the dependence of the critical temperature with the pressure dT_c/dP[181, 184–186]. Generally, vortices are repelled from locations where the internal strain is larger if $dT_c/dP > 0$ and are attracted to those locations if $dT_c/dP < 0$. The value of dT_c/dP in $\beta - Bi_2Pd$ is unknown and therefore we can not unambiguously prove that the vortex accumulation at the defects in our crystals are due to strain effects, but it is known that the non-centrosymmetric α-Bi_2Pd crystallizes at 3.8 K, 1.2K below the β-Bi_2Pd. At low magnetic fields, we find that vortices are accumulated along defects, which is compatible with $dT_c/dP < 0$. This is confirmed in a recent study of T_C vs pressure [187]

4.2.4 Origin of the flux landscape

All our experiments are in field cooled conditions, so we quench, during cooling, vortices at locations where the free energy landscape is more favourable [153–155, 162]. For the lowest magnetic fields, we find strong gradients in the vortex distribution. To analyse this further, we calculate the elastic energy associated to pairs of vortices, F, at different locations in our images. We compare the result for vortices located at a defect and giving weak spots in SOT images, with the elastic energy for pairs of vortices far from the defects. To this end, we use $F = \frac{\phi_0^2}{4\pi\mu_0\lambda^2} log(\kappa) + \frac{\phi_0^2}{4\pi\mu_0\lambda^2} K_0(d/\lambda)$ for the free energy per unit length of two vortices interacting with each other at a distance d [28]. The first term comes from the energy of superfluid currents, giving the line tension of the vortex, and the second term represents the interaction energy between vortices. K_0 is the modified Bessel function of the second kind. We then calculate F for vortices far from defects using the bulk λ and for vortices at the defects, using λ_D provided above. Below $\approx 50Oe$ the intervortex distances vary from 0.5 to 4 μm and the second term of the interaction energy remains negligible with respect to the first term, giving a difference in free energy between both situations of $\Delta F \approx 2 \times 10^{-11} J/m^3$ independent of the intervortex distance.

We can now compare ΔF with the pinning energy of a vortex pinned at a normal inclusion in β-Bi_2Pd using $U_{core} = \frac{B_c^2 \pi \xi^2}{\mu_0}$ [188], with B_c the thermodynamic critical field and ξ the superconducting coherence length ($\xi \approx 25$ nm, [23, 189]). We find a value which is smaller than ΔF, $1 \times 10^{-11} Jm^{-1}$. Thus, single vortex pinning at defects play an unimportant role in the vortex distribution on $\beta - Bi_2Pd$. Moreover, it is difficult to think of normal inclusions as large as $\xi \approx 25$ nm to pin isolated vortices. Thus, pinning seems to play a minor role in β-Bi_2Pd at low fields. The accumulation of vortices at the defects can be explained with the lower free energy caused by the experimentally determined changes in λ.

It is quite remarkable that such a simple estimation provides such clear results, and are probably particularly valid when vortices are very far apart, at the lowest magnetic fields we have studied. For higher magnetic fields, the vortex lattice density increases and the previous two-vortex interaction approximation is no

longer valid. For fields above ≈ 50 Oe we have considered the free energy of a vortex, interacting with its first six neighbours arranged in a hexagonal lattice using: $F = n\frac{\phi_0^2}{4\pi\mu_0\lambda^2}log(\kappa) + 3n\frac{\phi_0^2}{4\pi\mu_0\lambda^2}K_0(a/\lambda)$ [28], where a is the lattice parameter of the Abrikosov lattice determined by $a = (\frac{4}{3})^{1/4}\left(\frac{\Phi_0}{B}\right)^{1/2}$ and n the number of vortices per unit area. The difference of energy between six vortices close to a defect with λ_D and six vortices far from the defect with λ changes with the intervortex distance. We find that when vortices at the defect are closer than about 400 nm, it is no longer energetically favourable to add new vortices to the defect. This can explain the vortex distribution at low fields shown in Fig. 4.14. We find that the cross-over field is of ≈ 200 Oe. In the experiment, we find that already at $\approx 100Oe$ the distance histogram closes and the vortex lattice becomes hexagonal. We believe that, given the crude approximations made, the agreement is remarkable and provides a simple but useful explanation to the vortex landscape at low fields.

It is also noteworthy that the average value of the intervortex distances follows d for all magnetic fields. This finding has not been previously reported, to our knowledge, at low magnetic fields and in presence of strongly inhomogeneous vortex distributions. Instead the usual pictures consist of clusters of vortices with widely differing intervortex distances that are often smaller than d.

The vortex patterns that we have measured in β-Bi_2Pd showed both behaviours. At very low fields, there are strong gradients in the vortex distribution. No stripes or clusters as in MgB2 with two well defined intervortex distances, but nevertheless strong vortex accumulation. At higher magnetic fields, still below H_{c1}, we observe in contrast a hexagonal, defect free, vortex lattice.

β-Bi_2Pd is clearly a single gap superconductor, so vortex clustering cannot be associated to multiple gap opening here [23, 25]. Thus, the vortex patterns at very low fields in $\beta - Bi_2Pd$ are due to the distortion of the hexagonal lattice formed during the FC process by pinning at crystalline defects due to differences in the values of the penetration depth. At very low fields, the vortex-vortex repulsion potential is small, and pinning dominates, leading to the observed vortex clustering. At higher fields, the vortex-vortex repulsion potential impedes pinning of isolated vortices and the vortex lattice arranges as a whole in a regular hexagonal lattice.

It would be interesting to consider this scenario within the very recent proposal for a small p-wave component appearing in the order parameter close to the surface [178]. Particularly close to defects, we can think of modifications in the surface properties that could enhance such effects.

4.2.4.1 Evolution of the vortex lattice with the temperature

The penetration depth is expected to increase as the temperature approaches T_C, therefore, the superconducting vortex profile will be broader as the temperature increases. Eventually, at T_c, the magnetic profile will become homogeneous over the whole surface of the superconductor [28, 190].

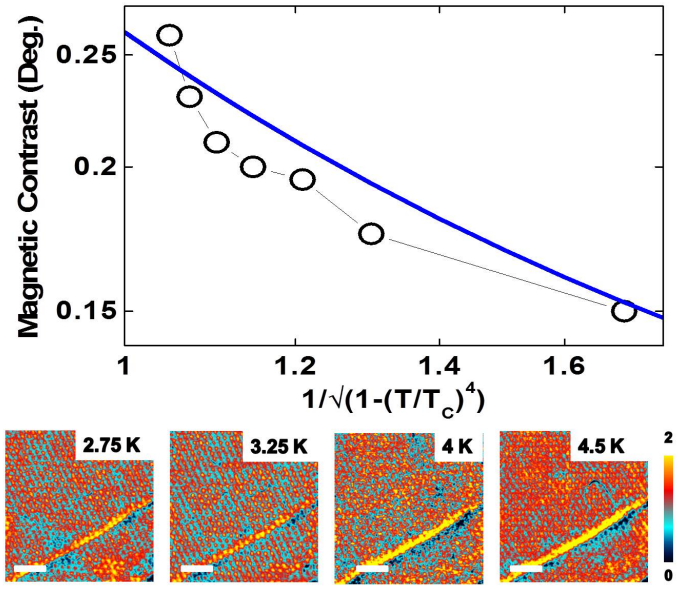

Figure 4.16: Evolution of the vortex lattice with the temperature. In the upper panel, a plot of the evolution of the magnetic contrast with the temperature is shown. The experimental data (black circles) was obtained from MFM images measured under a perpendicular magnetic field of 300 Oe at the same area. The blue line represents the expected magnetic contrast due to the theoretical evolution of λ as explained in the text. Both curves have the same behavior, proving that the evolution of the vortex width is dominated by the evolution of λ. In the lower panel, four of the MFM images used to obtain the plot. Scale bar in white is 1μm.

We have measured the magnetic profile of the same area at different temperatures

and constant magnetic field. After cooling down the sample to 2.75 K in a perpendicular magnetic field of 300 Oe, the temperature was increased to 3, 3.25, 3.5, 4, 4.5 and 5 K recording the magnetic profile at each temperature. The evolution of the vortex profile width with the temperature is presented in figure 4.16. Experimental data was obtained as the difference between the MFM signal at the centre of the vortices and the background between vortices. The magnetic field profile around vortices becomes broader as the temperature increases. This can be related to the increase in the penetration depth, $\lambda(T) = \frac{\lambda(T=0)}{1-(T/T_C)^4}$. In the image, the relation between the experimental data and the expected evolution of the penetration depth is clear. We have calculated the expected value of the contrast as the difference of the magnetic field at the centre of a vortex and in between its neighbours in an hexagonal lattice using equation 2.14. At 5 K, no vortex lattice was found in the sample, in agreement with the resistive T_C [23].

4.2.4.2 Orientation of the vortex lattice

Previous works in the same $\beta - Bi_2Pd$ crystals have found that at high fields, the hexagonal vortex lattice is oriented with one of its axis along a crystallographic direction [23]. AFM has no atomic resolution and therefore, it can not determine the directions of the crystals lattice, but they can be inferred from the direction of the atomic steps that are easily measured with an AFM.

Here, we have found that at low magnetic fields, below $\approx$ 200Oe, the vortex lattice is preferentially oriented with one axis following the steps direction. At higher magnetic fields, when the distances are practically homogeneous over the whole field of view, the vortex lattice is oriented at 90° with respect to the defects (figure 4.17). And it suggests that the vortex accumulation around defects found at the lowest fields does not occur exactly at the pinning centers (which would favor that one of the main axis of the hexagonal vortex lattice is oriented with the defect), but is a result of a collective interaction between vortex and crystal lattices.

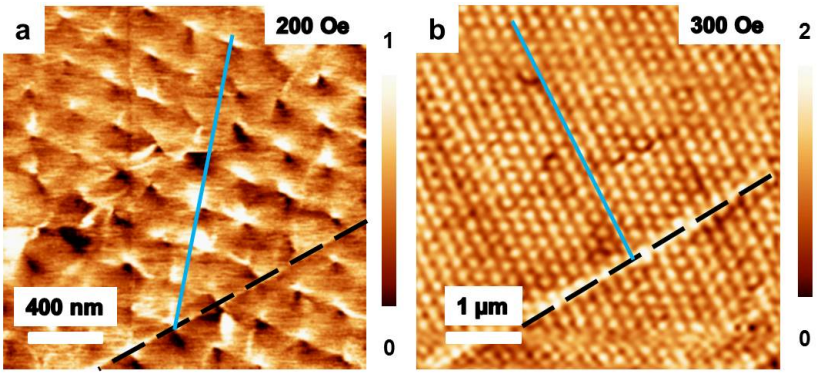

Figure 4.17: Example of the two vortex lattice orientations found. In a, the vortex lattice at 200 Oe form $\approx 30°$ with respect to the topographic step (dashed black line in the image). In b, at 300 Oe, one of the main directions of the vortex lattice is normal to the topographic step. In both images the direction of the vortex lattice is highlighted with a light blue line.

4.3 Electrochemical transfer of graphene on β-Bi_2Pd

We have transfered a graphene sheet of $\approx$ 1 cm $\times$ 1 cm area on a β-Bi_2Pd substrate using a PMMA as a wetting layer. The graphene sheet was grown in high vacuum on a copper foil by Jon Azpeitia at the laboratory of Prof. Jose Martin Gago (for a detailed description of the graphene growth see references [192] and [193]).

To transfer the graphene sheet from the copper foil to the β-Bi_2Pd substrate we have used the common electrochemical transfer method described in [194, 195]. In this method, first, the graphene is covered by a PMMA layer via spin coating (figure 4.18 a). Then, the coper foil with the graphene and the PMMA is immersed in a solution of potassium chloride at a rate of 1 mm/s (figures 4.18 b and 4.19 a). The copper is negatively polarized up to 5 V with respect to a carbon anode. When the graphene/copper cathode is negatively polarized, hydrogen bubbles appear at the graphene/copper interface due to the reduction of water molecules and allow graphene to gently detach (figure 4.18 c). Then, the graphene/PMMA layer is placed on top of the substrate (figures 4.18 d and 4.19 c) and the PMMA layer is dissolved with acetone to obtain free graphene deposit on top of the substrate (figure 4.18 e and f).

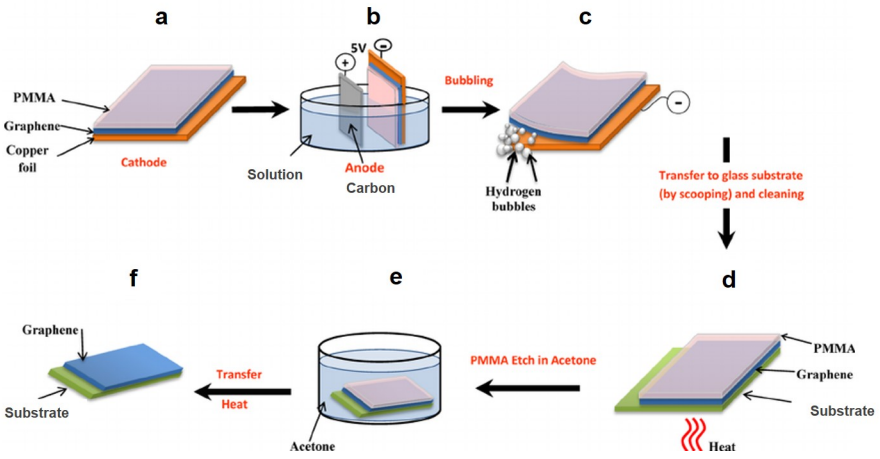

Figure 4.18: Schematic representation of the graphene sheet transfer method. The PMMA layer is presented in light pink, the graphene in blue, the copper foil in orange and the substrate in green. First, the graphene is covered by a PMMA layer via spin coating (a). Then, the copper foil with the graphene and the PMMA are immersed in a solution of potassium chloride at a rate of 1 mm/s (b). The copper is negatively polarized with respect to a carbon anode. When the cathode is negatively polarized, hydrogen bubbles appear at the graphene/copper interface due to the reduction of water molecules and allows graphene to gently detach (c). Then, the graphene/PMMA layer is placed on top of the substrate (d) and the PMMA layer is dissolved with acetone and heated up to 70 ° to obtain free graphene deposited on top of the substrate (e and f) Adapted from [191].

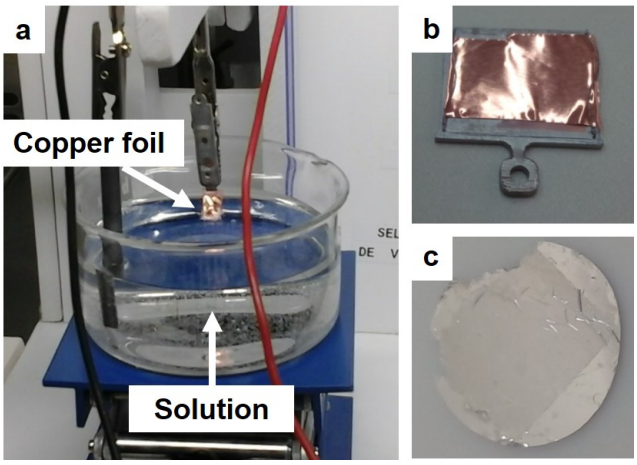

Figure 4.19: In a, the experimental set-up to transfer the PMMA/graphene layer to an arbitrary substrate. In b, a photography of the copper foil with the graphene deposited on top. In c, a photography of the β-Bi_2Pd crystal with the graphene/PMMA layer deposited on top.

4.3.1 Characterization at room temperature

After transfering the graphene on the β-Bi_2Pd crystal, we have characterized it in our RT-AFM to ensure the success of the transfer. We have found that the whole surface of the crystal was covered by remains of the PMMA layer, showing a very irregular and dirty surface (figure 4.20).

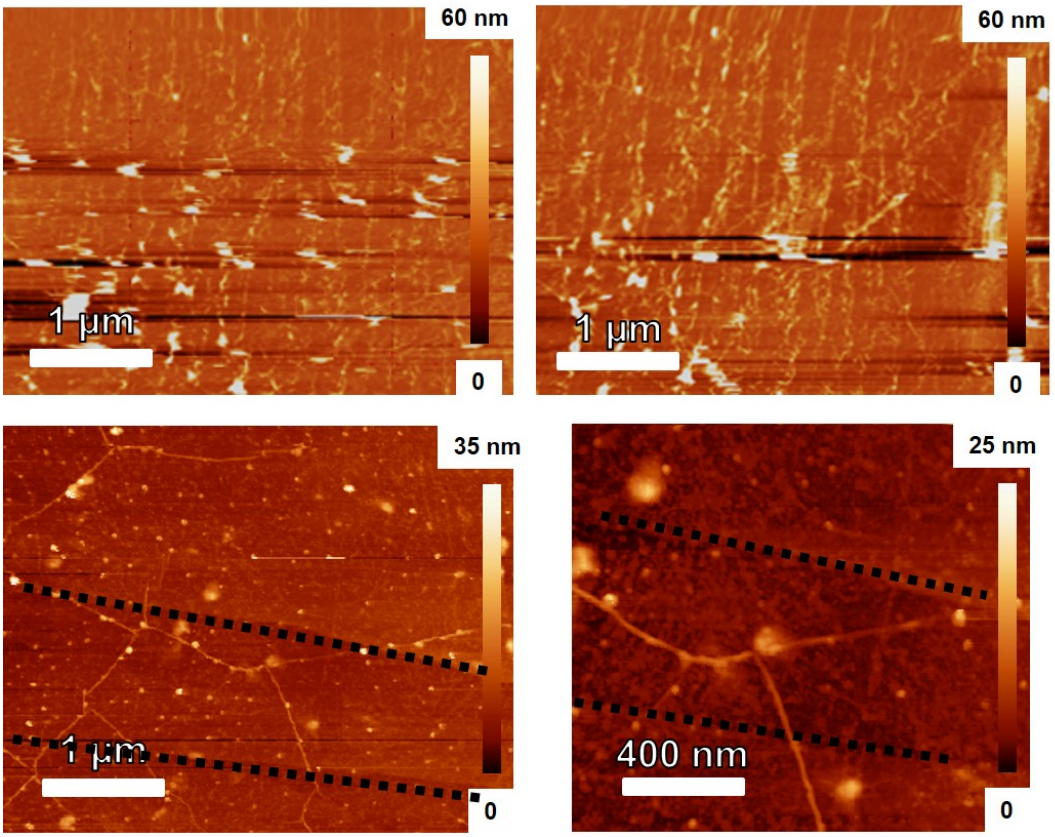

Figure 4.20: In the figure, we show four topographic images measured at RT with our RT-AFM in a sample with graphene deposited on top of a β-Bi_2Pd crystal. In the upper panel, two topographic images measured while cleaning the sample with the AFM tip in the contact mode. In the lower panel, the same sample after clean it with the tip. In both images the characteristic wrinkles (light lines) of the graphene, pointing the success of the transfer. The steps of the β-Bi_2Pd crystal are signaled as black dotted lines.

To clean the sample we have scratched the surface with the AFM tip in contact mode several times until the remains of the PMMA layer were removed from the surface. Then, we have measured the area again, finding the characteristic wrinkles

of graphene in the whole field of view of the image (figure 4.20). There are also visible some surface contaminations that remains at the surface after cleaning the system with the tip. This measurements point the big success of the transfer.

4.3.2 Characterization at low temperatures

We have measured the same sample at low temperatures. Figure 4.21 shows the topographic image of the sample at 2 K before and after cleaning it with the AFM tip. We were able to clean the surface without damaging the graphene layer or the MFM tip. Figure 4.21 reveals the characteristic wrinkles of the graphene layers and some steps and terraces of the β-Bi_2Pd crystal, showing the success of our cleaning method at low temperatures.

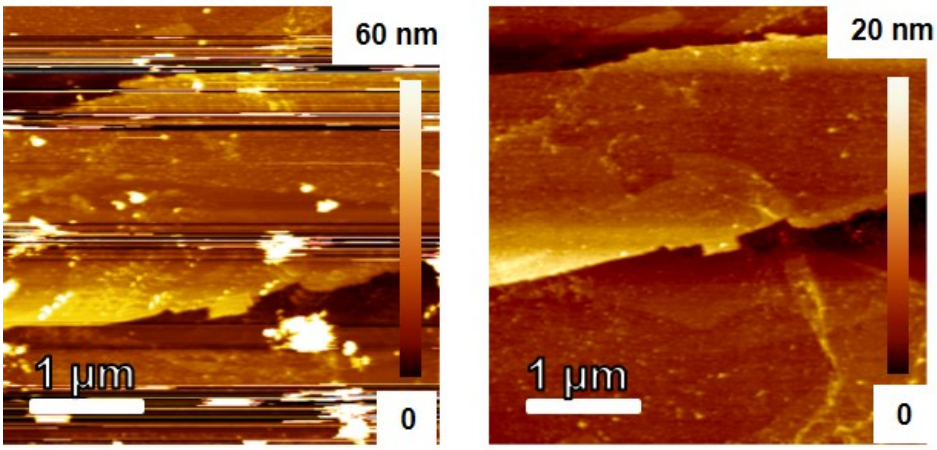

Figure 4.21: In the figure, we show two topographic images measured at 2K with our LT-AFM in a sample with graphene deposited on top of a β-Bi_2Pd single crystal. In the left panel, the area before cleaning it with the tip and in the right panel after cleaning it. In this image are visible the characteristic wrinkles of the graphene pointing the success of the transfer and cleaning methods.

After cleaning the surface, we have measured the magnetic field on the surface of the sample. Figure 4.22 shows the topographic and magnetic images measured at the same area at 2 K and under an applied magnetic field of 300 Oe in the out of plane direction. The magnetic image shows a hexagonal vortex lattice in the whole field of view, revealing that it is possible to observe the vortex lattice through the graphene layer. From the image, we have not found any visible distortion of the hexagonal

lattice with respect to the samples without graphene.

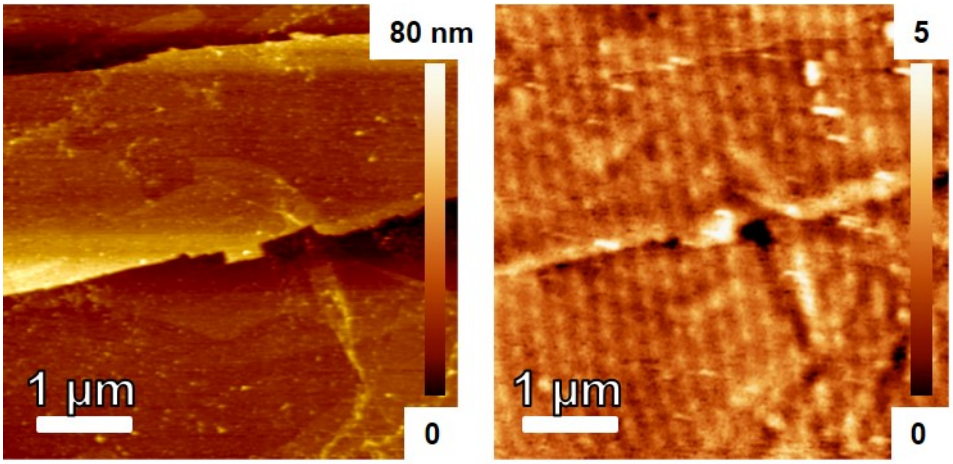

Figure 4.22: Topographic and magnetic images of the transfered graphene layer on top of the β-Bi_2Pd crystal measured at the same area at 2 K under an applied magnetic field of 300 Oe perpendicular to the surface. On the left, the topographic image reveal the characteristic wrinkles of the graphene sheet an the steps and terraces of the β-Bi_2Pd crystal. On the right, the magnetic image shows the ordered hexagonal vortex lattice.

To see if the graphene modifies the superconducting penetration depth, we have compared magnetic profiles with and without graphene on the surface. In essence, we find no remarkable difference. However, when we do the same analysis for vortices pinned around step edges, we do find a difference.

To see this difference, let us analyze the average over the radial profile of 30 vortices in each case. This is shown in Fig. 4.23 The fit to a Gaussian function provides no measurable difference.

When we compare magnetic profiles of vortices at the steps, we find a different result. In Fig. 4.24 we show the radial average of 10 vortices located at a defect with and without graphene coverage.

As it was presented in previous sections, the increment of the penetration depth at the topographic defects in the case of the pristine β-Bi_2Pd single crystal was also characterized in the Weizmann Institute of Israel by Dr. Anahory and Dr. Embon using a crystal from the same growth. Their results points that there is an increment

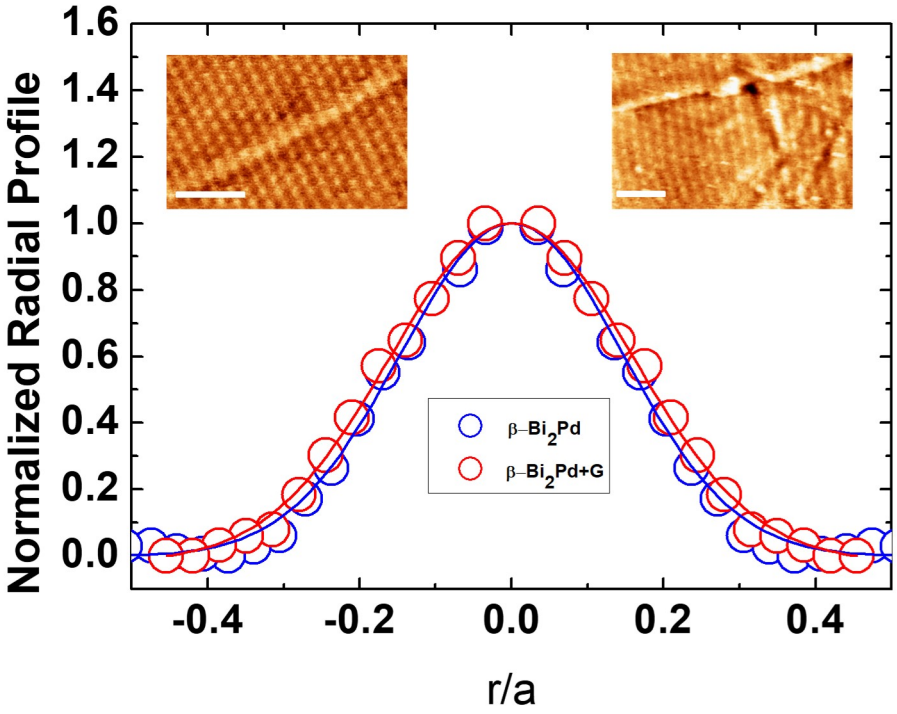

Figure 4.23: In the figure, we show the average of the normalized radial profiles for vortices far from the defects measured on a β-Bi_2P single crystal with and without a graphene layer deposited on top. The horizontal axis represents the radial distance from the center of the vortex divided by the Abrikoshov lattice parameter (a). The lines in the plot represent the Gaussian fit of the experimental data. Both fits show identical behavior with only differences of a few nanometers, well bellow the MFM resolution. In the figure, the magnetic images measured on the β-Bi_2P single crystal (left inset) and on the β-Bi_2Pd single crystal with the graphene layer deposited on top (right inset) are also shown. In the images the topographic defects are clearly identified as bright diagonal stripes from left to right and from bottom to top. Both scalebars represents 1 μm.

of the penetration depth at the defects. In the case of the sample with graphene, the profiles are even broader that in the β-Bi_2Pd single crystal. The Full width at half maximum (FWHM) of the Gaussian fit of the vortices at the defects in the case of the β-Bi_2Pd single crystal without graphene is 1.3 times higher than the FWHM for the Gaussian fit of vortices far from the defects. But, in the case of the sample with graphene on top, the FWHM at the defects is twice than the FWHM far from the defects. This, points that graphene modifies the local screening properties at the

defects of the β-Bi_2Pd single crystal and produces and enhancement of the penetration depth at these positions.

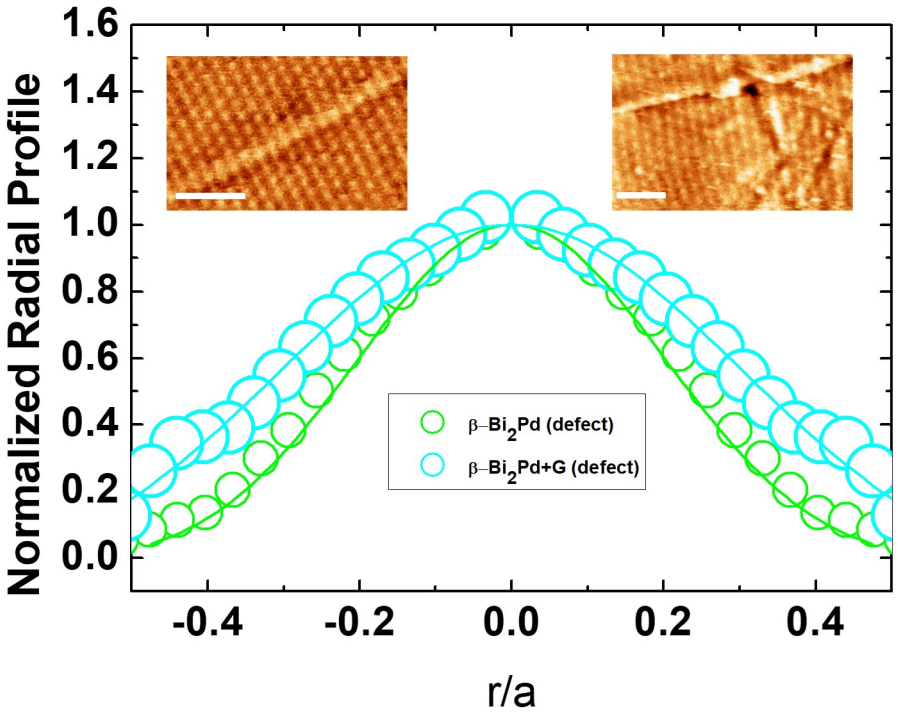

Figure 4.24: In the figure, we show the average of the normalized radial profiles for vortices at the defects measured on a β-Bi_2P single crystal with and without a graphene layer deposited on top. The horizontal axis represents the radial distance from the center of the vortex divided by the Abrikoshov lattice parameter (a). The lines in the plot represent the Gaussian fit of the experimental data. In the figure, the magnetic images measured on the β-Bi_2P single crystal (left inset) and on the β-Bi_2Pd single crystal with the graphene layer deposited on top (right inset) are also shown. In the images the topographic defects are clearly identified as bright diagonal stripes from left to right and from bottom to top. Both scalebars represents 1 μm.

Thus, graphene does not modify the magnetic flux out of the superconductor when there are no defects. As in the tunneling experiments shown in Ref. [102] in Re, graphene is strongly coupled to the substrate and essentially it is transparent, and remains superconducting, for all practical purposes.

At the defects, however, there is a clear increase in the penetration depth produced

by the graphene layer. This effect can be explained by an increase in the distance between graphene and the surface at the step edges. This decreases the barrier Γ, providing thus a reduction of the superconducting gap induced in graphene and therefore an increase in the penetration depth.

Several theoretical works have proposed different mechanism of superconductivity in graphene by placing it on a superconductor with a BCS or a non-BCS pairing symmetry [96, 97], depending on the position of the Fermi level with respect to the Dirac point. Experimentally, superconductivity in graphene was achieved by placing it in contact with the s-wave superconductor Re and the superconductor $Pr_{2-x}Ce_xCuO_4$ [2]. In the case of β-Bi_2Pd, a recent work, has proposed the existence of topological p-wave superconductivity at the surface [178] in addition of the previously reported s-wave behavior at the bulk [24, 25].

4.4 Summary and conclusions

In conclusion, we have observed two different regimes in the patterns of pinned superconducting vortices at low magnetic fields in the single gap superconductor β-Bi_2Pd. We have shown that lines of vortices form at defects due to pinning at very low magnetic fields, while at higher fields the vortex lattice acts as a whole, showing a regular hexagonal lattice even below H_{c1}. Crystalline strain close to defects determines the vortex arrangements at low fields and leads to sizable modifications of the local superconducting screening properties. The mutual influence of crystalline strain and the vortex lattice has been extensively studied at high magnetic fields. Here, we show that this mutual influence also modifies vortex arrangements at very low magnetic fields. At fields slightly above H_{C1}, where vortices are arranged in a regular Abrikosov lattice, we have found that the magnetic profile of the vortices follow the expected behaviour when changing the temperature. We have not found any evidence of vortex clustering when decreasing the temperature as in other superconducting materials. Instead, there is a widespread distribution of intervortex distances.

Finally, we have transfered a $\approx$ 1 cm $\times$ 1 cm graphene sheet on top of a β-Bi_2Pd

single crystal with the electrochemical transfer method and measured the vortex lattice of the β-Bi_2Pd crystal at the superconducting state at 2K trough the graphene layer. We have not found any difference between the magnetic profile of vortices far from the topographic defects in the β-Bi_2Pd crystal between the sample with and without graphene on top. We have found that in the case of the sample with graphene on top, vortices become much broader at the position of the topographic defects in the β-Bi_2Pd crystal than in the case of vortices in the sample without graphene. This experiment demonstrates that graphene is essentially transparent for the magnetic properties of superconductivity, unless the interaction between sample and substrate is modified. When the interaction is weaker, we observe that the penetration depth increases, opening the path to interesting experiments addressing unconventional superconducting properties.

CHAPTER 5

Strain induced magneto-structural and superconducting transitions in $Ca(Fe_{0.965}Co_{0.35})_2As_2$

Tuning parameters are a essential tool in the study of materials, since they can be used to control the appearance of an specific behavior. As an example, unconventional superconductivity often emerges around the point where antiferromagnetic order is suppressed by hydrostatic pressure [196]. Strain has been occasionally used as a tuning parameter [197–200], but is less employed than pressure. Strain has been mostly employed to probe the nematic susceptibility of iron-based superconductors [201–204].

Iron-based superconductors have a rich interplay between antiferromagnetism, orthorhombic to tetragonal distortion and superconductivity. Numerous tuning parameters have been used in iron-based superconductors, including: chemical substitution [205], hydrostatic pressure [206, 207], epitaxial strains in thin films [208, 209], uniaxial strain in $CaFe_2As_2$ and $BaFe_2As_2$ [210–215] and biaxial pressure in $Ca(Fe_{1-x}Co_x)_2As_2$ [71].

5.1 Previous studies in the parent compound $CaFe_2As_2$

The parent compound, $CaFe_2As_2$, presents tetragonal structure together with paramagnetism at ambient conditions and transits to either an antiferromagnetic/orthorhombic (AFM/ORTH) phase or a paramagnetic/collapsed tetragonal (PM/CT) phase when decreasing the temperature, depending on the hydrostatic pressure [216]. The AFM/ORTH transition is also present on other compounds of the same family like $BaFe_2As_2$, but $CaFe_2As_2$ is extremely sensitive to the pressure. For example it transits from orthorhombic to a collapsed tetragonal phase under 0.35 GPa at 33 K [216], which is a much more moderated pressure than $BaFe_2As_2$ (29 GPa [217]).

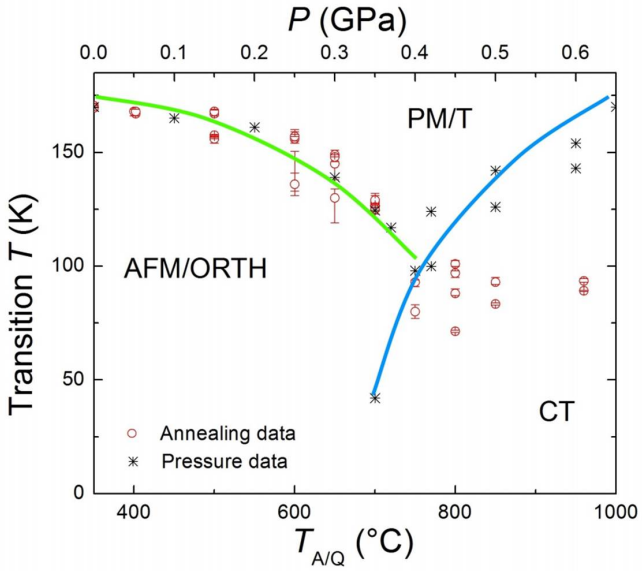

Figure 5.1: Phase diagram of $CaFe_2As_2$ as a function of the post growth annealing temperature and the hydrostatic pressure. In the lower x-axis, the annealing temperature and in the upper x-axis, the hydrostatic pressure. Black asterisks are the pressure data measured in [216] and red circles are the data obtained from the annealing treatment in [218]. Green and blue lines are a guide to the eye. Adapted from [219].

The possibility of stabilizing the PM/CT ground state at ambient pressure was also proved in [218] using a post growth annealing treatment. They argued that the changes in the internal strains due to the formation of FeAs nanoparticles in the sample are the cause of the change in the ground state as a function of the annealing temperature. Changing the annealing temperature will modify the size of the FeAs

precipitates and therefore the internal strain. The combination of the phase diagrams obtained in [216] and [218] is shown in figure 5.1. Authors establish, through this work, a relationship between pressure and annealing temperature that is quite useful to access some parts of the phase diagram using techniques where no pressure can be applied.

5.1.1 Structural domains at low temperatures

Studies of polarized light microscopy have shown the formation of structural domains below the tetragonal to orthorhombic transition in AFe_2As_2, A= Ca, Sr, Ba [220]. The authors of this work associate the contrast of the optical images to the rotation of the polarization plane between neighbouring domains in twin boundaries of orthorhombic domains.

In figure 5.2 we show an optical image of a $CaFe_2As_2$ single crystal at 5 K, well below the tetragonal to orthorhombic transition. A regular pattern of domain boundaries oriented in two orthogonal directions is clearly visible. A typical domain width is about 10 μm. Over large areas, sometimes covering the whole surface of the crystal, domains form stacks of parallel plates. In some areas perpendicular domain sets interpenetrate. The crystal under study has terraces on the sample surface and shown in inset at RT, with a step size of the order of 20 μm. On crossing the terraces, the domain lines perfectly match at different levels. This clearly shows that the domain walls are extended along the c axis.

5.2 Previous studies in $Ca(Fe_{1-x}Co_x)_2As_2$

A different approach was made by authors in [221]: they combined the effect of cobalt substitution and post growth annealing to characterize the 3D phase diagram of $Ca(Fe_{1-x}Co_x)_2As_2$ as a function of these two tuning parameters. In $Ca(Fe_{1-x}Co_x)_2As_2$, substitution of Fe for Co suppresses a coupled of first-order magnetostructural transition at $T_{s,N}$ and induces superconductivity with a maximum Tc of 16 K [221]. Authors in [221] proved that the ground state of $Ca(Fe_{1-x}Co_x)_2As_2$ can be tuned to

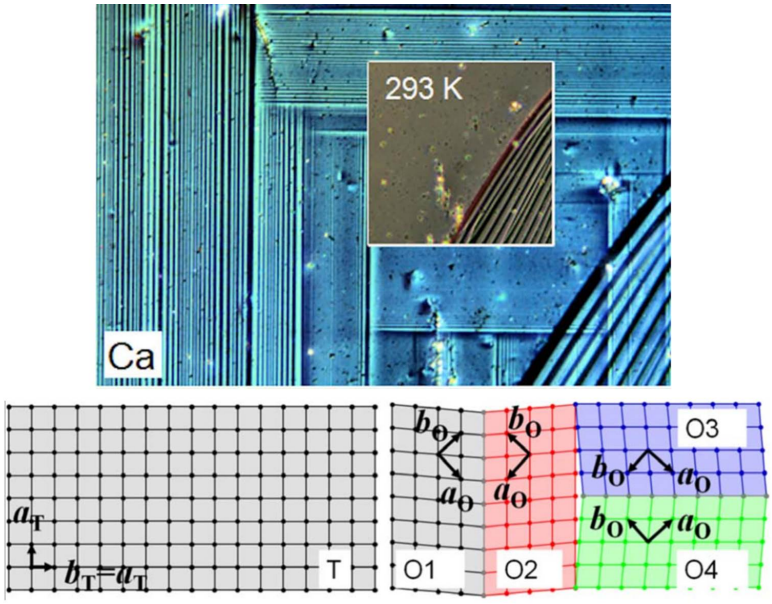

Figure 5.2: In the upper panel, a white light optical image measured in a polarization microscope showing a pattern of structural domains in $CaFe_2As_2$, at T≈ 5 K. The characteristic spacing between the lines is about 10 μm and the contrast in optical images follows the magnitude of orthorhombic distortion in the compound. The inset shows terraces on the crystal at room temperature at the same area. The c axis is perpendicular to the surface. In the lower panel, in the left, an scheme of the atomic positions in the tetragonal lattice. In the right, a scheme of the orthorhombic distortion and formation of domain walls at low temperatures. Different colours are used for different domains. Adapted form [220]

two new states, one superconducting, paramagnetic and tetragonal (SC/PM/T) state and another normal, paramagnetic and tetragonal (N/PM/T) state. The phase diagram obtained via resistivity, susceptibility and specific heat measurements is shown in figure 5.3. It is important to note that the studies from [221] were performed on free standing samples, only fixed using soft glues such as vacuum grease.

$Ca(Fe_{1-x}Co_x)_2As_2$ is also exceptionally pressure sensitive. Authors in [222] found a large rate of suppression of $T_{s,N}$ with hydrostatic pressure in the compound with x=0.028, $dT_{s,N}/dp \approx -1100$ K/GPa.

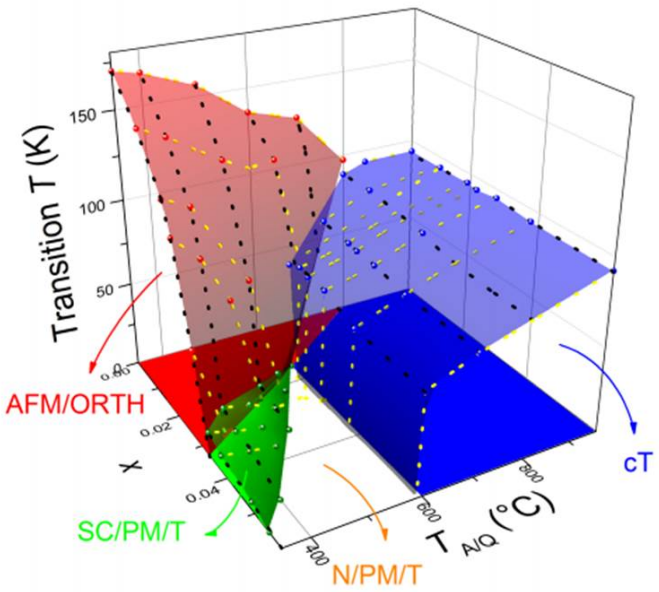

Figure 5.3: 3D phase diagram of $Ca(Fe_{1-x}Co_x)_2As_2$. x is the substitution level and $T_{A/Q}$ the annealing/quenching temperature. Four phases are observed, in red the antiferromagnetic/orthorhombic (AFM/ORTH), in green the superconducting/paramagnetic/tetragonal (SC/PM/T), in white the non superconducting/paramagnetic/tetragonal (N/PM/T) and in blue the collapsed tetragonal (CT) state. Adapted from [219].

5.2.1 Effect of biaxial strain

A recent work has focused in the effect of biaxial strain on the doped compound $Ca(Fe_{1-x}Co_x)_2As_2$ [71]. The authors have studied the effect of biaxial strain by making use of the different thermal expansion between the sample and a rigid substrate where the sample was glued. They measured a series of samples with different Co concentrations, first in free standing conditions and then glued to a rigid substrate. With a combination of high energy x-ray diffraction (XRD) and capacitance dilatometry techniques, they compared the evolution of the lattice parameters of both, free standing and glued samples, finding that the effect of biaxial strain induced by the difference between substrate and sample thermal expansion coefficients, modifies the sample state. The different expansion coefficients causes strain (ϵ) in the a-b plane of the sample affecting the c/a ratio. They found that samples that do not show AFM/ORTH transition when free standing, show a structural transition when glued to a substrate, proving that the c/a ratio is a suitable tuning parameter in

$Ca(Fe_{1-x}Co_x)_2As_2$ [71].

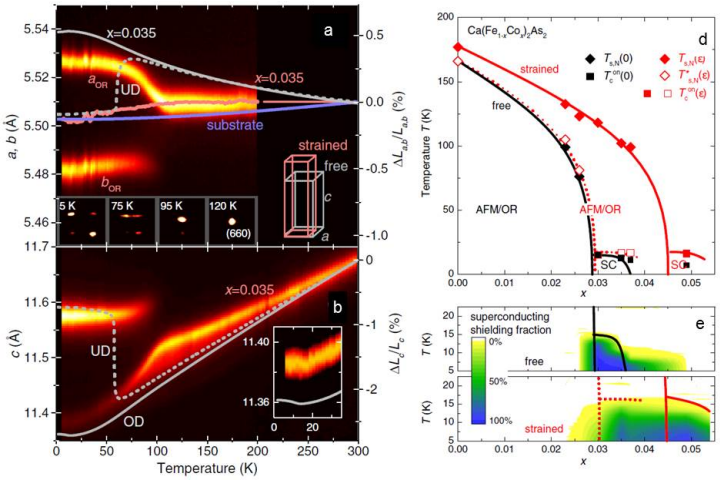

Figure 5.4: In the left panel, the in plane and c axis structural data for $Ca(Fe_{1-x}Co_x)_2As_2$ x=0.35 is presented. The colour code intensity maps represents the lattice parameters measured by x-rays diffraction when warming the sample. Lines indicate uniaxial fractional length changes, $\Delta L_i = Li$ (i=c, c axis and i=a, b, in-plane average), of free overdoped (OD samples, x=0.035 in a and x=0.029 in b) and of a representative underdoped (UD) x=0.027 sample obtained by capacitance dilatometry. The blue line shows the substrate thermal expansion and the red line indicates the average in-plane length of strained $Ca(Fe_{0.965}Co_{0.035})_2As_2$ inferred from the diffraction data. The right inset in a shows an scheme of the deformation of the unit cell due to the strain. The row of insets in a, show the diffraction pattern close to the tetragonal (660) reflection revealing orthorhombic domains. The inset in b presents the data on expanded scales. In the right panel, in c, the phase diagram of $Ca(Fe_{1-x}Co_x)_2As_2$ in the free (black) and strained (red) state. The AFM/ORTH transition at $T_{s,N}(\epsilon)$ is only gradual. Red open symbols and dashed lines correspond to the remaining phase fraction within the strained sample. In d,the superconducting shielding fraction of free and strained samples, respectively. Lines are a guide to the eye. Adapted from [71].

In the figure 5.4 a, the in plane and c axis structural data for samples with x=0.35 is presented in combination with the data for free standing samples obtained by capacitance dilatometry. The substrate thermal expansion is also shown. In figure 5.4 c, the phase diagram of $Ca(Fe_{1-x}Co_x)_2As_2$ in the free and strained state is presented. In the diagram is shown how the AFM/ORTH transition in the strained sample takes place at higher Co concentration than in the free standing samples. As

the temperature decreases, the c/a ratio is modified due to the strain on the sample, favouring the nucleation of orthorhombic domains in certain regions of the sample, splitting the samples in orthorhombic and tetragonal domains. In the under doped (UD) samples (x<0.28) the samples have a strain induced orthorhombic structural transition at a temperature above the structural/magnetic transition of free samples. Below this temperature the sample is split in tetragonal and orthorhombic domains and below a temperature close to the orthorhombic transition of free samples, the remaining tetragonal domains of the UD samples transit to the orthorhombic phase. For overdoped (OD) samples with cobalt concentrations between 0.28 and 0.49, the strain produces the coexistence of tetragonal and orthorhombic domains in the sample below $T_{s,N}(\epsilon)$ that persists until lower temperatures. For those samples, when the temperature is decreased below the T_C of free standing samples, the strained ones, presents a superconducting transition associated to the tetragonal domains. Above concentrations of 0.49, there is no structural transition associated with strain while the superconducting transition is still present below T_C.

5.3 AFM/MFM studies in $Ca(Fe_{0.965}Co_{0.35})_2As_2$

Previous works have studied the coexistence of tetragonal and orthorhombic domains in strained $Ca(Fe_{1-x}Co_x)_2As_2$ single crystals from a macroscopic point of view [71]. Prior to our work there was no microscopic evidence of the distribution of those domains or the geometry of their boundaries. Moreover, the interplay between tetragonal and orthorhombic domains in the superconducting phase remains unclear. This was our main motivation and the starting point of our study in this compound.

AFM/MFM measurements were performed in the set up of our lab described in section 2.1 in a $Ca(Fe_{1-x}Co_x)_2As_2$ single crystal doped with a 3.5% of Co and annealed at 350°. The crystal was grown by the group of Prof. Paul Canfield at *Ames Laboratory* in Iowa, following the procedure described in [219].

Prior to the AFM/MFM measurements, the crystal was glued on a copper substrate with low temperature silver epoxy to apply a biaxial strain on it at low tem-

peratures, similarly to the experiment in [71]. The same sample was also measured with STM at the *Laboratorio de Bajas Temperaturas de la Universidad Autonoma de Madrid* (LBTUAM) by Dr. Anton Fente in a set-up similar to the one described in [223]. Some of his STM results will be presented together with the AFM/MFM measurements to complement them, but the specifics of the STM experiments will not be given here as they are beyond the scope of this thesis. It is important to emphasize, that the sample was never unglued from the copper substrate, neither between AFM/MFM experiments, neither to perform the STM measurement. Therefore, the strain on the sample should be the same in the AFM/MFM and the STM measurements.

A relevant difference between STM and AFM/MFM is that the surface needs to be pristine to make STM measurements, whereas AFM/MFM measurements can be made on surfaces that have been exposed to air. Therefore, the sample was first inserted into the STM, cleaved in-situ in cryogenic vacuum, STM measurements were made and then we measured it with the AFM/MFM. Furthermore, in our set-up we can easily reach temperatures of 100 K and above, whereas the STM is optimized for working below 4 K. Therefore, we could trace the temperature dependence much better with the AFM system.

5.3.1 Topographic characterization

Topographic measurements were taken using the AFM dynamic mode described in section 2.1.3.7.1 with typical tip-sample separation around 10 nm.

Very flat surfaces were easily found after cleaving the sample, making possible topographic and magnetic images at 2 K up to $\approx 15 \times 15 \mu m^2$ with height differences of tens of nanometres. The cleaving of the surface is expected to occur in the c-axis [72]. An example of the crystal surface is presented in figure 5.5 together with a topographic profile, and the unit cell of the crystal.

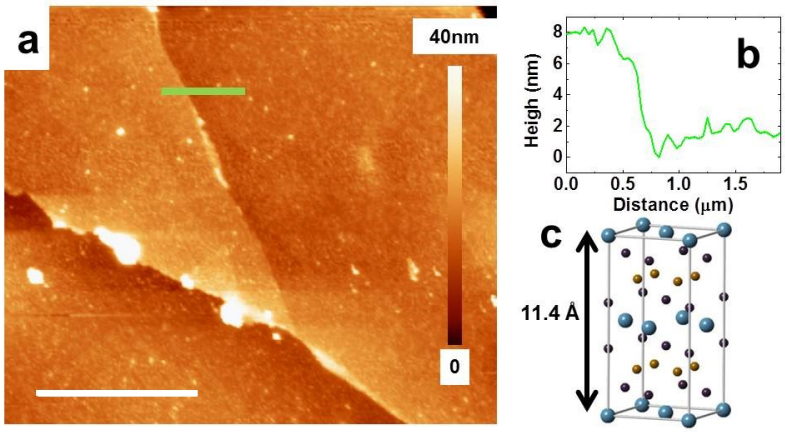

Figure 5.5: In a, a topographic AFM image of the sample at 100 K. The image shows large flat areas separated by steps of few nanometres high. Scale bar is 2μm. In b, the heigh of the profile marked as a green line on the topography is presented. In c, the unit cell of the sample. Ca atoms are represented in blue, Fe atoms in yellow and As atoms in purple.

5.3.2 Tetragonal to orthorhombic structural transition

As it was presented at the introduction of this chapter, a partial tetragonal to orthorhombic structural transition is expected for strained $Ca(Fe_{0.965}Co_{0.35})_2As_2$ samples at $T_{s,N}(\epsilon) \approx 100$ K.

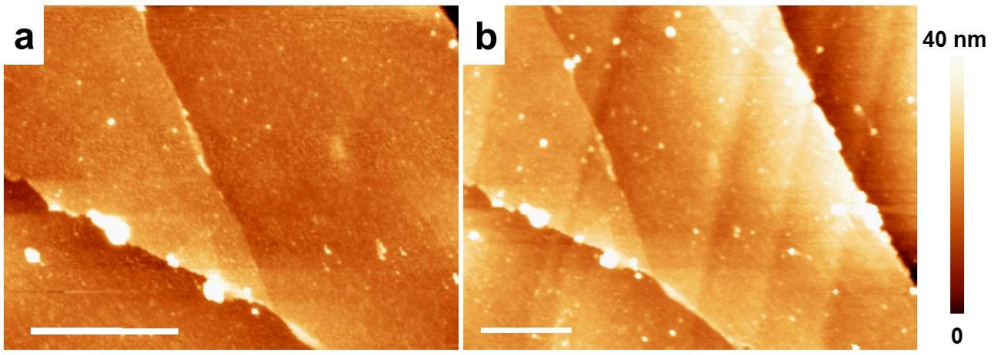

Figure 5.6: Topography of the strained $Ca(Fe_{0.965}Co_{0.35})_2As_2$ sample above and bellow $T_{s,N}(\epsilon)$. In a, a topographic image measured at 100 K. In b, the same area measured at 32 K. At 100 K the image shows atomically flat terraces with steps of few nanometres in between. At 32 K longitudinal stripes at an angle with respect to the image are visible. The scale bar represents 2μm.

We have performed AFM measurements above and below $T_{s,N}(\epsilon)$ in different

areas of the sample, finding radically different topographies. Above $T_{s,N}(\epsilon)$, in the tetragonal phase, flat terraces and small steps of few nanometres were found (figure 5.6 a). Slightly below the structural transition expected from [71], we have observed clear stripes in the topographic images (figure 5.6 b). The stripes are separated by flat regions, few microns wide and are straight and parallel on the whole field of view. The origin of the stripes will be discussed in the following.

5.3.2.1 Origin of the topographic stripes

The corrugation observed reminds AFM measurements below the tetragonal to orthorhombic transition in $BaTiO_3$ [224] and STM measurement below the Verwey transition in FeO_3 [225]. In both materials, the corrugation in the surface was associated to the reorientation of the structural domains due to the changes in the lattice parameters in the transition. We believe that our images can be explained in the same way.

The samples that present coexistence between orthorhombic and tetragonal domains, have domain boundaries separating both phases and different orientations of the same phase [71]. In the orthorhombic phase, the short axis, b_{ORTH}, is equal to the lattice parameter of the tetragonal phase, a_{TET} and therefore, the tetragonal/orthorhombic domain boundary will occur along the crystallographic direction determined by b_{ORTH}. Note in particular that the interface between these domains has no stress within the plane, because in-plane lattice constants coincide along the interface [71]. Domain boundaries between orthorhombic domains are in contrast, oriented at 45° with respect to the crystallographic axis, forming a twin boundary similar to the case of the parent compound $CaFe_2As_2$ described before [220]. In figure 5.7 two examples of the orthorhombic/tetragonal and orthorhombic/orthorhombic domain walls are presented.

We now will introduce a simple model originally developed to explain the corrugation in $BaTiO_3$ single crystals[226].

A condition for the formation of domain walls, is the matching and continuity of

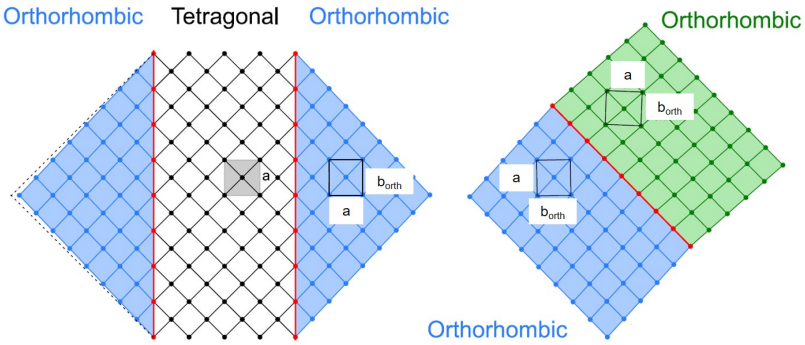

Figure 5.7: Example of the structural domain boundaries in strained $Ca(Fe_{1-x}Co_x)_2As_2$. In the left panel, two domain boundaries between two orthorhombic and a tetragonal domain, the domain boundary develops along the crystallographic direction determined by b_{ORTH}. In the right panel, the boundary between two orthorhombic domains, forming 45° with respect to the crystallographic axis. Different colours are used for different crystallographic domains. The domain wall is represented as a red line. Adapted from [72, 220].

the lattice at the wall [226]. Due to the differences in the c-axis lattice parameter between the two phases below $T_{s,N}$ in our crystal, this condition is fulfilled by the accommodation of the tetragonal and orthorhombic domains schematically shown in figure 5.8. The angle formed by the perpendicular and in-plane axis of both lattices at each side of the wall is not exactly 90°. It differs from 90° by an angle $\alpha = \arctan(c_{tet}/a_{tet}) + \arctan(a_{ort}/c_{ort})$ [226]. We have calculated the expected angle of the corrugation at the tet/orth domain wall using the lattice parameters obtained for strained samples from [71]. We have found a corrugation angle of $\alpha \approx 0.55°$.

Topographic features in form of stripes were also measured in STM experiments in the same sample (figure 5.9). In this case, the stripes are separated by tens of nanometres and are few Angstroms high. The STM measurements also show the 2x1 reconstruction of Ca atoms expected for $CaFe_2As_2$ [72, 227] covering most of the surface. The two main axis of the Ca reconstruction (corresponding to the two main axis of the Ca sublattice) form 45° with the crystallographic axis [189]. As is shown in figure 5.9, the reconstruction is found forming 45° with the topographic stripes (vertical lines in the figure), thus the stripes are oriented in the direction of the crystallographic axis. As it was presented in the introduction of the chapter, the domain boundary compatible with a direction of the crystallographic axis is the

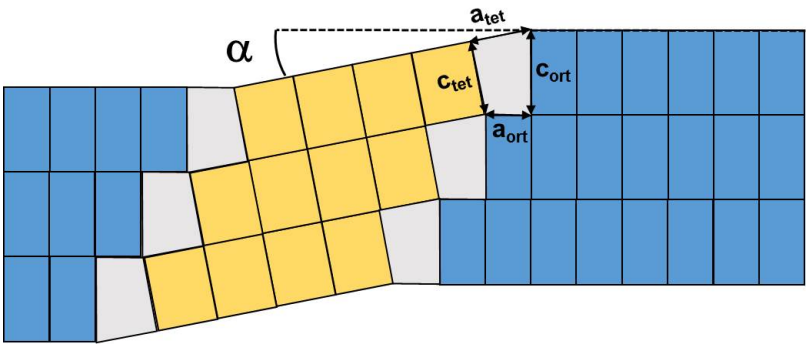

Figure 5.8: Scheme of the corrugation below the structural transition. The orthorhombic and tetragonal unit cells are represented in blue and yellow rectangles respectively. The unit cell at the interface is represented as a grey polygon.

tetragonal/orthorhombic domain wall, with the domain parallel to the a_{TET} and b_{ORTH} axis. This shows that stripes reflect the tet/orth domain boundaries.

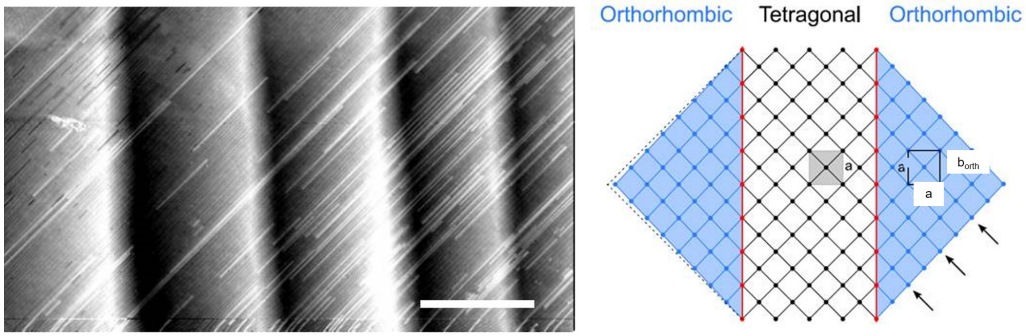

Figure 5.9: In the left panel, an STM topographic image taken at T<4.2K. The image display parallel elongated stripes, forming 45° with the 2x1 Ca reconstruction. The white scale bar represents 100 nm. In the right panel, a schematized tetragonal/orthorhombic domain wall. The 2x1 Ca reconstruction is marked with by black arrows and different domains are represented by different colours.

We have calculated the angle between domains at both sides of the stripes in AFM and STM images, finding that it remains almost constant in all the stripes with a value between 0.8 and 1.3°. A few STM and AFM selected images are shown together with their topographic profiles and the measured angle at the stripes in figure 5.10. It is noticeable that images with such different scales, present the same angle between domains.

The value of the angle measured at the stripes is larger than the calculated angle

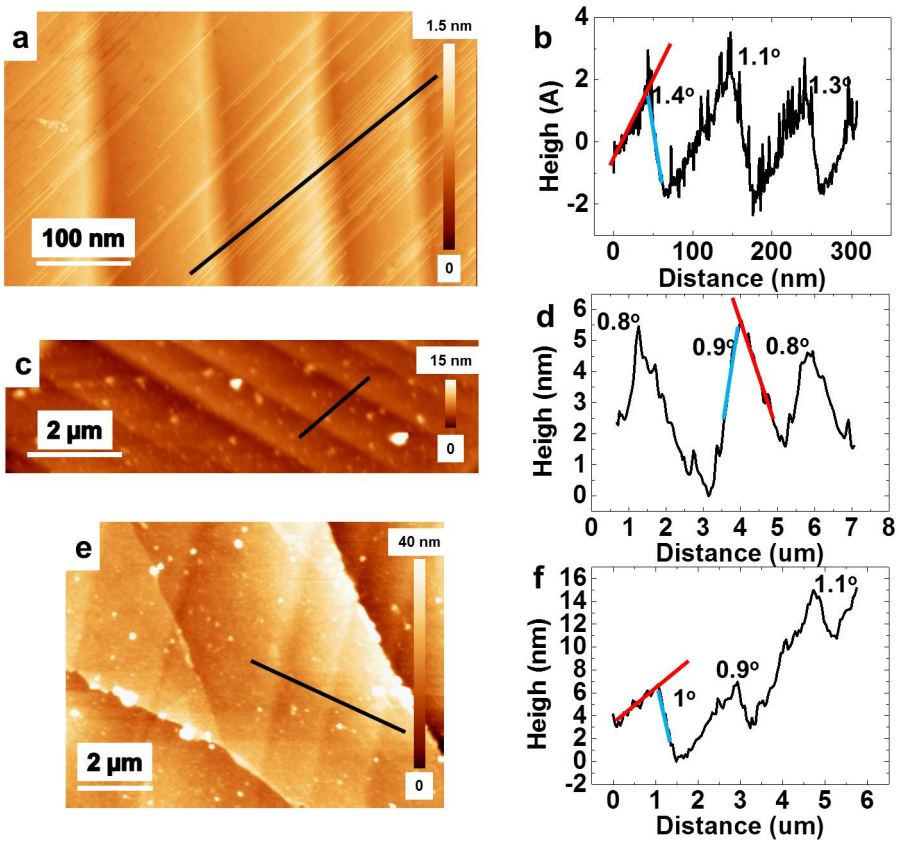

Figure 5.10: In the left column, thee topographic images measured by STM (a) and AFM (c and e). The images, show step-like features associated to the tetragonal-orthorhombic domain boundaries. In the right column, three topographic profiles measured black lines on the topographic images. All the step-like features showed in the profiles present an angle of ≈1° between the tetragonal and the orthorhombic domains. The surface of the tetragonal and orthorhombic domains is highlighted in the profiles using a blue and a red line respectively.

for this system ($\approx 0.55°$). But it is important to note that the distortion of the tetragonal and orthorhombic lattice is dependent on the strain and therefore on the substrate where the sample is glued. We have followed a similar procedure as in reference [71]. Thus, we can not unambiguously determine the magnitude of the distortion of the unit cells in our crystal. Moreover, the model used to calculate the distortion of the lattice at the boundary proposed in [226] is very simple. It assumes that the unit cell at the boundary is deformed, presenting exactly the same cell parameters of the tetragonal and orthorhombic phases at each side of the boundary, which does not have to be exactly true. For example, small deviation of $\approx 0.5\%$ from

the values of the cell parameters measured by [71], leads to a different $\alpha \approx 1°$.

We believe that, given the simple approximations made, the agreement is remarkable and provides a simple but successful explanation to the corrugation on the topography in our samples.

5.3.2.2 Evolution of the corrugation on the surface

We have measured the evolution of the stripes with the temperature in the same area. The results are shown in figure 5.11.

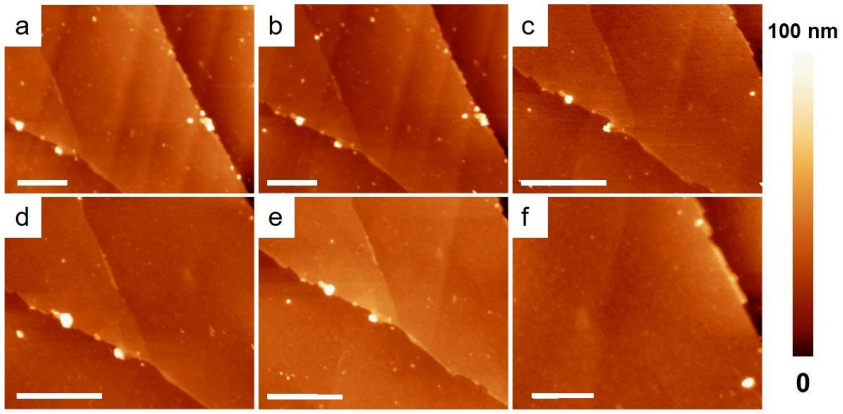

Figure 5.11: Evolution of the stripes on the surface with the temperature. Images measured when heating the sample at 17 K (a), 32 K (b), 55 K (c) and 68 K (d), e and f where measured after cooled the sample again at 55 K from 68 K. The stripes on the images become less visible at 55 K and they are not present at 68 K, they reappear at the same positions after decreasing the temperature again. Scale bars represent 2μm.

Images a, b, c and d were taken at 17 K, 32 K 55 K and 68 K respectively. The stripes remain at the same positions until the temperature reaches 55 K were some of the stripes start to vanish to be completely lost at 68 K. This temperature is close to the expected $T_{s,N}(\epsilon)$ [71]. Then, the sample was cooled down and measured again at 55 K (figure 5.11 e and f), obtaining the same position for the stripes that in the previous case. This shows that the stripes are a direct consequence of the orthorhombic to tetragonal phase transition.

It is important to note that the value of the critical temperature for this transition coincides well with the value obtained in the macroscopic phase diagram. Differences of a few K can arise because of slight differences in concentrations, annealing temperatures or strain.

5.3.3 Superconducting transition

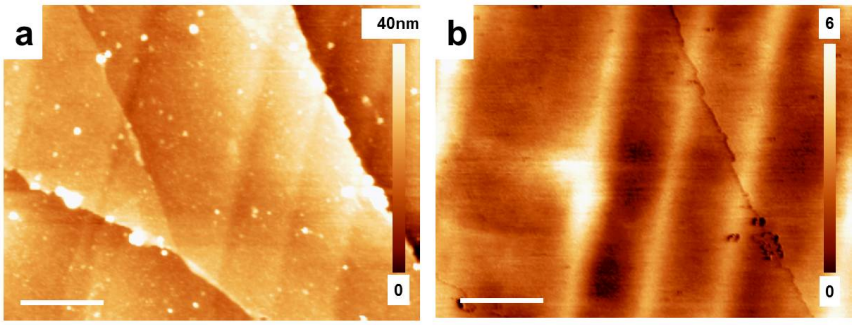

Figure 5.12: In a and b the topographic and magnetic image of the same area measured at 4.2 K and 1360 Oe. The magnetic image show elongated stripes that perfectly matches the topographic features originated when the sample is cooled below $T_{s,N}(\epsilon)$. White scale bars represents 2μm.

To further understand the behaviour of the tetragonal and orthorhombic domains on the sample and their interplay with the superconducting properties, we have measured the same area presented in figure 5.11, in the MFM mode at 4 K. After FC the sample at 1360 Oe below the superconducting critical temperature of free standing samples ($T_C \approx 16$ K), we have performed MFM measurements, finding that magnetic images show elongated an alternative paramagnetic and diamagnetic domains that exactly coincide with the topographic stripes observed in the AFM images (figure 5.12).

5.3.3.1 Evolution with the Temperature

To clarify if the magnetic signal is related or not with the superconducting transition, we have imaged the same area after FC the sample at 230 Oe, at different temperatures, keeping the magnetic field constant. We have found that the diamagnetic

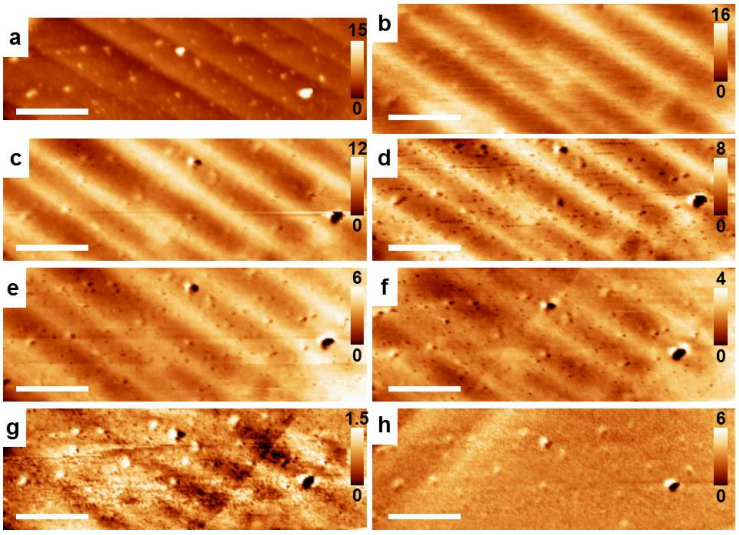

Figure 5.13: Evolution of the magnetic stripes with the temperature. In a, the topographic image of the area where the magnetic images were measured. In b-h, the magnetic images measured at 3.7 K, 4.8 K, 7.8K, 11.2K, 12.6K, 14 K and 16 K respectively. The contrast of the superconducting domains (white and light yellow), become fainter as the temperature increases, until they are not visible at 16 K in agreement with the expected T_C for the superconducting transition. All measurements were done with an applied field of 230 Oe. Scale bar is 2μm.

domains become broader and less intense as the temperature increases and they are completely gone at temperatures above 16 K, which is the same T_C as obtained using magnetization in the same sample [71].

We have combined the information obtained in the MFM measurements with the STM data. In STM experiments, conductance maps at zero magnetic field near the stripes show a gap opening that matches the expected gap for the material ($\Delta = 1.78 K_B T_C \approx 2.3$ mV) [69, 72]. STM conductance maps at 6 T also show vortex images at the tetragonal domains with intervortex distance corresponding to the expected one as is presented in figure 5.14 [72].

Therefore we can conclude that the diamagnetic domains observed in the MFM measurements are the result of the superconducting transition of the tetragonal domains of the sample that are still present at the sample below $T_{s,N}(\epsilon)$. The paramagnetic domains are related with the orthorhombic domains. It is interesting to note that the sample is split in two different phases normal/superconductor related with

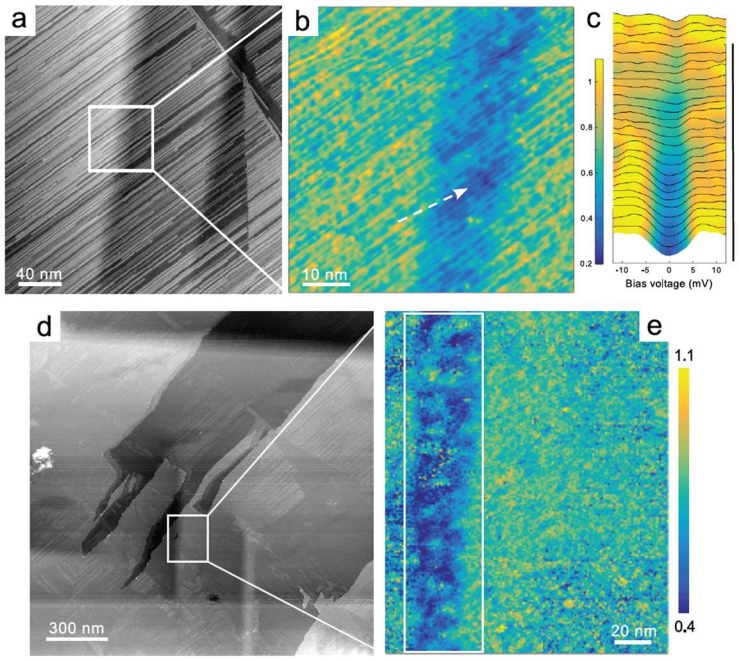

Figure 5.14: In a, a topographic STM image measured at 2 K. Surface shows a step-like feature similar to those found in the AFM measurement. In b, zero bias normalized conductance map of the area in the white square in a at zero magnetic field. In c, normalized conductance curves along the line in b, showing a superconducting gap in the expected energy range opening in the tetragonal domain. In d, an STM topographic image measured at 2 K. In e, zero bias normalized conductance map measured in the area of the white rectangle in d at H = 6 T, showing superconducting vortices (green spots on the blue area). Adapted from [72].

structural domains.

5.3.3.2 Evolution with the magnetic field

MFM measurements were taken at different applied magnetic fields at 4 K to characterize the evolution of the tetragonal-superconductor domains. The same area was mapped from perpendicular fields of 25 Oe to 1360 Oe after FC at 25 Oe. The results are shown in figure 5.15. The superconducting domains become thinner as the magnetic field increases. At the lower fields, there are some small domains perpendicular to the topographic stripes. When increasing the magnetic field we observe that the overall difference between large and small magnetization decreases and that the perpendicular domains disappear.

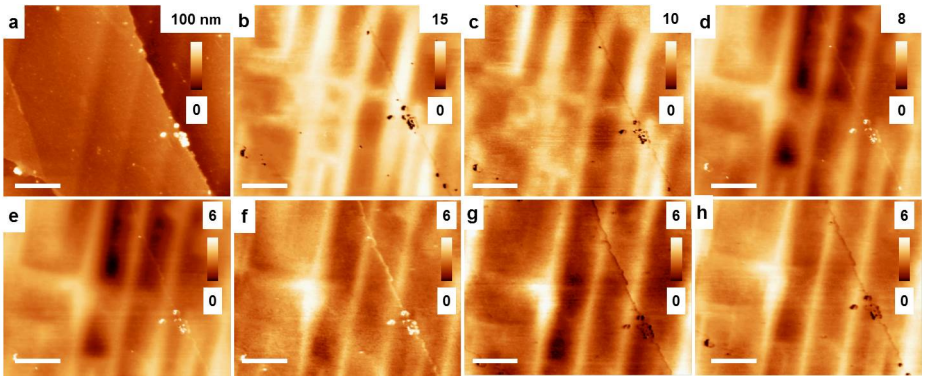

Figure 5.15: Evolution with the applied magnetic field of the magnetic stripes. In a, the topographic image of the area were the MFM images were measured. In b-h the magnetic images measured at 25, 70, 300, 430, 700, 1160 and 1360 Oe respectively. The superconducting domains (white and light yellow) become thinner as the magnetic field increases and some small domains perpendicular to larger domains along the vertical dimension are visible at the lower field and are not visible at higher fields. Scale bar is 2 μm.

The AFM resolution does not allow to determine if there are smaller topographic stripes associated to these domains. The possible origin of this orthogonal domains will be discussed in the following section.

5.3.4 Origin of the perpendicular domains

In the previous section, it was shown that there are some superconducting domains that are perpendicular to the topographic stripes and seems not to be related with any feature in the topographic image. This is nicely seen in images at larger scanned areas as the one presented in figure 5.16.

Figure 5.16 shows intersection of superconducting domains, always forming angles of $\approx 90°$. This may be explained by the formation of tetragonal-orthorhombic domain walls at each side of the twin boundaries between two orthorhombic domains as is schematized in figure 5.16. Two orthorhombic domains in a twin boundary, form an angle of $\approx 2°$ between them due to the orthorhombic distortion [69, 72]. As a result, the angle between two tetragonal domains at both sides of a twin boundary should differ from 90° by this small angle. This is compatible with the MFM images, where

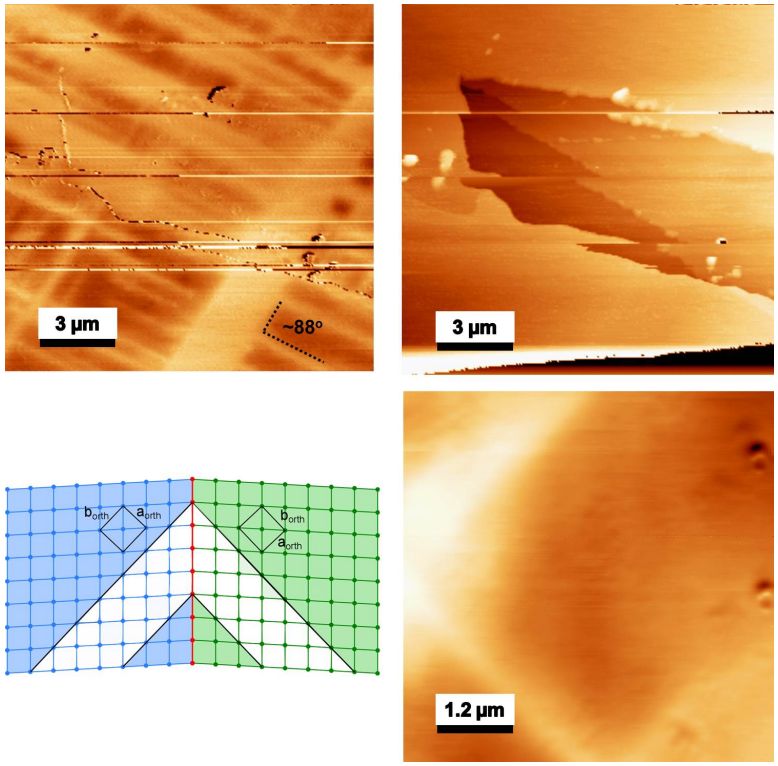

Figure 5.16: In the upper panel, two MFM and AFM images measured at 4K and 100 Oe. On the left, in the MFM image, elongated diamagnetic stripes associated to the tetragonal domains are observed. The stripes presents two main directions with an angle between them that differs from 90° by a few degrees. On the right, the topography image of the same area. In the lower panel, on the left, an schematic representation of two tetragonal domains at both sides of an orthorhombic twin boundary. Orthorhombic domains are represented in blue and green and tetragonal domains in white. The twin boundary is represented as a red line. On the right, a higher magnification of the MFM image centered at the intersection of three tetragonal domains.

the angle between the stripes gives values that differs from 90° by a few degrees, the same distortion that was found in the STM measurements for the 2x1 Ca reconstruction [72]. However, that would also result in some surface corrugation, which we do not observe. Another possibility is that fluctuations induce superconducting correlations in some parts of the orthorhombic phase. In both cases, this result shows that superconductivity in the tetragonal linear domains can be connected with each other.

In the topographic image of the same area, a huge step of several tens of nanome-

tres is shown at the centre of the image. On crossing the big step, the domain lines perfectly match. This shows that the domain walls extend along the c axis.

5.4 Conclusions

In this chapter we have studied the effect of strain in a $Ca(Fe_{0.965}\ Co_{0.35})_2As_2$ single crystal from the microscopic point of view. We have imaged the coexistence of tetragonal/orthorhombic domain walls below the strains mediated transition at $T_{s,N}(\epsilon)$.

Below the superconducting critical temperature of free standing samples, we have measured the formation of diamagnetic domains coinciding with the tetragonal domains. We have associated the diamagnetic domains with the superconducting transition of the remaining tetragonal phase. We have characterized their evolution with the applied magnetic field and the temperature. STM images are consistent with our results, showing the opening of a superconducting gap and the existence of vortices in the tetragonal domains below T_C.

Quite likely, the size of the domains can be modified by applying uniaxial stress to the substrate, either perpendicular or parallel to the stripes. Or simply by changing the substrate. For instance, the thermal expansion of glass is of -0.1% which should result in a differential thermal expansion of 0.6% between sample and substrate and eventually lead to modified length scales in the domain size and distribution. Thus, strain might be used as a control parameter to produce novel kinds of superconducting systems, such as intrinsic Josephson junction arrays or to use the domain structure to improve vortex pinning. At very low magnetic fields we observe sometimes linear diamagnetic structures in the orthorhombic phase that might join elongated tetragonal domains, suggesting that such a coupling between elongated domains can indeed happen in some parts of the sample.

To our knowledge, this is the first experimental work showing phase separation associated to strain below T_C in pnictides. The likely absence of magnetic order in the tetragonal domains, having in close spatial proximity a magnetically ordered domain, suggests that magnetic and superconducting order are both antagonistic,

although they are probably fed by the same fluctuations.

CHAPTER 6

Manipulation of the crossing lattice in $Bi_2Sr_2CaCu_2O_8$

6.1 Introduction

Bismuth strontium calcium copper oxide, or BSCCO, is a family of high-temperature superconductors having the generalized chemical formula $Bi_2Sr_2Ca_{n-1}Cu_nO_{2n+4}$, with $n = 2$ being the most commonly studied compound, also called Bi-2212. Discovered in 1988 [228], BSCCO was the first high-temperature superconductor which did not contain a rare earth element. It is a cuprate superconductor, an important category of high-temperature superconductors sharing a two-dimensional layered (perovskite) structure with superconductivity taking place in the copper oxide planes.

The crossing lattice of Josephson vortices (JVs) and pancake vortices (PVs) in Bi-2212 has attracted a lot of attention in the scientific community in the last decades. Theoretical works have described the interaction between PVs and JVs at different regimes [44, 46, 47, 49, 55] and experimentalist have imaged the crossing lattice by several techniques like magneto optical (MO) imaging [60–62] (figure 6.1 a), Bitter decoration [58, 59] (figure 6.1 b), and Hall microscopy [63–65] (figure 6.1 c).

Those works have characterized the crossing lattice at different polar angles and strengths of the applied magnetic field. They have found good agreement between

theory and the experimental values of the lattice parameters of the JV lattice and the distribution of PVs on top of JVs [63, 64]. They have also achieved PVs manipulation in some extent by using a rotating magnetic field [65]. But, the local manipulation of single PVs and the experimental measurement of the force between PVs and JVs has not been achieved yet. On the other hand, local manipulation of single vortices was achieved in YBCO, another anisotropic high-T_C superconductor. Authors in [106, 113] have demonstrated that MFM can be used to manipulate vortices.

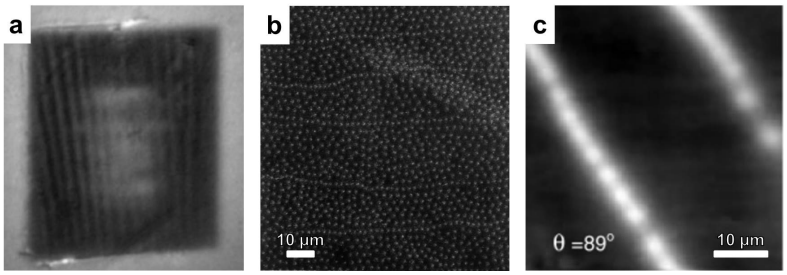

Figure 6.1: In a, a MO image measured in a Bi-2212 single crystal showing vortex chains due to the accumulation of PVs on top of JVs. Obtained at T = 72 K, $B_\perp$ = 13.8 Oe and $B_\parallel$ = 60 Oe. In b, bitter decoration image in a Bi-2212 single crystal showing PV chains on top of JVs with PVs in between. Obtained at T = 72 K, $B_\perp$ = 12 Oe and $B_\parallel$ = 32 Oe. In c, a SHPM image of PV chains decorating two JVs in a Bi-2212 single crystal at T = 81 K, $B_\perp$ = 0.8 Oe and $B_\parallel$ = 35 Oe. In the three images, vortices appear as white dots on the black background. Adapted from [58, 62] and [56].

6.1.1 Interaction between JVs and PVs

At small fields and high anisotropy factor, γ, PVs do not influence much the structure of JVs. However, there is a finite interaction energy between PV stacks and JVs due to the PVs displacements under the action of the JVs in-plane currents [46]. This interaction causes an effective attractive force between PVs and JVs. The force per unit length along the c-axis, between a PV stack and a JV stack was calculated in [46] as:

$$f_x = \frac{1.4\phi_0^2}{4\pi^2 a_z \gamma^3 s^2 log(\lambda_{ab}/s)} \tag{6.1}$$

Where ϕ_0 is the quantum of flux, a_z the lattice parameter of the JV lattice in the c-axis direction, s the distance between superconducting layers and λ_{ab} the penetration depth for superconducting currents in the a-b plane.

6.1.2 Manipulation of the crossing lattice in Bi-2212

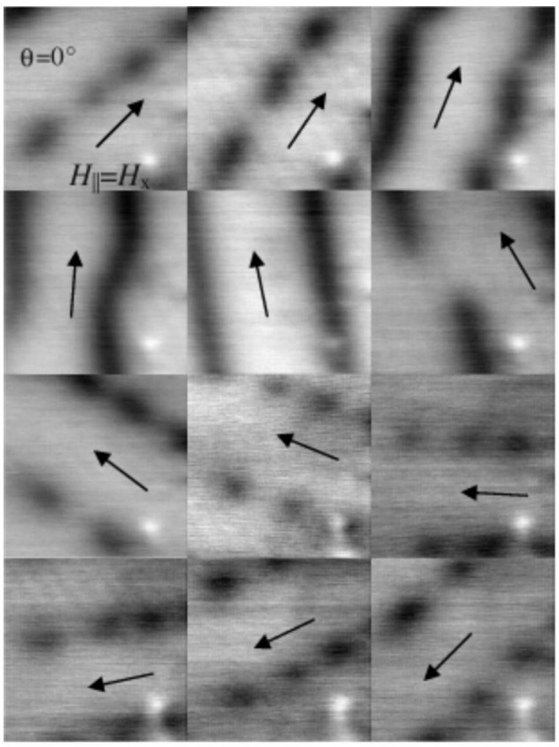

Figure 6.2: SHPM images at T = 80 K and $H_{\parallel}$ = 27.5 Oe, with the JV lattice rotated by (left to right, top to bottom, anticlockwise rotation): 0°, 15°, 30°, 45°, 60°, 75°, 105°, 120°, 135°, 150°, 165°, and 180°. PVs appear as black dots in the grey background. The black arrow indicates the direction of the magnetic field. Scan size 28 μm × 28 μm. Adapted from [65].

Previous works have been able to manipulate the crossing lattice in Bi-2212,. They were able to drag PVs with the JVs by changing the direction of the in-plane magnetic field at temperatures close to T_C [56, 65]. An example is presented in figure 6.2, where the crossing lattice was successfully rotated in Bi-2212 at 80 K.

Authors in [65] argue that the attraction force between JVs and PVs at 80 K in their crystals is three times larger that the pinning force of the PVs. Therefore changing the direction of the JVs by rotating the in-plane the magnetic field, drags

the PVs with them.

6.1.3 Observation of crossing lattice with MFM and its manipulation

6.1.3.1 Force of a MFM tip on a vortex

MFM tips exerts a given force on magnetic samples. This fact is often a disadvantage, as the tip-sample interaction could change the magnetic state of the sample and somehow introduce artefacts in the measurement [125–127, 229]. In the present chapter, we deliberately have used this force to manipulate superconducting vortices. We have magnetized the tip parallel to the vortices to give attraction force between them. Such a force will decrease as the tip-sample separation increases.

To obtain an insight on the force acting on the vortices, we have followed the calculation of the tip-vortex interaction made by [230]. This model, treats both, tip and vortex, as monopoles. The model assumes that the tip is and infinitely long and narrow cylinder with its mains axis and magnetization parallel to the Z axis and the vortex as a monopole residing at a distance λ below the surface of the superconductor, which fills the half space z<0 with a magnetic field [141, 231]:

$$\vec{B}(\vec{r},z) \approx \frac{\phi_0(\vec{r}+(z+\lambda)\hat{z})}{2\pi(R^2+(z+\lambda^2))^{3/2}} \tag{6.2}$$

Where r is the radial distance from the tip, z the vertical distance and R the tip radius. Thus, the force acting on the tip due to the interaction with the superconducting vortex is:

$$\vec{F}(\vec{r},z) \approx m\vec{B}(\vec{r},z) \tag{6.3}$$

where m is the dipolar moment per unit length of the tip. Maximizing the force of equation 6.3 in z, we obtain:

$$F_z^{max} = \frac{m\phi_0}{2\pi(z+h_0)^2} \tag{6.4}$$

where h_0 is the offset in the tip-sample separation due to the approximation of the monopole model. The maximum lateral force is approximated as:

$$F_{lat}^{max} = \alpha F_z^{max} \tag{6.5}$$

Here, α is a constant of proportionality with a value between 0.3 and 0.4 [231, 232].

6.1.3.2 Vortex manipulation in YBCO

Previous measurements have shown the possibility to drag vortices in the High-T_C superconductors, YBCO [106, 113]. In particular, the authors in [106] have measured the interaction of a moving vortex with the local disorder potential. They found an unexpected and marked enhancement of the response of a vortex to pulling when they wiggled it transversely. They showed that wiggling the vortex along the fast scan direction of the MFM image, allows to move the vortex along the slow axis of the image when the magnetic tip is close enough to the sample and therefore the magnetic force between tip and sample increases. A schematic representation of the process is presented in figure 6.3 together with real MFM images of stationary and dragged vortices.

6.2 AFM/MFM studies

We have presented how previous works have manipulated individual vortices in YBCO and groups of PVs trapped on JVs in Bi-2212 at temperatures close to T_C. But, prior to our work, individual manipulation of PVs on JV has not been studied yet. Moreover, the force to move a PV out a JV remains unknown. This was our main motivation and the starting point of our study in this compound.

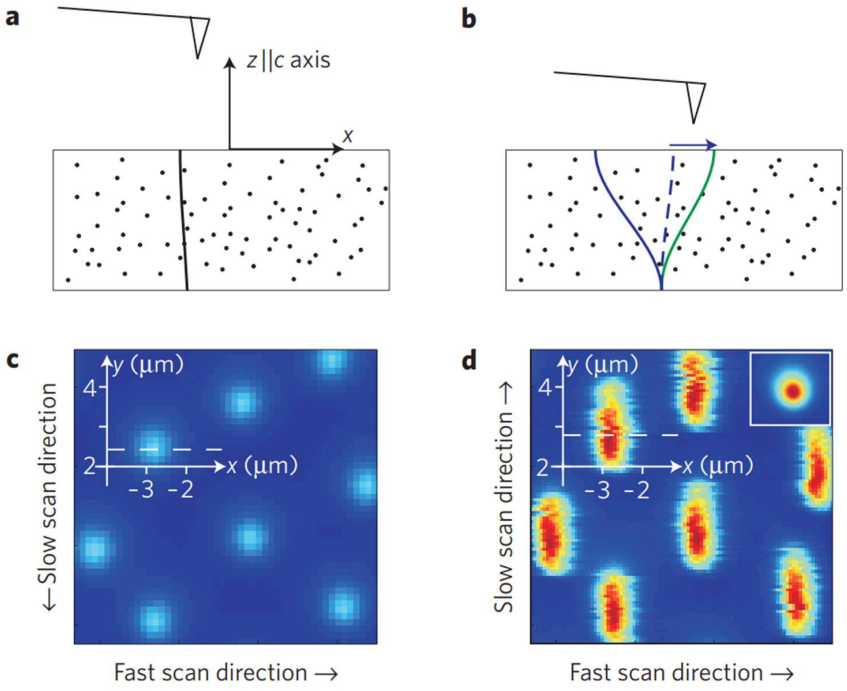

Figure 6.3: Scheme of vortex movement by MFM. The MFM tip (triangles) attracts a vortex (thick lines) in a sample with random pinning sites (dots). In a, the applied force F_{lat} is too weak to move the vortex due to the large tip-sample distance. In b, the vortex moves right, as the tip rasters over it in the direction indicated by the arrow. The blue line illustrates the initial vortex position, the dashed blue line shows an intermediate position and the green line shows the final configuration. In c and d, MFM scans for two different scan heights, z = 420 nm ($F_{lat}^{max} \approx 6$ pN), not enough to perturb vortices (c) and z = 170 nm ($F_{lat}^{max} \approx 12$ pN), enough to drag the vortices (d). Inset: Scan at 5.2 K, showing a stationary vortex. Adapted from [106].

We make several manipulation experiments. First, we show that PVs can be displaced by exciting them with the tip motion and turning the magnetic field. Then, we show how the tip motion can move PVs from one JV to another. We have also crossed JVs after inducing a JV lattice at an angle with respect to a strongly pinned JV. Finally, we have studied the PVs entry in the sample at low temperatures, determining that it is governed by pinning. Our experiments show that phase patterns in superconductors, even when these are strongly pinned, can be controlled by the action of small forces and the direction of the magnetic field.

AFM/MFM measurements were performed in the set up of our lab described in

section 2.1 in a Bi-2212 single crystal. The crystal was grown by the group of Prof. Kadowaki at the *University of Tsukuba* in Japan, following a procedure similar to the one described in [233]. It has a superconducting critical temperature of $\approx$ 88 K.

6.2.1 Topographic characterization

For topographic characterization of the sample, AFM measurements were made in a Bi-2212 single crystal glued with low temperature silver epoxy to our LT-AFM sample holder and exfoliated at room temperature using scotch tape. The cleaving of the surface occurs in the c-axis [234, 235]. We have aligned the crystal with the main axis of our coil system, to apply the Z component of the magnetic field along the c axis and B_x and B_y along the in-plane crystalline axis. Topographic measurements were taken using the dynamic mode described in section 2.1.3.7.1 with typical sample tip separation around 10 nm.

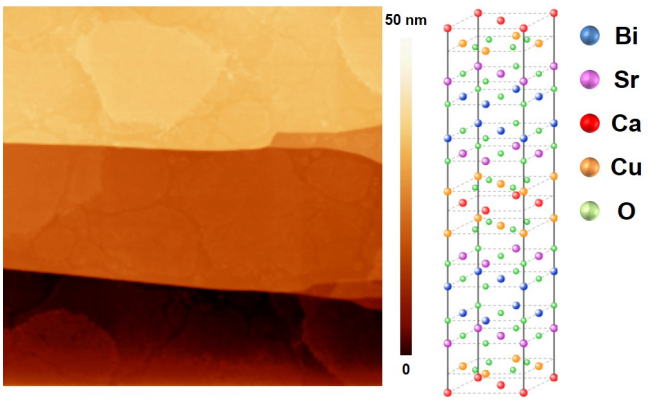

Figure 6.4: An AFM topographic image of the cleaved Bi-2212 single crystal and its unit cell (right). The topography shows atomically flat terraces with with steps $\approx$ 15 nm high.

After exfoliating the sample, it presents very large areas with flat terraces and atomic steps. The atomic flatness of the surface have allowed us to measure areas of $\approx 10 \times 10 \mu m^2$ at 5 K. An example of the crystal surface is presented in figure 6.4 together with the unit cell.

6.2.2 Obtaining the Crossing Lattice

We have imaged the crossing lattice in our Bi-2212 single crystal using the MFM mode described in 2.1.3.7.2. First, we have cooled the sample under an applied magnetic field of 30 Oe in the Z direction down to 5.3 K and measured the resulting PV distribution. We obtained the regular Abrikosov lattice with the intervortex distance expected for the applied magnetic field (figure 6.5).

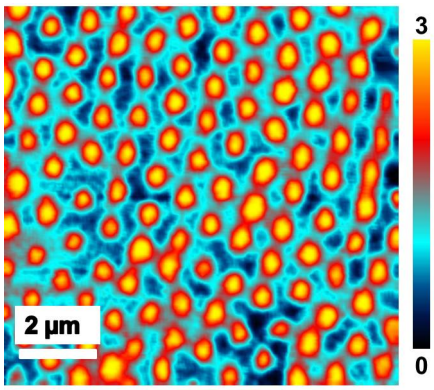

Figure 6.5: MFM image of the regular Abrikosov lattice. Measured in the Bi-2212 single crystal after FC at 5.3 K with a perpendicular magnetic field of 30 Oe.

After measuring the Abrikosov lattice, we ramped the field in Z down to zero and applied a magnetic field of 200 Oe in the Y direction. We obtained images as shown in Fig.6.6 a. The Abrikosov lattice is interspersed with lines of PVs pinned on JVs. To eliminate as much as possible PVs, we heated the sample quickly above 70 K and cooled it again to 2 K. This freed the PVs from their pinned positions and more JVs decorated with PVs are visible (figure 6.6 b). After repeating this process several times we have obtained areas with almost every PV pinned on top of a JV (figure 6.6 c). The same process was always used to obtain the decorated JVs in the following sections.

Images in figure 6.6 were used to calculate the anisotropic factor of our Bi-2212 crystal (for the details of the calculation see chapter 1). Using the distance between JVs, we have calculated $\gamma = 250$ and $a_z = 15.4$ nm. The size of the JVs was also calculated using the relation $a_{JV} = \gamma s/2$ and $b_{JV} = s$ [48], finding $a_{JV} = 375nm$ and $b_{JV} = 0.75nm$.

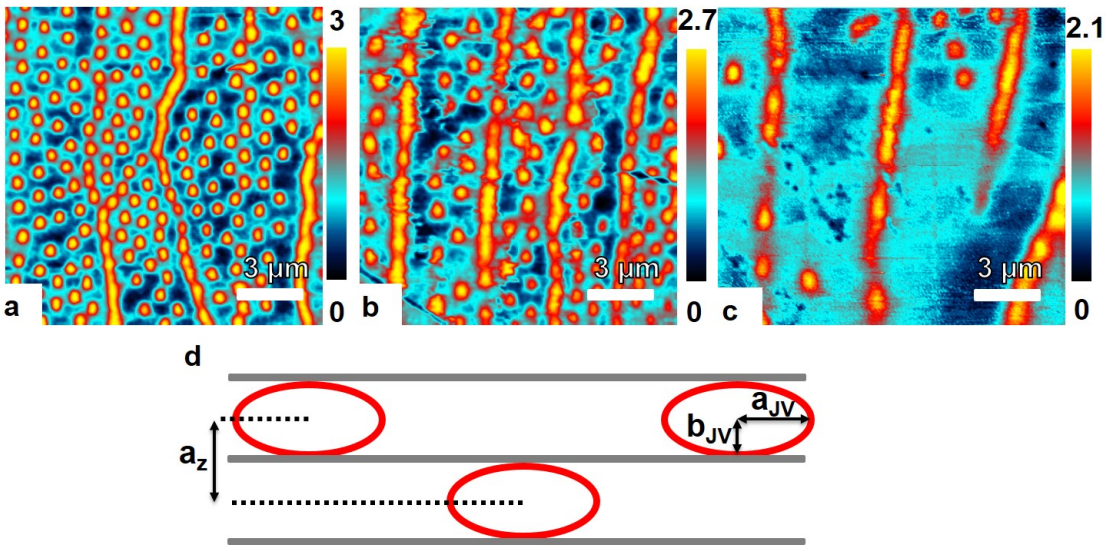

Figure 6.6: Decorated JVs with PVs. Images obtained with $B_{||} = 200$ Oe along the Y direction, at 5.3 K. In a, the vortex arrangement after FC with $B_{\perp} = 30$ Oe and switching it to zero and $B_{||}$ to 200 Oe at 5.3 K. Some decorated JVs are visible with a significant number of trapped PVs in between. In b, a different configuration after heating the sample up to 70 K and cooling it down again to 5.3 K. More decorated JVs are visible and the number of PVs in between have decreased. After repeating the same process several times, almost all the PVs are decorating JVs (c). The field of view has moved during heating, so the images are not taken at the same position. In d, a schematic representation of the JV lattice in Bi-2212. The gray lines represent the CuO planes and the red ellipses the JVs.

The penetration depth, λ_{ab}, of Bi-2212 single crystals was experimentally determined in previous works using different methods [143–145, 236]. These works have reported values between 180-270 nm for λ_{ab}. Thus, the lateral size of the PVs and the JVs is comparable. Therefore, only one PV row fits inside a JV.

6.2.3 Evolution of the crossing lattice with the temperature

We have measured the evolution of the crossing lattice at the same area for different temperatures. Images in figure 6.7 were measured at 5.5 K, 12 K and 15.5 K. They show that the vortices width increases with the temperature. At 20 K the flux distribution becomes homogeneous over the surface and no magnetic contrast was obtained. This, suggest that PVs are able to move far enough from their equilib-

rium position to overlap between them. Figure 6.7 also represents the evolution of the magnetic profile of the same vortex at different temperatures, it shows that the magnetic contrast decreases as the temperatures increases. The potential well of the size of the pancake vortices was extracted from the evolution of this magnetic profile. It represents the thermal energy associated to each temperature of the experiment versus the vortex profile width.

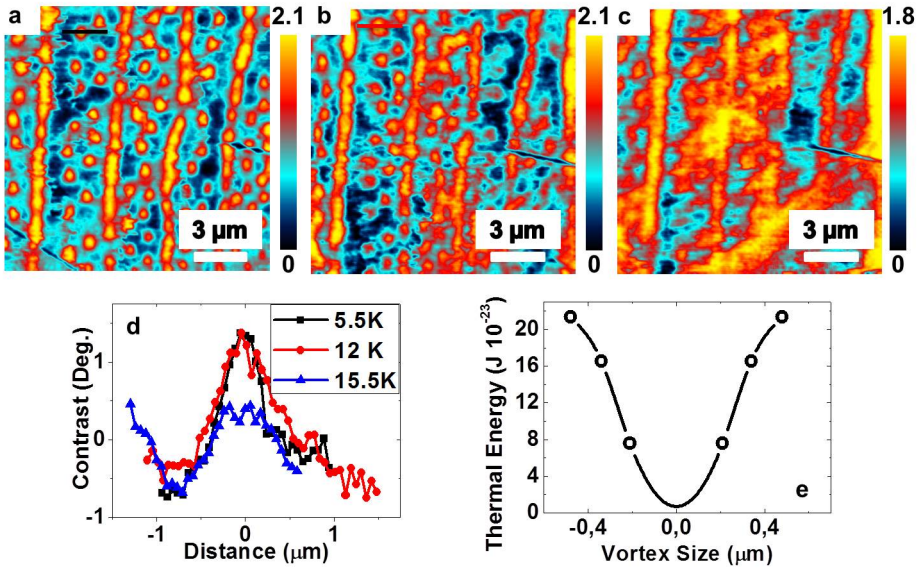

Figure 6.7: Thermal motion of PVs. In a, b and c, MFM images measured at 5.5 K, 12 K and 15.5 K respectively at the same area. The magnetic field is B_y= 200 Oe in the three images. The size of the PVs increases with temperature due to thermal motion. In d, the magnetic profiles, measured at the same PV at the three temperatures. The PV is marked by black red and blue lines in the images. In e, the potential well of the PVs extracted from the data in d, the line is a guide to the eye.

The temperature at which we observe strong vortex motion, $T^*_m \approx 20$ K, obtained from figure 6.7 is far below the melting temperature reported by previous works, $T_m \approx 80$ K, for the same material at low fields [190, 237–239]. Moreover, according to [44], the decrease of the melting temperature with the tilted angle of the magnetic field is not enough itself to explain such a low melting temperature. More likely, the melting of PVs is not exclusively a consequence of large thermal fluctuations. It has been pointed out by [106, 113, 232] that lateral magnetostatic forces during MFM imaging could lead to a depinning of vortices. In our experiment, dragging due to the

magnetostatic attraction between PVs and tip could also play a significant role, which suggest that the vortex-probe interaction is large enough to force PVs to move outside their equilibrium position at temperatures above 20K. This result gives a powerful tool to vortex manipulation in this system, as it shows that PVs can be manipulated by the MFM probe at reasonable low temperatures.

6.2.4 Manipulation of the crossing lattice

We have successfully manipulated the crossing lattice in our crystal. As a first step, we have manipulated a disordered arrangement of PVs. Then, we have successfully manipulated PV rows pinned on JVs.

6.2.4.1 Manipulation of PVs

We have successfully manipulated PVs combining the action of the in-plane magnetic field and the force of the MFM tip on the PVs. Figure 6.8 shows the evolution of an arbitrary arrangement of PVs when changing the angle of the in-plane magnetic field. The fast scan axis of the MFM is parallel to the X direction in all images. Figure 6.8 a, shows the original configuration of PVs, with round shapes and well localized positions at 12 K. After rotating the magnetic field by 10 degrees (figure 6.8 b) the same area was measured again. In the image, several PV magnetic profiles are elongated in the direction of the magnetic field. This behaviour is better seen after changing the angle to 45° (figure 6.8 c), 70° (figure 6.8 d) and 90° (figure 6.8 e). PV profiles became more elongated as the angle between the slow scan axis and the in-plane magnetic field decreases, always following the direction of the magnetic field. The elongation is maximum when the magnetic field is aligned with the slow axis of the MFM. Figure 6.8 f, summarizes the evolution of the PV elongation as a function of the angle between the fast scan axis and the magnetic field.

As discussed in the previous paragraph, we can ascribe such elongated magnetic patterns to vortices moving below the tip. The stray field of the MFM tip exerts a given lateral force, F_{lat}, on the vortices. The lateral force can be decomposed in

two components, $F_{lat,s}$ and $F_{lat,f}$ in the directions of the slow and fast scan axis respectively. $F_{lat,f}$ shakes the vortices, moving them back and forth on its potential well while $F_{lat,s}$ can be use to drag vortices along the scan axis if the gain in energy of the vortex due to $F_{lat,f}$ is enough [106, 109, 230] (figure 6.9 a). Such a scenario is of course not compatible with a perfect harmonic potential at a single pinning site. Instead, it suggests that vortices have multiple relaxation time scales. They seem to remain at positions far from equilibrium for a long time. Between each passage of the tip there are a few ms. This seems to be compatible with the complex pinning patterns and vortex trajectories observed in recent SOT measurements [240].

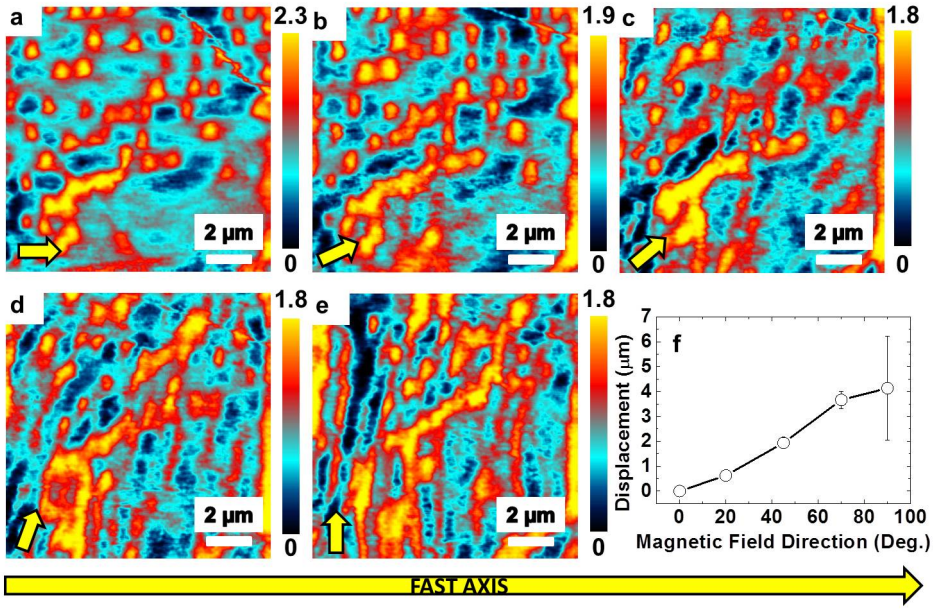

Figure 6.8: Motion of PVs by the combined action of the MFM tip and the rotating magnetic field. We show the evolution of a set of PVs when changing the direction of $B_{||}$ = 200 Oe (marked as a yellow arrow in the images). In a, b, c, d and e, MFM images measured with an angle of $B_{||}$ with respect the X axis of 0°, 10°, 45°, 70° and 90° respectively. Some PVs presents elongated magnetic profiles in the direction of $B_{||}$ as the angle increases. The direction of the fast scan axis is represented by a yellow arrow at the bottom. In f, we show the average PVs displacement vs the angle, the line is a guide to the eye.

In addition, a parallel magnetic field applied to Bi-2112, will enter the material in form of JVs. As a consequence, superconducting currents flow on the CuO planes perpendicular to the direction of $B_{||}$. These currents exerts a Lorentz force, F_L, on

the PVs parallel to the direction of $B_{\parallel}$.

Combination of the two previous forces was used to manipulate PVs. From figure 6.8, it is clear that there is no movement when both forces are perpendicular and maximum when they are parallel. The process is schematized in figure 6.9. When $F_{lat,s}$ and F_L are perpendicular, no vortex movement was found, suggesting that $F_{lat,s}$ was not strong enough to manipulate the PVs. When the angle, Θ, between $F_{lat,s}$ and F_L is different from 90°, PVs movement was measured in the direction of $B_{\parallel}$. The movement, in this case is due to the sum of F_L and the projection of F_{ts} in the direction of F_L, as is shown in figure 6.9 c. PVs movement is greater when $\Theta = 0$ as the total forces becomes maximum and PVs can be dragged far from their equilibrium positions (figure 6.9 d).

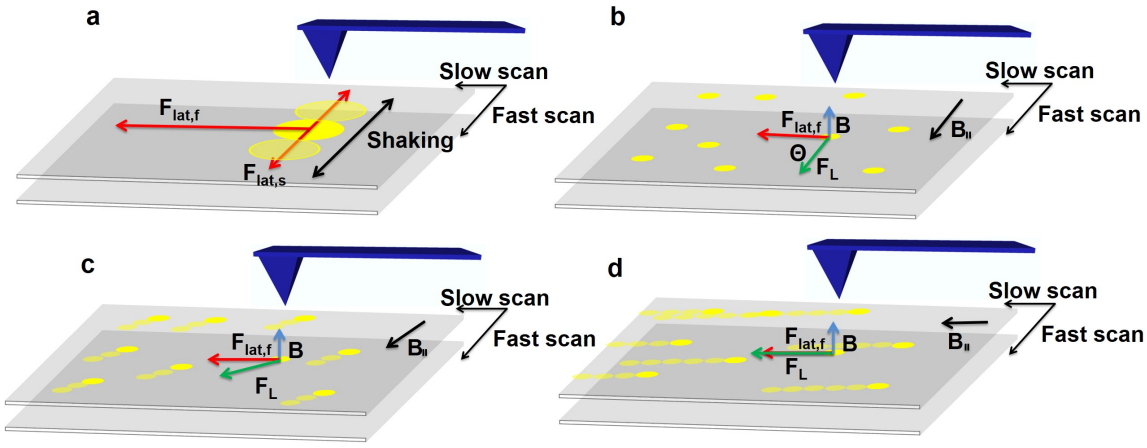

Figure 6.9: Scheme of the motion of PVs by the combined action of the MFM tip and the rotating magnetic field. The MFM tip is represented as a blue triangle, the CuO layers as grey planes and the PVs as yellow circles. We use transparent yellow circles to represent the PVs movement. In a, the force of the MFM tip acting on a PV is schematized. The force is decomposed in two components, $F_{lat,s}$ and $F_{lat,f}$ in the directions of the slow and fast scan axis respectively. $F_{lat,s}$ shakes the PV back and forth and $F_{lat,f}$ drags the PV. In b, the Lorentz force, F_L, acting on the PVs and the slow scan axis are perpendicular. They are not strong enough to move the PVs. In c, the the parallel magnetic field form an angle $\Theta \neq 90°$ with the slow axis and the sum of both forces becomes strong enough to drag PVs a short distance in the direction of F_L. In d, both forces are parallel and the PVs move a larger distance.

We have estimated the value of Lorentz force acting on a PV due to the JV

supercurrents. We have used the expression for the supercurrents flowing on the surface due to the presence of JVs from [48]:

$$J_{\parallel} \approx \frac{\phi_0}{\mu_0 2\pi\lambda_{\perp}\lambda_{\parallel}^2} \tag{6.6}$$

From equation 6.6 we have estimated the force acting on a PVs of about 50 pN. Pinning force of PVs is therefore stronger as F_L by itself is not enough to drag PVs. We have calculated the force exerted by the MFM probe on a PV by using the equation 6.5. For our calculation we have use typical values of $\alpha = 0.35$, $h_0 = 250$ nm and $m = 30$ nAm following [122, 230, 241], and the experimental tip-sample separation of 120 nm, obtaining $F_{lat}^{max} = 80$pN. PVs movement was achieved by the combination of the force of the MFM tip and the Lorentz force. Thus, we estimate the force needed to drag isolated PVs of ≈ 130 pN.

6.2.4.2 Manipulation of PVs on top of JVs

Figure 6.10 a, shows JVs decorated with PVs at 5.3 K. In the image, the in plane component of the magnetic field is aligned with the slow axis of the scan. PVs are well localized on top of the JVs with some clusters in between, without any signature of vortex movement. After changing the direction of the scan by 90° and increasing the temperature up to 12 K, the same area was measured again. Result are presented in figures 6.10 b and c.

Figure 6.10 b, was obtained by scanning from the bottom to the top and from right to left of the image while 6.10 c, was obtained by scanning from the top to the bottom and from right to left. From visual inspection is clear that the straight trajectories of the PVs follow the direction of the tip during the scan.

In this case PVs are not randomly arranged on the surface but pinned on JVs forming rows. In this particular configuration we have found PVs movement in the direction of the scan. In this case, the force on the PVs from the tip is strong enough to depin them from the JVs, moving them from one JV to another. The process is

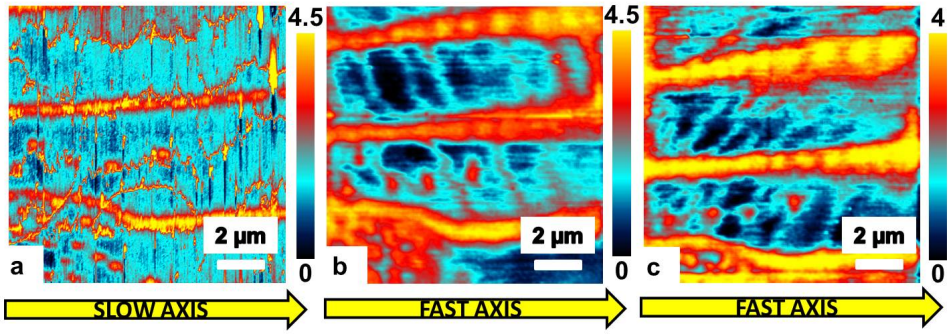

Figure 6.10: Triggering motion of PVs between JVs by the MFM tip. In a, we show an image measured at 5.4 K and B_x= 200 Oe with the slow scan axis parallel to B_x. In b and c, we show the same field of view at 12 K, changing the scanning direction (marked by the yellow arrow) with respect to a. Between b and c we change the direction over which the tip is scanned during imaging, from left to right and bottom to top in b and from right to left and top to bottom in c. Note that, in addition to the signal on top of the JVs, we observe stripes in between JVs.

schematized in figure 6.11, where the trajectories of three PV are shown, solid yellow circles represents their equilibrium positions on the JVs and empty yellow circles their positions during the scan as a result of the force of the MFM tip.

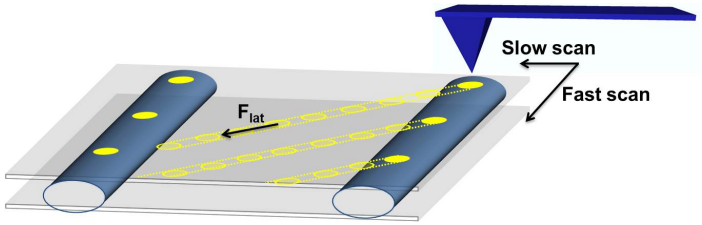

Figure 6.11: Scheme of the motion of PVs between JVs by the MFM tip. The MFM tip is represented as a blue pyramid, the JVs as blue cylinders, the PVs as yellow circles and the CuO layers as grey planes. The movement of the PVs is schematized by transparent yellow circles. The MFM tip exerts a given force, F_{lat} on the PVs in the direction of the scan.

We have calculated the attractive force per unit length along the c-axis, between a PV stack and a JV stack following equation 6.1. We have used $\gamma = 250$ and $a_z =$ 15.4nm calculated in previous sections, obtaining $f_x = 2.28 \cdot 10^{-7}$N/m. Assuming a sample thickness of about 0.5 mm, the attractive force will be $f_x \approx 114$ pN, smaller than the estimated force to drag isolated PVs and comparable to the force of the MFM tip on the PVs.

6.2.5 Manipulation with the aim to cross Josephson vortices

Previous works have demonstrated that the JV-PV interaction is sufficiently strong to indirectly pin JVs stacks at the location of pinned PVs [242]. We have used this behaviour to generate and keep a JV in a fixed direction and then cross other JVs with it by rotating the in-plane magnetic field.

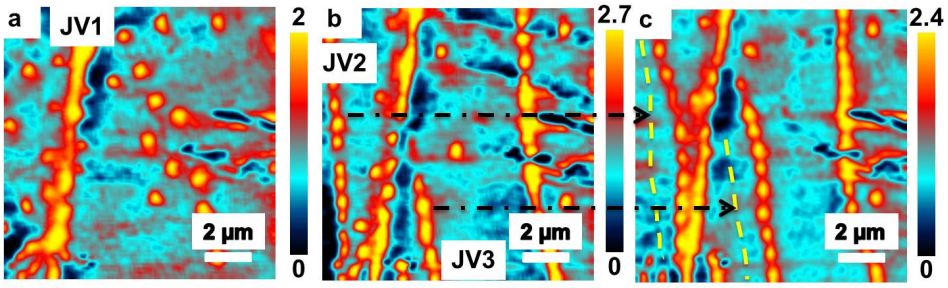

Figure 6.12: Crossing JVs. In a, a JV (denoted by JV1) pinned at a topographic feature at 5.3 K and $B_{||}$ = 200 Oe. In b, the same area, measure after heat the sample up to 20 K and modifing the direction of $B_{||}$ by -5° with respect to the Y axis. Three new JVs appear in the image, two of them (denoted as JV2 and JV3) cross JV1. In c, after heat and cool the sample again, JV2 and JV3 have changed slightly their position. We mark the previous position of JV1 and JV2 by dashed yellow lines. Remarkably, JV2 is attracted to JV1 and JV3 intersects JV1.

After finding an area with a longitudinal topographic feature, we have applied a tilted magnetic field with $B_{||}$, parallel to the topographic feature, generating a series of decorated JVs at 5.3K. As a result, one JV and several PVs were pinned to the topographic feature. Then, we have heated the sample up to 20 K and cooled down to 5.3 K quickly. After that, we have measured the same area again. All PVs that were pinned on the JVs where depinned, except the ones on the JV on the topographic feature labelled as JV1 (figure 6.12 a). The pancake intervortex distances within the feature are consistent with the presence of a JV, indicating that the original JV is still pinned to the feature. Then, the angle of the in-plane magnetic field was changed by -5° generating a new JV lattice tilted 5° with respect to the topographic feature. The new JV lattice crosses the topographic feature in two points (figure 6.12 b). Finally, the sample was heated up to 20 K and cooled down again to 5.5K to favour the JV lattice movement. After scanning the area again, we have found that the JVs have

moved a few microns crossing the topographic feature at new points (figure 6.12 c). In figure 6.12 c) the JV labelled as JV2 approaches to the topographic feature in a asymptotic way while the JV labelled as JV3 form a kink with the feature.

A similar situation was previously reported by [63]. In this work, they were able to split the PVs row on top of a JV in two 'forks' by quickly changing the direction of the magnetic field. In their work, the double row of PVs relaxed back to a single chain after a few minutes. This suggest that the JV was not split in two branches. Instead, the most possible scenario is that when changing the direction of magnetic field and therefore the direction of the JV, some of the PVs are dragged with it and others are not. Finally the PVs that were not dragged are attracted again to the JV forming a single row again.

Our case is completely different as the JV configuration was stable during all the experiment (several hours). Thus, we suggest that we are in a crossing flux configuration, where we have successfully crossed three JVs. The MFM does not allow to determine the direction of the JVs at the crossing point, but a twist, crossing and reconnection of the magnetic field inside the material is the most likely scenario as it was previously suggested by [243, 244].

6.2.6 Pinning of the crossing lattice at low temperatures

A previous work, has reported the possibility of manipulate JVs and PVs by changing the azimuthal angle of the applied magnetic field at high temperatures (80 K), where the pinning potential is weak [65]. Authors in [65], argue that at 80 K the pinning force acting on the PVs in their crystal is three times smaller that the attractive force between JVs and PVs. Thus, changing the direction of $B_{\parallel}$ modifies the direction of the JVs and drags the PVs with them.

We have measured the evolution JVs decorated by PVs at low temperatures (5.5 K and 10 K) for different azimuthal angles. We have rotated the magnetic field in the XY plane up to 120° without finding any movement of the crossing lattice. JVs and PVs remain pinned at their original positions and do not change with the direction

of the magnetic field. At 10 K only a increment of the PV profiles was measured. Results are presented in figure 6.13.

Our results prove that pinning of PVs on the JV lattice at low temperatures is large enough to avoid any JV movement with the magnetic field.

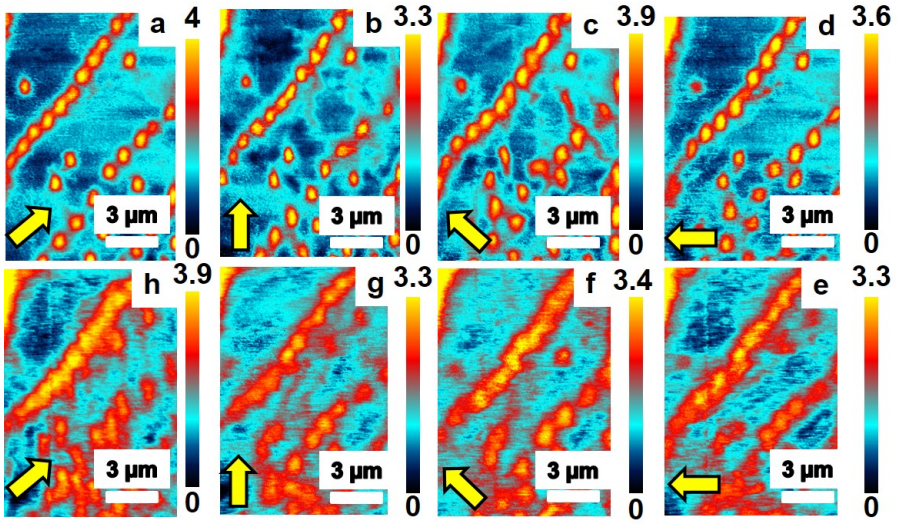

Figure 6.13: Pinned crossing lattice in rotating magnetic fields. In the figure we show the same field of view when changing the direction of $B_{\parallel}$=200 Oe. The direction of $B_{\parallel}$ is marked by a yellow arrow at the images. a, b, c and d were measured at 5.3 K and e, f, g and h at 10 K. Clearly, JVs and PVs remain pinned, in spite of the varying direction of the magnetic field at both temperatures.

The effect of pinning in our crystal is also seen when ramping $B_{\perp}$ from 0 Oe to 2000 Oe as is presented in figure 6.14. First, we have obtained two JVs decorated with PVs at 5.5 K. Then we have increased the perpendicular magnetic field from 0 Oe to 2000 Oe in several steps, measuring the surface at each step. Surprisingly, the vortex distribution almost does not change until 2000 Oe where the flux distribution becomes homogeneous. Then, the magnetic field was decreased to 50 Oe and the hexagonal vortex lattice was recovered (Figure 6.14 i).

This indicates that the magnetic flux does not penetrate to the centre of the sample until the field reaches a threshold value (2000 Oe in our case), accumulating flux elsewhere.

The vortex distribution at low fields in High-T_C superconductors with rectangular

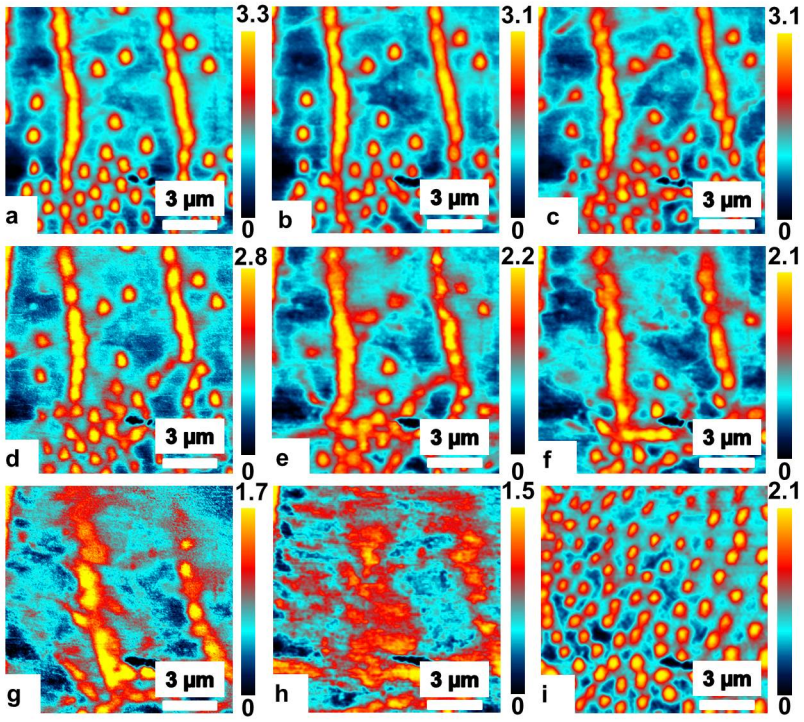

Figure 6.14: Ramping the Z field in crossed lattices. We show the evolution of the crossing lattice with the perpendicular component of the magnetic field ($B_\perp$) at constant temperature (5.3 K). $B_\parallel$ remained constant at 200 Oe in the Y direction and the perpendicular component was 0 Oe (a), 100 Oe (b), 300 Oe (c), 500 Oe (d), 750 Oe (e), 1000 Oe (f), 1500 Oe (g), 2000 Oe (h). Clearly, the crossed lattices remain roughly at the same position below $B_\perp = 1500$ Oe. At $B_\perp = 1500$ Oe, no vortices are resolved. When decreasing $B_\perp$ down to 50 Oe, we observe again the lattice of PVs.

geometry results from the competition of pinning and geometrical barriers (GBs) [245]. The GB is formed by the interplay between the vortex line tension and the Lorentz force that is induced by the circulating Meissner currents [245–251]. At low fields, vortices entering the sample accumulate at the edges until the Lorentz force acting on them is strong enough to sweep them to the center of the sample. When $B_\perp$ is increased above the penetration field, $B_p = B_{C1}\sqrt{W/d}$, (W and d are the width and thickness of the sample), vortices entering through the edges are swept by the Meissner currents toward the center, where they accumulate, giving rise to a dome-shaped induction profile. Due to the effect of GBs, the vortex penetration is delayed significantly. In the presence of bulk pinning, the initial penetrating vortices do not

reach the center of the sample even at B>B_p. In this case, the Lorentz Force need to overcome both, the GBs and the pinning forces to sweep vortices to the center of the sample. It has been also shown that JVs in Bi-2212 serve as narrow channels for easy vortex entry and exit through the geometrical barrier (GB) [252], in this case, PVs still accumulate at the centre of the sample but with some of them decorating JVs outside the central dome.

We have found that there is not vortex entry to the center of the samples at low fields. PVs only reach the center of the sample at fields above 2000 Oe. We have calculated for our sample B_p ≈600Oe and found vortices at the center at almost 2000 Oe. This can be explained by pinning.

6.2.7 Evolution of the PV lattice with the polar angle of the magnetic field

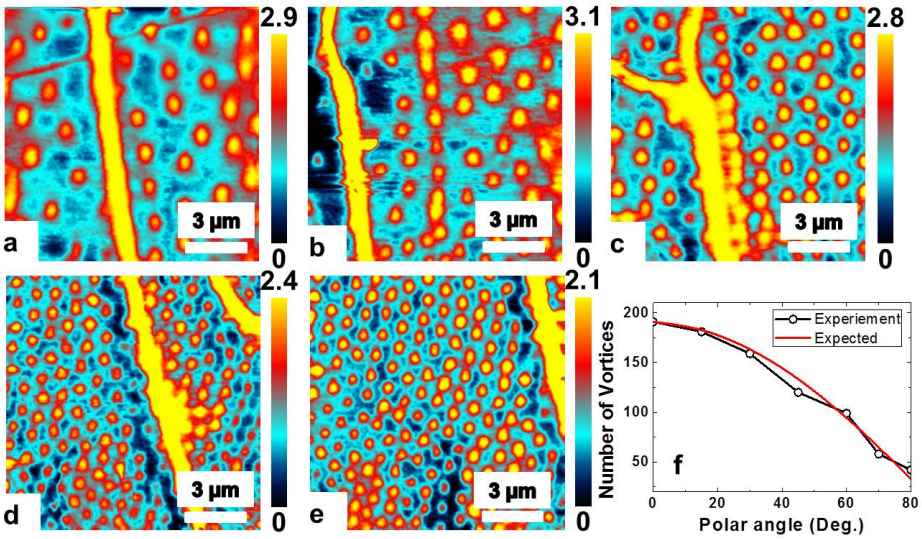

Figure 6.15: Evolution of the PV lattice with the polar angle. We show a set of images measured at constant magnetic field (27.5 Oe) and azimuthal angle ($\phi = 0$) but different polar angle. All are taken at 5.3 K in FC conditions, with the magnetic field applied above T_C = 88 K. Polar angle is 80° in a, 70° in b, 60° in c, 15° in d and 0°in e. The field of view is different in each image. In i, we compare the measured vortex density with the expected value within Ginzburg-Landau theory.

We have investigated the influence of $B_\perp$ from a different approach. To avoid the

pinning of the PVs, each measurement was taken at FC conditions. The sample was heated above its critical temperature and the absolute value of the magnetic field was held constant to 27.5 Oe for different polar angles. Then, the sample was cooled down to 5.5 K. This procedure avoids the effect of pinning and allows to measure the evolution of the lattice at different angles, but does not allow to measure an specific area due to the thermal drift of the sample. Results are summarized in Figure 6.15.

All images of $12 \times 12 \mu m^2$ were measured at different positions of a larger area about $30 \times 30 \mu m^2$. The number of vortices at the area, follows the expected behaviour (figure 6.15 g), indicating that at high temperatures where the pinning potential is smaller, PVs enter to the centre of the sample with an homogeneous distribution.

6.3 Conclusions

In this chapter, we have studied the crossing lattice of Bi-2212 single crystal at low temperatures and low fields. We have successfully manipulated an arbitrary arrangement of PVs and the crossing lattice of JVs and PVs. We have measured the dependence of the PV movement with the angle between the in-plane magnetic field and the scan of the MFM. We have measured the necessary force to manipulate isolated PVs and PVs trapped on JVs, finding values of $\approx 120pN$. We were able to cross three JVs. We have also demonstrated that pinning determines the entry of PVs from the edges to the centre of the sample at low temperatures.

To our knowledge,this is the first work showing local manipulation of the crossing lattice in a superconductor.

CHAPTER 7

General conclusions

In this project we have used magnetic force microscopy at low temperatures to study three different superconducting compounds. We have focused our research in the study of superconducting vortices and their manipulation. We have also studied the decomposition in superconducting and ferromagnetic domains in a $Ca(Fe_{0.965}Co_{0}.035)_2As_2$ single crystal and the exfoliation and deposition of several 2D systems. Regarding the experimental system, we have used a set-up that allows us to perform AFM-MFM measurements between 1.8 K and 300 K, applying magnetic fields in any direction of the space up to 5 T in the Z direction and 1.2 T in the X and Y directions.

With this set up, we have characterized for the first time the hysteresis cycle of MFM commercial probes as a function of the temperature from 1.8 to 300 K. We have also found that the MFM images of superconducting vortices show star-like features at vortex positions when the MFM tip is magnetized bellow its coercive field.

We have successfully exfoliated several superconducting crystals and graphene and deposit them in different substrates using a combination of PDMS silicon stamps and the regular scotch tape method. We have investigated three different systems with this method, BSCCO on SiO_2, β-Bi_2Pd on SiO_2 and graphene and FLG on β-Bi_2Pd.

In the case of BSCCO flakes deposited in SiO_2, we were able to measure one thick flake at low temperatures and characterize its magnetic profile in the superconducting state at different magnetic fields and temperatures.

For β-Bi_2Pd flakes deposited on SiO_2, we were able to exfoliate and deposit flakes of this system for the very first time, down to some tens of nanometers. This results open the possibility to study the superconducting behavior in the 2D limit in this system in the future.

We have also transfered graphene and FLG flakes on top of a β-Bi_2Pd single crystal and developed a experimental procedure to unambiguously localize graphene and FLG flakes on top of β-Bi_2Pd using a combination of friction and KPM measurements with an AFM. We have also probed that this method allow to localize the flakes at ambient and at low humidity conditions.

We have observed two different regimes in the patterns of pinned superconducting vortices at low magnetic fields in the single gap superconductor β-Bi_2Pd. We have shown that lines of vortices form at defects due to pinning at very low magnetic fields, while at higher fields the vortex lattice acts as a whole, leaving a regular hexagonal lattice even below H_{c1}. Crystalline strain close to defects determines the vortex arrangements at low fields and leads to sizable modifications of the local superconducting screening properties, as shown by the measured increase in the penetration depth λ close to defects.

We have transfered a $\approx$ 1 cm $\times$ 1 cm graphene sheet on top of a β-Bi_2Pd single crystal with the electromechanical transfer method and measured the vortex lattice of the β-Bi_2Pd crystal at the superconducting state at 2K trough the graphene layer. This experiment, opens the possibility of characterize this heterostructure in future experiments to determine if there is a gap opening in the graphene in this situation.

We have studied the effect of strain in a $Ca(Fe_{0.965}\ Co_{0.35})_2As_2$ single crystal from the microscopic point of view. We have imaged the coexistence of tetragonal/orthorhombic domain walls bellow the strains mediated transition at $T_{s,N}(\epsilon)$. Bellow the superconducting critical temperature of free standing samples, we have measured the formation of diamagnetic domains coinciding with the tetragonal domains. We have associated the diamagnetic domains with the superconducting transition of the remaining tetragonal phase. We have characterized their evolution with the applied magnetic field and the temperature. At very low magnetic fields we observe

linear diamagnetic structures in the orthorhombic phase that might join elongated tetragonal domains, suggesting that such a coupling between elongated domains can indeed happen in some parts of the sample. To our knowledge, ours is the first experimental work showing phase separation associated to strain bellow T_C in pnictides.

We have studied the crossing lattice in a Bi-2212 single crystal at low temperatures and low fields. We have successfully manipulated an arbitrary arrangement of PVs and the crossing lattice of JVs and PVs. We have measured the dependence of the PV movement with the angle between the in-plane magnetic field and the scan of the MFM. We have measured the necessary force to manipulate isolated PVs and PVs trapped on JVs. We were able to cross three JVs. To our knowledge, ours is the first work showing manipulation of the crossing lattice in a superconductor.

In summary, we have addressed systems that include proximity induced superconductivity in graphene, phase separation induced by coexistence with magnetic order and observation and manipulation of 2D vortex lattices. We have found new results, as the increase in penetration depth in graphene when decreasing the coupling with a superconductor, we have shown the existence of a new intrinsically inhomogeneous superconductor and have characterized complex phase patterns in a 2D superconductor. The combination of AFM and MFM in a vector magnet provides a useful platform to study and manipulate novel forms of superconductivity.

Bibliography

[1] Gianni Profeta, Matteo Calandra, and Francesco Mauri. Phonon-mediated superconductivity in graphene by lithium deposition. *Nat Phys*, 8(2):131–134, Feb 2012.

[2] A. Di Bernardo, O. Millo, M. Barbone, H. Alpern, Y. Kalcheim, U. Sassi, A. K. Ott, D. De Fazio, D. Yoon, M. Amado, A. C. Ferrari, J. Linder, and J. W. A. Robinson. p-wave triggered superconductivity in single-layer graphene on an electron-doped oxide superconductor. 8:14024 EP –, Jan 2017. Article.

[3] Rekha Narayan and Sang Ouk Kim. Surfactant mediated liquid phase exfoliation of graphene. *Nano Converg*, 2(1):20, Oct 2015. 50[PII].

[4] Sajedeh Manzeli, Dmitry Ovchinnikov, Diego Pasquier, Oleg V. Yazyev, and Andras Kis. 2d transition metal dichalcogenides. 2:17033 EP –, Jun 2017. Review Article.

[5] Rui Dong and Irma Kuljanishvili. Review article: Progress in fabrication of transition metal dichalcogenides heterostructure systems. *Journal of Vacuum Science & Technology B, Nanotechnology and Microelectronics: Materials, Processing, Measurement, and Phenomena*, 35(3):030803, 2017.

[6] Miguel Ayan-Varela, Oscar Perez-Vidal, Juan I. Paredes, Jose M. Munuera, Silvia Villar-Rodil, Maria Diaz-Gonzalez, Cesar Fernandez-Sanchez, Virgilia S. Silva, MÃşnica Cicuendez, Mercedes Vila, Amelia Martinez-Alonso, and Juan M. D. Tascon. Aqueous exfoliation of transition metal dichalcogenides assisted by dna/rna nucleotides: Catalytically active and biocompatible nanosheets stabilized by acid-base interactions. *ACS Applied Materials & Interfaces*, 9(3):2835–2845, 2017. PMID: 28029778.

[7] Christophe Brun, Tristan Cren, and Dimitri Roditchev. Review of 2d superconductivity: the ultimate case of epitaxial monolayers. *Superconductor Science and Technology*, 30(1):013003, 2017.

[8] Takashi Uchihashi. Two-dimensional superconductors with atomic-scale thickness. *Superconductor Science and Technology*, 30(1):013002, 2017.

[9] A T Bollinger and I Bozovic. Two-dimensional superconductivity in the cuprates revealed by atomic-layer-by-layer molecular beam epitaxy. *Superconductor Science and Technology*, 29(10):103001, 2016.

[10] X. Wang, L. X. You, D. K. Liu, C. T. Lin, X. M. Xie, and M. H. Jiang. Thin-film-like $BSCCO$ single crystals made by mechanical exfoliation. pages 13–17, 2012.

[11] Yuan Huang, Eli Sutter, Norman N. Shi, Jiabao Zheng, Tianzhong Yang, Dirk Englund, Hong-Jun Gao, and Peter Sutter. Reliable exfoliation of large-area high-quality flakes of graphene and other two-dimensional materials. *ACS Nano*, 9(11):10612–10620, 2015. PMID: 26336975.

[12] Efrén Navarro-Moratalla, Joshua O. Island, Samuel Mañas-Valero, Elena Pinilla-Cienfuegos, Andres Castellanos-Gomez, Jorge Quereda, Gabino Rubio-Bollinger, Luca Chirolli, Jose Angel Silva-Guillén, Nicolás Agraït, Gary A. Steele, Francisco Guinea, Herre S. J. van der Zant, and Eugenio Coronado. Enhanced superconductivity in atomically thin TaS_2. 7:11043 EP –, Mar 2016. Article.

[13] Katsuyoshi Komatsu, Chuan Li, S. Autier-Laurent, H. Bouchiat, and S. Guéron. Superconducting proximity effect in long superconductor/graphene/superconductor junctions: From specular andreev reflection at zero field to the quantum hall regime. *Phys. Rev. B*, 86:115412, Sep 2012.

[14] C. Ojeda-Aristizabal, M. Ferrier, S. Guéron, and H. Bouchiat. Tuning the proximity effect in a superconductor-graphene-superconductor junction. *Phys. Rev. B*, 79:165436, Apr 2009.

[15] M Hayashi, H Yoshioka, and A Kanda. Superconducting proximity ef-

fect in graphene nanostructures. *Journal of Physics: Conference Series*, 248(1):012002, 2010.

[16] Chuan Li. *Superconducting proximity effect in graphene and Bi nanowire based junctions*. PhD thesis, Universite Paris, 2014.

[17] Jungdae Kim, Victor Chua, Gregory A. Fiete, Hyoungdo Nam, Allan H. MacDonald, and Chih-Kang Shih. Visualization of geometric influences on proximity effects in heterogeneous superconductor thin films. *Nat Phys*, 8(6):464–469, Jun 2012. Letter.

[18] Jun-Yi Ge, Joffre Gutierrez, A. Lyashchenko, V. Filipov, Jun Li, and Victor V. Moshchalkov. Direct visualization of vortex pattern transition in ZrB_{12} with ginzburg-landau parameter close to the dual point. *Phys. Rev. B*, 90:184511, Nov 2014.

[19] Victor Moshchalkov, Mariela Menghini, T. Nishio, Q. H. Chen, A. V. Silhanek, V. H. Dao, L. F. Chibotaru, N. D. Zhigadlo, and J. Karpinski. Type-1.5 superconductivity. *Phys. Rev. Lett.*, 102:117001, Mar 2009.

[20] J. Gutierrez, B. Raes, A. V. Silhanek, L. J. Li, N. D. Zhigadlo, J. Karpinski, J. Tempere, and V. V. Moshchalkov. Scanning hall probe microscopy of unconventional vortex patterns in the two-gap MgB_2 superconductor. *Phys. Rev. B*, 85:094511, Mar 2012.

[21] Taichiro Nishio, Vu Hung Dao, Qinghua Chen, Liviu F. Chibotaru, Kazuo Kadowaki, and Victor V. Moshchalkov. Scanning squid microscopy of vortex clusters in multiband superconductors. *Phys. Rev. B*, 81:020506, Jan 2010.

[22] H. J. Zhao, V. R. Misko, J. Tempere, and F. Nori. Pattern formation in vortex matter with pinning and frustrated intervortex interactions. *Phys. Rev. B*, 95:104519, Mar 2017.

[23] E. Herrera, I. Guillamón, J. A. Galvis, A. Correa, A. Fente, R. F. Luccas, F. J. Mompean, M. García-Hernández, S. Vieira, J. P. Brison, and H. Suderow. Magnetic field dependence of the density of states in the multiband superconductor $\beta - \mathrm{bi_2Pd}$. *Phys. Rev. B*, 92:054507, Aug 2015.

[24] E. et al Herrera. Preprint. 2016.

[25] J. Kačmarčík, Z. Pribulová, T. Samuely, P. Szabó, V. Cambel, J. Šoltýs, E. Herrera, H. Suderow, A. Correa-Orellana, D. Prabhakaran, and P. Samuely. Single-gap superconductivity in $\beta-Bi_2Pd$. *Phys. Rev. B*, 93:144502, Apr 2016.

[26] H. Kamelingh Onnes. *Leiden Commum.*, 120B:122, 1911.

[27] W. Meissner and R. Ochsenfeld. Ein neuer effekt bei eintritt der supraleitfähigkeit. *Naturwissenschaften*, 21(44):787–788, 1933.

[28] Michael Tinkham. *Introduction to Superconductivity.* McGRAW-HILL, 1974.

[29] Charles Poole Horacio Farach Richard Creswick Ruslan Prozorov. *Superconductivity.* Elsevier, 2014.

[30] F. London and H. London. The electromagnetic equations of the supraconductor. *Proceedings of the Royal Society of London A: Mathematical, Physical and Engineering Sciences*, 149(866):71–88, 1935.

[31] L.D. Landau V.L. Ginzburg. *Zh.Eksp.Teor.Fiz*, 20:1064–1082, 1950.

[32] J. Bardeen, L. N. Cooper, and J. R. Schrieffer. Microscopic theory of superconductivity. *Phys. Rev.*, 106:162–164, Apr 1957.

[33] A. A. Abrikosov. *Zh. Eksp. i Teor. Fiz.*, 32B:1442, 1957.

[34] Leon N. Cooper. Bound electron pairs in a degenerate fermi gas. *Phys. Rev.*, 104:1189–1190, Nov 1956.

[35] H. Fröhlich. Theory of the superconducting state. i. the ground state at the absolute zero of temperature. *Phys. Rev.*, 79:845–856, Sep 1950.

[36] T. E. Faber. The Intermediate State in Superconducting Plates. *Proceedings of the Royal Society of London Series A*, 248:460–481, December 1958.

[37] E. H. Brandt and U. Essmann. *phys. stat. sol.(b)*, 13:144, 1987.

[38] D. R. Aston, L. W. Dubeck, and F. Rothwarf. "intermediate mixed" state of type-ii superconductors. *Phys. Rev. B*, 3:2231–2236, Apr 1971.

[39] S. Mühlbauer, C. Pfleiderer, P. Böni, M. Laver, E. M. Forgan, D. Fort, U. Keiderling, and G. Behr. Morphology of the superconducting vortex lattice in ultrapure niobium. *Phys. Rev. Lett.*, 102:136408, Apr 2009.

[40] Ernst Helmut Brandt and Mukunda P. Das. Attractive vortex interaction and the intermediate-mixed state of superconductors. *Journal of Superconductivity and Novel Magnetism*, 24(1):57–67, Jan 2011.

[41] Jeudy, V. and Gourdon, C. Instability-driven formation of domains in the intermediate state of type-i superconductors. *Europhys. Lett.*, 75(3):482–488, 2006.

[42] John R. Clem. Two-dimensional vortices in a stack of thin superconducting films: A model for high-temperature superconducting multilayers. *Phys. Rev. B*, 43:7837–7846, Apr 1991.

[43] S. E. Savel'ev, J. Mirković, and K. Kadowaki. London theory of the crossing vortex lattice in highly anisotropic layered superconductors. *Phys. Rev. B*, 64:094521, Aug 2001.

[44] A. E. Koshelev. Crossing lattices, vortex chains, and angular dependence of melting line in layered superconductors. *Phys. Rev. Lett.*, 83:187–190, Jul 1999.

[45] John R. Clem. Pancake vortices. *Journal of Superconductivity*, 17(5):613–629, Oct 2004.

[46] A. E. Koshelev. Josephson vortices and solitons inside pancake vortex lattice in layered superconductors. *Phys. Rev. B*, 68:094520, Sep 2003.

[47] A. E. Koshelev. Vortex-chain phases in layered superconductors. *Phys. Rev. B*, 71:174507, May 2005.

[48] A. E. Koshelev and M. J. W. Dodgson. Josephson vortex lattice in layered superconductors. *Journal of Experimental and Theoretical Physics*, 117(3):449–479, 2013.

[49] A. V. Samokhvalov, A. S. Mel'nikov, and A. I. Buzdin. Attraction between pancake vortices and vortex molecule formation in the crossing lattices in thin films of layered superconductors. *Phys. Rev. B*, 85:184509, May 2012.

[50] John R. Clem. Theory of magnetically coupled type-ii superconducting films. *Phys. Rev. B*, 9:898–911, Feb 1974.

[51] John R. Clem. Theory of the coupling force in magnetically coupled type-ii superconducting films. *Phys. Rev. B*, 12:1742–1752, Sep 1975.

[52] S.N. Artemenko and A.N. Kruglov. Structure of 2d vortex in a layered high-tc superconductor. *Physics Letters A*, 143(9):485 – 488, 1990.

[53] Buzdin, A. and Feinberg, D. Electromagnetic interaction of vortices in layered superconducting structures. *J. Phys. France*, 51(17):1971–1978, 1990.

[54] M. J. W. Dodgson, A. E. Koshelev, V. B. Geshkenbein, and G. Blatter. Evaporation of the pancake-vortex lattice in weakly coupled layered superconductors. *Phys. Rev. Lett.*, 84:2698–2701, Mar 2000.

[55] A. I. Buzdin, A. S. Mel'nikov, and A. V. Samokhvalov. Vortex molecules in thin films of layered superconductors. *Journal of Superconductivity and Novel Magnetism*, 26(9):2853–2857, 2013.

[56] Bending Simon Tamegai Tsuyoshi Ooi Shuuichi Henini Mohamed Grigorenko, Alexander. A one-dimensional chain state of vortex matter. *Nature.*, 2001.

[57] A. Buzdin and I. Baladié. Attraction between pancake vortices in the crossing lattices of layered superconductors. *Phys. Rev. Lett.*, 88:147002, Mar 2002.

[58] C. A. Bolle, P. L. Gammel, D. G. Grier, C. A. Murray, D. J. Bishop, D. B. Mitzi, and A. Kapitulnik. Observation of a commensurate array of flux chains in tilted flux lattices in bi-sr-ca-cu-o single crystals. *Phys. Rev. Lett.*, 66:112–115, Jan 1991.

[59] P. L. Gammel, D. J. Bishop, J. P. Rice, and D. M. Ginsberg. Images of the vortex chain state in untwinned $YBa_2Cu_3O_{7-\delta}$ crystals. *Phys. Rev. Lett.*, 68:3343–3346, Jun 1992.

[60] T. Tamegai, M. Yasugaki, K. Itaka, N. Kameda, and M. Tokunaga. Magneto-optical observations of vortex states under tilted fields in $Bi_2Sr_2CaCu_2O_{8+y}$. *Physica C: Superconductivity*, 378:416 – 419, 2002.

[61] T. Tamegai, H. Chiku, H. Aoki, and M. Tokunaga. Visualization and control of vortex chains in highly anisotropic superconductors. *Physica C: Superconductivity and its Applications*, 437:314 – 318, 2006. Proceedings of the Fourth International Conference on Vortex Matter in Nanostructured Superconductors VORTEX IV.

[62] T. Tamegai, H. Chiku, and M. Tokunaga. Competition between lensing and dome formation of vortices in $Bi_2Sr_2CaCu_2O_{8+y}$. *Physica C: Superconductivity and its Applications*, 463:245 – 250, 2007. Proceedings of the 19th International Symposium on Superconductivity (ISS 2006).

[63] S.J. Bending, A.N. Grigorenko, I.A. Crisan, D. Cole, A.E. Koshelev, John R. Clem, T. Tamegai, and S. Ooi. Interacting crossing vortex lattices in the presence of quenched disorder. *Physica C: Superconductivity*, 412:372 – 378, 2004. Proceedings of the 16th International Symposium on Superconductivity (ISS 2003). Advances in Superconductivity XVI. Part I.

[64] A. Crisan, S. J. Bending, S. Popa, Z. Z. Li, and H. Raffy. Observation of interacting crossing vortex lattices in bi2sr2cacu2o8+delta thin films. *Physical Review B*, 72, Dec 2005.

[65] A Crisan, S J Bending, and T Tamegai. Manipulation of pancake vortices by rotating a josephson vortex lattice. *Superconductor Science and Technology*, 21(1):015017, 2008.

[66] Yoichi Kamihara, Hidenori Hiramatsu, Masahiro Hirano, Ryuto Kawamura, Hiroshi Yanagi, Toshio Kamiya, and Hideo Hosono. Iron-based layered superconductor:âĂŁ laofep. *Journal of the American Chemical Society*, 128(31):10012–10013, 2006. PMID: 16881620.

[67] Yoichi Kamihara, Takumi Watanabe, Masahiro Hirano, and Hideo Hosono. Iron-based layered superconductor $La_{1-x}FeAs$ (x=0.05-0.12) with T_c = 26 k. *Journal of the American Chemical Society*, 130(11):3296–3297, 2008. PMID: 18293989.

[68] Johnpierre Paglione and Richard L. Greene. High-temperature superconductivity in iron-based materials. *Nat Phys*, 6(9):645–658, Sep 2010.

[69] T.-M. Chuang, M. P. Allan, Jinho Lee, Yang Xie, Ni Ni, S. L. Bud'ko, G. S. Boebinger, P. C. Canfield, and J. C. Davis. Nematic electronic structure in the "parent" state of the iron-based superconductor ca(fe1–xcox)2as2. *Science*, 327(5962):181–184, 2010.

[70] Jiun-Haw Chu, James G. Analytis, Kristiaan De Greve, Peter L. McMahon, Zahirul Islam, Yoshihisa Yamamoto, and Ian R. Fisher. In-plane resistivity anisotropy in an underdoped iron arsenide superconductor. *Science*, 329(5993):824–826, 2010.

[71] A. E. Böhmer, A. Sapkota, A. Kreyssig, S. L. Bud'ko, G. Drachuck, S. M. Saunders, A. I. Goldman, and P. C. Canfield. Effect of biaxial strain on the phase transitions of $CaFe_{1-x}Co_x)_2As_2$. *Phys. Rev. Lett.*, 118:107002, Mar 2017.

[72] A. Fente. *Visualizing the influence of defects and impurities on pnctide and chalcogenide superconductors.* PhD thesis, Universidad Autonoma de Madrid, 2017.

[73] I.I. Mazin and J. Schmalian. Pairing symmetry and pairing state in ferropnictides: Theoretical overview. *Physica C: Superconductivity*, 469(9):614 – 627, 2009. Superconductivity in Iron-Pnictides.

[74] P J Hirschfeld, M M Korshunov, and I I Mazin. Gap symmetry and structure of fe-based superconductors. *Reports on Progress in Physics*, 74(12):124508, 2011.

[75] D.J. Singh. Electronic structure of fe-based superconductors. *Physica C: Superconductivity*, 469(9):418 – 424, 2009. Superconductivity in Iron-Pnictides.

[76] Kazuhiko Kuroki, Hidetomo Usui, Seiichiro Onari, Ryotaro Arita, and Hideo Aoki. Pnictogen height as a possible switch between high-T_c nodeless and low-T_c nodal pairings in the iron-based superconductors. *Phys. Rev. B*, 79:224511, Jun 2009.

[77] I. I. Mazin, D. J. Singh, M. D. Johannes, and M. H. Du. Unconventional superconductivity with a sign reversal in the order parameter of lafeaso$_{1-x}$f$_x$. *Phys. Rev. Lett.*, 101:057003, Jul 2008.

[78] Fengjie Ma, Wei Ji, Jiangping Hu, Zhong-Yi Lu, and Tao Xiang. First-principles calculations of the electronic structure of tetragonal α-fete and α-fese crystals:

Evidence for a bicollinear antiferromagnetic order. *Phys. Rev. Lett.*, 102:177003, Apr 2009.

[79] Shiliang Li, Clarina de la Cruz, Q. Huang, Y. Chen, J. W. Lynn, Jiangping Hu, Yi-Lin Huang, Fong-Chi Hsu, Kuo-Wei Yeh, Maw-Kuen Wu, and Pengcheng Dai. First-order magnetic and structural phase transitions in $Fe_{1+y}Se_xTe_{1-x}$. *Phys. Rev. B*, 79:054503, Feb 2009.

[80] Chang-Youn Moon and Hyoung Joon Choi. Chalcogen-height dependent magnetic interactions and magnetic order switching in $FeSe_xTe_{1-x}$. *Phys. Rev. Lett.*, 104:057003, Feb 2010.

[81] Peter J. Hirschfeld. Using gap symmetry and structure to reveal the pairing mechanism in fe-based superconductors. *Comptes Rendus Physique*, 17(1):197 – 231, 2016. Iron-based superconductors / Supraconducteurs a base de fer.

[82] V. Mourik, K. Zuo, S. M. Frolov, S. R. Plissard, E. P. A. M. Bakkers, and L. P. Kouwenhoven. Signatures of majorana fermions in hybrid superconductor-semiconductor nanowire devices. *Science*, 336(6084):1003–1007, 2012.

[83] Stevan Nadj-Perge, Ilya K. Drozdov, Li Jian, Hua Chen, Sangjun Jeon, Jungpil Seo, Allan H. MacDonald, B. Andrei Bernevig, and Ali Yazdani. Observation of majorana fermions in ferromagnetic atomic chains on a superconductor. *Science*, 346(6209):602–607, 2014.

[84] N. B. Kopnin, I. M. Khaymovich, and A. S. Mel'nikov. Vortex matter in low-dimensional systems with proximity-induced superconductivity. *Journal of Experimental and Theoretical Physics*, 117(3):418–438, Sep 2013.

[85] P. R. Wallace. The band theory of graphite. *Phys. Rev.*, 71:622–634, May 1947.

[86] K. S. Novoselov, A. K. Geim, S. V. Morozov, D. Jiang, M. I. Katsnelson, I. V. Grigorieva, S. V. Dubonos, and A. A. Firsov. Two-dimensional gas of massless dirac fermions in graphene. *Nature*, 438:197 EP –, Nov 2005.

[87] Yuanbo Zhang, Yan-Wen Tan, Horst L. Stormer, and Philip Kim. Experimental observation of the quantum hall effect and berry phase in graphene. *Nature*, 438:201 EP –, Nov 2005.

[88] B. Partoens and F. M. Peeters. From graphene to graphite: Electronic structure around the k point. *Phys. Rev. B*, 74:075404, Aug 2006.

[89] S. Das Sarma, Shaffique Adam, E. H. Hwang, and Enrico Rossi. Electronic transport in two-dimensional graphene. *Rev. Mod. Phys.*, 83:407–470, May 2011.

[90] N. B. Kopnin and E. B. Sonin. Bcs superconductivity of dirac electrons in graphene layers. *Phys. Rev. Lett.*, 100:246808, Jun 2008.

[91] Bruno Uchoa and A. H. Castro Neto. Superconducting states of pure and doped graphene. *Phys. Rev. Lett.*, 98:146801, Apr 2007.

[92] J. P. L. Faye, P. Sahebsara, and D. Sénéchal. Chiral triplet superconductivity on the graphene lattice. *Phys. Rev. B*, 92:085121, Aug 2015.

[93] Maximilian L. Kiesel, Christian Platt, Werner Hanke, Dmitry A. Abanin, and Ronny Thomale. Competing many-body instabilities and unconventional superconductivity in graphene. *Phys. Rev. B*, 86:020507, Jul 2012.

[94] Rahul Nandkishore, Ronny Thomale, and Andrey V. Chubukov. Superconductivity from weak repulsion in hexagonal lattice systems. *Phys. Rev. B*, 89:144501, Apr 2014.

[95] J. González. Kohn-luttinger superconductivity in graphene. *Phys. Rev. B*, 78:205431, Nov 2008.

[96] Rahul Nandkishore, L. S. Levitov, and A. V. Chubukov. Chiral superconductivity from repulsive interactions in doped graphene. *Nature Physics*, 8:158 EP –, Jan 2012. Article.

[97] Annica M. Black-Schaffer and Sebastian Doniach. Possibility of measuring intrinsic electronic correlations in graphene using a d-wave contact josephson junction. *Phys. Rev. B*, 81:014517, Jan 2010.

[98] Mir Vahid Hosseini and Malek Zareyan. Model of an exotic chiral superconducting phase in a graphene bilayer. *Phys. Rev. Lett.*, 108:147001, Apr 2012.

[99] Valeri N. Kotov, Bruno Uchoa, Vitor M. Pereira, F. Guinea, and A. H. Castro Neto. Electron-electron interactions in graphene: Current status and perspectives. *Rev. Mod. Phys.*, 84:1067–1125, Jul 2012.

[100] B. M. Ludbrook, G. Levy, P. Nigge, M. Zonno, M. Schneider, D. J. Dvorak, C. N. Veenstra, S. Zhdanovich, D. Wong, P. Dosanjh, C. Straβer, A. StÃűhr, S. Forti, C. R. Ast, U. Starke, and A. Damascelli. Evidence for superconductivity in li-decorated monolayer graphene. *Proceedings of the National Academy of Sciences*, 112(38):11795–11799, 2015.

[101] J. Chapman, Y. Su, C. A. Howard, D. Kundys, A. N. Grigorenko, F. Guinea, A. K. Geim, I. V. Grigorieva, and R. R. Nair. Superconductivity in ca-doped graphene laminates. *Scientific Reports*, Mar 2016.

[102] C. Tonnoir, A. Kimouche, J. Coraux, L. Magaud, B. Delsol, B. Gilles, and C. Chapelier. Induced superconductivity in graphene grown on rhenium. *Phys. Rev. Lett.*, 111:246805, Dec 2013.

[103] Jacob Linder, Annica M. Black-Schaffer, Takehito Yokoyama, Sebastian Doniach, and Asle Sudbø. Josephson current in graphene: Role of unconventional pairing symmetries. *Phys. Rev. B*, 80:094522, Sep 2009.

[104] P. A. Khomyakov, G. Giovannetti, P. C. Rusu, G. Brocks, J. van den Brink, and P. J. Kelly. First-principles study of the interaction and charge transfer between graphene and metals. *Phys. Rev. B*, 79:195425, May 2009.

[105] J. Wintterlin and M.-L. Bocquet. Graphene on metal surfaces. *Surface Science*, 603(10):1841 – 1852, 2009. Special Issue of Surface Science dedicated to Prof. Dr. Dr. h.c. mult. Gerhard Ertl, Nobel-Laureate in Chemistry 2007.

[106] Straver Eric W. J. Hoffman Jennifer E Koshnick Nicholas C. Zeldov Eli Bonn Douglas A. Liang Ruixing Hardy Walter N. Auslaender Ophir M, Luan Lan and Moler Kathryn A. Mechanics of individual isolated vortices in a cuprate superconductor ja - nat phys. *Nat Phys*, 5(1):39, 2009.

[107] Anna Kremen, Shai Wissberg, Noam Haham, Eylon Persky, Yiftach Frenkel, and Beena Kalisky. Mechanical control of individual superconducting vortices. *Nano Lett*, 16(3):1626–1630, Mar 2016. 26836018[pmid].

[108] I. S. Veshchunov, W. Magrini, S. V. Mironov, A. G. Godin, J.-B. Trebbia, A. I. Buzdin, Ph Tamarat, and B. Lounis. Optical manipulation of single flux quanta. 7:12801 EP –, Sep 2016. Article.

[109] E. W. J. Straver, J. E. Hoffman, O. M. Auslaender, D. Rugar, and Kathryn A. Moler. Controlled manipulation of individual vortices in a superconductor. *Applied Physics Letters*, 93(17):–, 2008.

[110] Pengcheng Dai, Jiangping Hu, and Elbio Dagotto. Magnetism and its microscopic origin in iron-based high-temperature superconductors. *Nat Phys*, 8(10):709–718, Oct 2012.

[111] A. A. Kordyuk. Iron-based superconductors: Magnetism, superconductivity, and electronic structure (review article). *Low Temperature Physics*, 38(9):888–899, 2012.

[112] Jinsheng Wen, Guangyong Xu, Genda Gu, J M Tranquada, and R J Birgeneau. Interplay between magnetism and superconductivity in iron-chalcogenide superconductors: crystal growth and characterizations. *Reports on Progress in Physics*, 74(12):124503, 2011.

[113] E. W. J. Straver, J. E. Hoffman, O. M. Auslaender, D. Rugar, and Kathryn A. Moler. Controlled manipulation of individual vortices in a superconductor. *Applied Physics Letters*, 93(17):172514, 2008.

[114] J. A. Galvis, E. Herrera, I. Guillamon, J. Azpeitia, R. F. Luccas, C. Munuera, M. Cuenca, J. A. Higuera, N. DÃŋaz, M. Pazos, M. Garcia-Hernandez, A. BuendÃŋa, S. Vieira, and H. Suderow. Three axis vector magnet set-up for cryogenic scanning probe microscopy. *Review of Scientific Instruments*, 86(1):–, 2015.

[115] Peng Pan, Feiyu Yang, Zhenhua Wang, Bowen Zhong, Lining Sun, and Changhai Ru. *A Review of Stick–Slip Nanopositioning Actuators*, pages 1–32. Springer International Publishing, Cham, 2016.

[116] D. Rugar, H. J. Mamin, and P. Guethner. Improved fiber-optic interferometer for atomic force microscopy. *Applied Physics Letters*, 55(25):2588–2590, 1989.

[117] D. Rugar, H. J. Mamin, R. Erlandsson, J. E. Stern, and B. D. Terris. Force microscope using a fiber optic displacement sensor. *Review of Scientific Instruments*, 59(11):2337–2340, 1988.

[118] A Moser, H J Hug, T Jung, U D Schwarz, and H J Guntherodt. A miniature fibre optic force microscope scan head. *Measurement Science and Technology*, 4(7):769, 1993.

[119] Ozgur Karci. *Design of a self alinged, high resolution, low temperature (30 mK - 300 K) magnetic force microscope.* PhD thesis, Institute of Sciences of Hacettepe University, 2014.

[120] Bennewitz Roland Meyer Ernst, Hug Hans Josef. *Scanning Probe Microscopy : the Lab on a Tip.* Academic Press, 2004.

[121] Rubén Pérez, Ivan Štich, Michael C. Payne, and Kiyoyuki Terakura. Surface-tip interactions in noncontact atomic-force microscopy on reactive surfaces: Si(111). *Phys. Rev. B*, 58:10835–10849, Oct 1998.

[122] M. Jaafar. *Procesos de imanacion en la nanoescala mediante microscopia de fuerzas magneticas.* PhD thesis, Universidad Autonoma de Madrid, 2009.

[123] Jian-Gang (Jimmy) Zhu. New heights for hard disk drives. *Materials Today*, 6(7):22 – 31, 2003.

[124] Livia Angeloni, Daniele Passeri, Melania Reggente, Diego Mantovani, and Marco Rossi. Removal of electrostatic artifacts in magnetic force microscopy by controlled magnetization of the tip: application to superparamagnetic nanoparticles. 6:26293 EP –, May 2016. Article.

[125] H. Li, Y. Wang, S. Wang, H. Zhong, and D. Wei. Micromagnetic analysis of effective magnetic dipole position in magnetic force microscope tip. *IEEE Transactions on Magnetics*, 46(7):2570–2578, July 2010.

[126] Oscar Iglesias-Freire, Jeffrey R. Bates, Yoichi Miyahara, Agustina Asenjo, and Peter H. Grutter. Tip-induced artifacts in magnetic force microscopy images. *Applied Physics Letters*, 102(2):022417, 2013.

[127] Alexander Alekseev, Anatoliy Popkov, Andrey Shubin, Feodor Pudonin, and Nikolay Djuzhev. Effect of horizontal magnetization reversal of the tips on magnetic force microscopy images. *Ultramicroscopy*, 136:91 – 95, 2014.

[128] J R Kirtley. Fundamental studies of superconductors using scanning magnetic imaging. *Reports on Progress in Physics*, 73(12):126501, 2010.

[129] P.C Canfield. *Solution Growth of Intermetallic Single Crystals: A beguinner guide*. Book series on COmplex Metallic Alloys. World Scientific, 2010.

[130] P. C. Canfield and Z. Fisk. *Phil. Mag.*, B 65:1117, 1992.

[131] P. C. Canfield. *Solution growth of intermetallic single crystals: a beginner's guide*, chap 2:93, 2009.

[132] H. Okamoto. *J. of Phase Equilibria*, B 65:1117, 1994.

[133] J. Rodriguez-Carvaja. *Physica B*, 55:192, 1993.

[134] N. N. Zhuravlev. *Zh. Eksp. Teor. Fiz*, 5:1064, 1957.

[135] K. S. Novoselov, A. K. Geim, S. V. Morozov, D. Jiang, Y. Zhang, S. V. Dubonos, I. V. Grigorieva, and A. A. Firsov. Electric field effect in atomically thin carbon films. *Science*, 306(5696):666–669, 2004.

[136] K. S. Novoselov, D. Jiang, F. Schedin, T. J. Booth, V. V. Khotkevich, S. V. Morozov, and A. K. Geim. Two-dimensional atomic crystals. *Proceedings of the National Academy of Sciences of the United States of America*, 102(30):10451–10453, 2005.

[137] Matthew A. Meitl, Zheng-Tao Zhu, Vipan Kumar, Keon Jae Lee, Xue Feng, Yonggang Y. Huang, Ilesanmi Adesida, Ralph G. Nuzzo, and John A. Rogers. Transfer printing by kinetic control of adhesion to an elastomeric stamp. *Nat Mater*, 5(1):33–38, Jan 2006.

[138] Andres Castellanos-Gomez, Magdalena Wojtaszek, Nikolaos Tombros, Nicolas Agrait, Bart J. van Wees, and Gabino Rubio-Bollinger. Atomically thin mica flakes and their application as ultrathin insulating substrates for graphene. *Small*, 7(17):2491–2497, 2011.

[139] E. Pinilla. *Characterization and processability of molecular-based magnetic nanoparticles and 2D crystals by scanning probe microscopy.* PhD thesis, Universidad Autonoma de Madrid, 2013.

[140] J. Pearl. Current distribution in superconducting films carrying quantized fluxoids. *Applied Physics Letters*, 5(4):65–66, 1964.

[141] Judea Pearl. Structure of superconductive vortices near a metal-air interface. *Journal of Applied Physics*, 37(11):4139–4141, 1966.

[142] Ernst Helmut Brandt. Vortex-vortex interaction in thin superconducting films. *Phys. Rev. B*, 79:134526, Apr 2009.

[143] R. Prozorov, R. W. Giannetta, A. Carrington, P. Fournier, R. L. Greene, P. Guptasarma, D. G. Hinks, and A. R. Banks. Measurements of the absolute value of the penetration depth in high-tc superconductors using a low-tc superconductive coating. *Applied Physics Letters*, 77(25):4202–4204, 2000.

[144] S. L. Lee, P. Zimmermann, H. Keller, M. Warden, I. M. Savić, R. Schauwecker, D. Zech, R. Cubitt, E. M. Forgan, P. H. Kes, T. W. Li, A. A. Menovsky, and Z. Tarnawski. Evidence for flux-lattice melting and a dimensional crossover in single-crystal $Bi_{2.15}Sr_{1.85}CaCu_2O_{8+\delta}$ from muon spin rotation studies. *Phys. Rev. Lett.*, 71:3862–3865, Dec 1993.

[145] V. G. Kogan, M. Ledvij, A. Yu. Simonov, J. H. Cho, and D. C. Johnston. Role of vortex fluctuations in determining superconducting parameters from magnetization data for layered superconductors. *Phys. Rev. Lett.*, 70:1870–1873, Mar 1993.

[146] I. R. Shein and A. L. Ivanovskii. Electronic band structure and fermi surface of tetragonal low-temperature superconductor bi2pd as predicted from first principles. *Journal of Superconductivity and Novel Magnetism*, 26(1):1–4, 2013.

[147] Diana Berman, Ali Erdemir, and Anirudha V. Sumant. Graphene: a new emerging lubricant. *Materials Today*, 17(1):31 – 42, 2014.

[148] Suzhi Li, Qunyang Li, Robert W. Carpick, Peter Gumbsch, Xin Z. Liu, Xiangdong Ding, Jun Sun, and Ju Li. The evolving quality of frictional contact with graphene. *Nature*, 539(7630):541–545, Nov 2016. Letter.

[149] U. Essman y H. Traublel. *Physics Letters A*, 526:24, 1967.

[150] P. L. Gammel, D. J. Bishop, G. J. Dolan, J. R. Kwo, C. A. Murray, L. F. Schneemeyer, and J. V. Waszczak. Observation of hexagonally correlated flux quanta in $YBa_2Cu_3O_7$. *Phys. Rev. Lett.*, 59:2592–2595, Nov 1987.

[151] A. Moser, H. J. Hug, I. Parashikov, B. Stiefel, O. Fritz, H. Thomas, A. Baratoff, H.-J. Güntherodt, and P. Chaudhari. Observation of single vortices condensed into a vortex-glass phase by magnetic force microscopy. *Phys. Rev. Lett.*, 74:1847–1850, Mar 1995.

[152] E. H. Brandt and U. Essmann. *Phys. Rev. B*, 2231:3, 1971.

[153] Ruslan Prozorov. Equilibrium topology of the intermediate state in type-i superconductors of different shapes. *Phys. Rev. Lett.*, 98:257001, Jun 2007.

[154] C. P. Bean and J. D. Livingston. Surface barrier in type-ii superconductors. *Phys. Rev. Lett.*, 12:14–16, Jan 1964.

[155] Maamar Benkraouda and John R. Clem. Critical current from surface barriers in type-ii superconducting strips. *Phys. Rev. B*, 58:15103–15107, Dec 1998.

[156] T. Reimann, S. Mühlbauer, M. Schulz, B. Betz, A. Kaestner, V. Pipich, P. Böni, and C. Grünzweig. Visualizing the morphology of vortex lattice domains in a bulk type-ii superconductor. 6:8813 EP –, Nov 2015. Article.

[157] U. Essmann. Intermediate state of superconducting niobium. *Physics Letters A*, 41(5):477 – 478, 1972.

[158] Guillamon et al. *Phys. Rev. B*, 134505:77, 2008.

[159] F. Giubileo, D. Roditchev, W. Sacks, R. Lamy, D. X. Thanh, J. Klein, S. Miraglia, D. Fruchart, J. Marcus, and Ph. Monod. Two-gap state density in mgb_2: A true bulk property or a proximity effect? *Phys. Rev. Lett.*, 87:177008, Oct 2001.

[160] A. S. Sidorenko, L. R. Tagirov, A. N. Rossolenko, V. V. Ryazanov, M. Klemm, and R. Tidecks. Evidence for two-dimensional nucleation of superconductivity in mgb 2. *EPL (Europhysics Letters)*, 59(2):272, 2002.

[161] A D Caplin, Y Bugoslavsky, L F Cohen, L Cowey, J Driscoll, J Moore, and G K Perkins. Critical fields and critical currents in mgb 2. *Superconductor Science and Technology*, 16(2):176, 2003.

[162] M. Marchevsky, P.H. Kes, and J. Aarts. Determination of the quenching temperature for the vortex lattice in field-cooling decoration experiments. *Physica C: Superconductivity and its Applications*, 282:2083 – 2084, 1997.

[163] Egor Babaev and Martin Speight. Semi-meissner state and neither type-i nor type-ii superconductivity in multicomponent superconductors. *Phys. Rev. B*, 72:180502, Nov 2005.

[164] Yoshinori Imai, Fuyuki Nabeshima, Taiki Yoshinaka, Kosuke Miyatani, Ryusuke Kondo, Seiki Komiya, Ichiro Tsukada, and Atsutaka Maeda. Superconductivity at 5.4 k in β-bi2pd. *Journal of the Physical Society of Japan*, 81(11):113708, 2012.

[165] Hyoung Joon Choi, David Roundy, Hong Sun, Marvin L. Cohen, and Steven G. Louie. The origin of the anomalous superconducting properties of mgb2. *Nature*, 418(6899):758–760, Aug 2002.

[166] Y. Nakajima, T. Nakagawa, T. Tamegai, and H. Harima. Specific-heat evidence for two-gap superconductivity in the ternary-iron silicide $Lu_2Fe_3Si_5$. *Phys. Rev. Lett.*, 100:157001, Apr 2008.

[167] D. F. Agterberg, T. M. Rice, and M. Sigrist. Orbital dependent superconductivity in Sr_2RuO_4. *Phys. Rev. Lett.*, 78:3374–3377, Apr 1997.

[168] S. V. Shulga, S.-L. Drechsler, G. Fuchs, K.-H. Müller, K. Winzer, M. Heinecke, and K. Krug. Upper critical field peculiarities of superconducting YNi_2B_2C and $LuNi_2B_2C$. *Phys. Rev. Lett.*, 80:1730–1733, Feb 1998.

[169] T. Dahm and N. Schopohl. Fermi surface topology and the upper critical field in two-band superconductors: Application to MgB_2. *Phys. Rev. Lett.*, 91:017001, Jul 2003.

[170] A. Gurevich. Enhancement of the upper critical field by nonmagnetic impurities in dirty two-gap superconductors. *Phys. Rev. B*, 67:184515, May 2003.

[171] V. G. Tissen, M. R. Osorio, J. P. Brison, N. M. Nemes, M. García-Hernández, L. Cario, P. Rodière, S. Vieira, and H. Suderow. Pressure dependence of superconducting critical temperature and upper critical field of $2H-NbS_2$. *Phys. Rev. B*, 87:134502, Apr 2013.

[172] Paul F. Sullivan and G. Seidel. Steady-state, ac-temperature calorimetry. *Phys. Rev.*, 173:679–685, Sep 1968.

[173] J. Kačmarčík, Z. Pribulová, V. Pal'uchová, P. Szabó, P. Husaníková, G. Karapetrov, and P. Samuely. Heat capacity of single-crystal cu_xtise_2 superconductors. *Phys. Rev. B*, 88:020507, Jul 2013.

[174] Yan-Feng Lv, Wen-Lin Wang, Yi-Min Zhang, Hao Ding, Wei Li, Lili Wang, Ke He, Can-Li Song, Xu-Cun Ma, and Qi-Kun Xue. Experimental signature of topological superconductivity and majorana zero modes on $\beta-bi_2pd$ thin films. *Science Bulletin*, 62(12):852 – 856, 2017.

[175] C. Caroli, P.G. De Gennes, and J. Matricon. Bound fermion states on a vortex line in a type ii superconductor. *Physics Letters*, 9(4):307 – 309, 1964.

[176] H. F. Hess, R. B. Robinson, and J. V. Waszczak. Vortex-core structure observed with a scanning tunneling microscope. *Phys. Rev. Lett.*, 64:2711–2714, May 1990.

[177] M. Kanou H. Sanjo T. Okuda T. Sasagawa M. Sakano, K. Okawa and K Ishizakaa. Topologically protected surface states in a centrosymmetric superconductor $\beta-pdbi_2$. *Nature Communications*, 6:8595, 2015.

[178] K. Iwaya, Y. Kohsaka, K. Okawa, T. Machida, M. S. Bahramy, T. Hanaguri, and T. Sasagawa. Full-gap superconductivity in spin-polarised surface states of topological semimetal $\beta-pdbi_2$. *Nature Communications*, 8(1):976, 2017.

[179] Lu Hua Li and Ying Chen. Electric contributions to magnetic force microscopy response from graphene and MoS_2 nanosheets. *Journal of Applied Physics*, 116(21):213904, 2014.

[180] Yonathan Anahory, Jonathan Reiner, Lior Embon, Dorri Halbertal, Anton Yakovenko, Yuri Myasoedov, Michael L. Rappaport, Martin E. Huber, and

Eli Zeldov. Three-junction squid-on-tip with tunable in-plane and out-of-plane magnetic field sensitivity. *Nano Letters*, 14(11):6481–6487, 2014. PMID: 25310273.

[181] R. Labusch. Elasticity effects in type-ii superconductors. *Phys. Rev.*, 170:470–474, Jun 1968.

[182] Tom H Johansen. Flux-pinning-induced stress and magnetostriction in bulk superconductors. *Superconductor Science and Technology*, 13(10):R121, 2000.

[183] Shi-Zeng Lin and Vladimir G. Kogan. Strain-induced intervortex interaction and vortex lattices in tetragonal superconductors. *Phys. Rev. B*, 95:054511, Feb 2017.

[184] V. G. Kogan, L. N. Bulaevskii, P. Miranović, and L. Dobrosavljević-Grujić. Vortex-induced strain and flux lattices in anisotropic superconductors. *Phys. Rev. B*, 51:15344–15350, Jun 1995.

[185] V. G. Kogan. Vortex-induced strain and magnetization in type-ii superconductors. *Phys. Rev. B*, 87:020503, Jan 2013.

[186] A. Cano, A. P. Levanyuk, and S. A. Minyukov. Elasticity-driven interaction between vortices in type-ii superconductors. *Phys. Rev. B*, 68:144515, Oct 2003.

[187] G. Pristas et al. Pressure effect on superconducting and normal state of β-bi$_2$pd. *Phys. Rev. B*, 97:01234, 2017.

[188] R. Kossowsky, S. Bose, Z. Durusoy, and V. Pan. *Physics and Materials Science of Vortex States, Flux Pinning and Dynamics.* NATO Advanced Study Institutes series. Series E, Applied sciences. Springer, 1999.

[189] A. Fente, E. Herrera, I. Guillamón, H. Suderow, S. Mañas Valero, M. Galbiati, E. Coronado, and V. G. Kogan. Field dependence of the vortex core size probed by scanning tunneling microscopy. *Phys. Rev. B*, 94:014517, Jul 2016.

[190] A Schwarz, M Liebmann, U H Pi, and R Wiesendanger. Real space visualization of thermal fluctuations in a triangular flux-line lattice. *New Journal of Physics*, 12(3):033022, 2010.

[191] David Dodoo-Arhin, Mopeli Fabiane, Abdulhakeem Bello, and Ncholu Manyala. Graphene: Synthesis, transfer, and characterization for dye-sensitized solar cells applications. *Industrial & Engineering Chemistry Research*, 52(39):14160–14168, 2013.

[192] J. Azpeitia. PhD thesis, Universidad Autonoma de Madrid, 2018.

[193] J. Azpeitia, G. Otero-Irurueta, I. Palacio, J.I. Martinez, N. Ruiz del Arbol, G. Santoro, A. Gutierrez, L. Aballe, M. Foerster, M. Kalbac, V. Vales, F.J. Mompean, M. Garcia-Hernandez, J.A. Martin-Gago, C. Munuera, and M.F. Lopez. High-quality pvd graphene growth by fullerene decomposition on cu foils. *Carbon*, 119(Supplement C):535 – 543, 2017.

[194] Yu Wang, Yi Zheng, Xiangfan Xu, Emilie Dubuisson, Qiaoliang Bao, Jiong Lu, and Kian Ping Loh. Electrochemical delamination of cvd-grown graphene film: Toward the recyclable use of copper catalyst. *ACS Nano*, 5(12):9927–9933, 2011. PMID: 22034835.

[195] Tymoteusz Ciuk, Iwona Pasternak, Aleksandra Krajewska, Jan Sobieski, Piotr Caban, Jan Szmidt, and Wlodek Strupinski. Properties of chemical vapor deposition graphene transferred by high-speed electrochemical delamination. *The Journal of Physical Chemistry C*, 117(40):20833–20837, 2013.

[196] Yasutomo J Uemura. Superconductivity: Commonalities in phase and mode. *Nature Materials*, 8:253–255, 2009.

[197] E. P. Stillwell, M. J. Skove, and J. H. Davis. Two "whisker" straining devices suitable for low temperatures. *Review of Scientific Instruments*, 39(2):155–157, 1968.

[198] D. R. Overcash, M. J. Skove, and E. P. Stillwell. Effect of elastic stress on some electronic properties of indium. *Phys. Rev.*, 187:570–574, Nov 1969.

[199] M A Angadi, D E Britton, and E Fawcett. Low temperature sample holder for rotating a crystal under tension in a superconducting solenoid. *Journal of Physics E: Scientific Instruments*, 6(11):1086, 1973.

[200] M. Shayegan, K. Karrai, Y. P. Shkolnikov, K. Vakili, E. P. De Poortere, and S. Manus. Low-temperature, in situ tunable, uniaxial stress measurements

in semiconductors using a piezoelectric actuator. *Applied Physics Letters*, 83(25):5235–5237, 2003.

[201] Jiun-Haw Chu, Hsueh-Hui Kuo, James G. Analytis, and Ian R. Fisher. Divergent nematic susceptibility in an iron arsenide superconductor. *Science*, 337(6095):710–712, 2012.

[202] Hsueh-Hui Kuo, Maxwell C. Shapiro, Scott C. Riggs, and Ian R. Fisher. Measurement of the elastoresistivity coefficients of the underdoped iron arsenide ba$(\mathrm{fe}_{0.975}\mathrm{co}_{0.025})_2\mathrm{as}_2$. *Phys. Rev. B*, 88:085113, Aug 2013.

[203] Hsueh-Hui Kuo, Jiun-Haw Chu, Johanna C. Palmstrom, Steven A. Kivelson, and Ian R. Fisher. Ubiquitous signatures of nematic quantum criticality in optimally doped fe-based superconductors. *Science*, 352(6288):958–962, 2016.

[204] M. C. Shapiro, Patrik Hlobil, A. T. Hristov, Akash V. Maharaj, and I. R. Fisher. Symmetry constraints on the elastoresistivity tensor. *Phys. Rev. B*, 92:235147, Dec 2015.

[205] Michael Merz, Peter Schweiss, Peter Nagel, Meng-Jie Huang, Robert Eder, Thomas Wolf, Hilbert von Lohneysen, and Stefan Schuppler. Of substitution and doping: Spatial and electronic structure in fe pnictides. *Journal of the Physical Society of Japan*, 85(4):044707, 2016.

[206] Athena S Sefat. Pressure effects on two superconducting iron-based families. *Reports on Progress in Physics*, 74(12):124502, 2011.

[207] Igawa Kazumi Arii Kazunobu Kamihara Yoichi Hirano Masahiro Hosono Hideo Takahashi, Hiroki. Superconductivity at 43 k in an iron-based layered compound $lao_{1-x}f_xfeas$. *Nature*, 453:376–378, May 2015.

[208] K. Iida, J. Hanisch, R. Huhne, F. Kurth, M. Kidszun, S. Haindl, J. Werner, L. Schultz, and B. Holzapfel. Strong tc dependence for strained epitaxial ba$(\mathrm{fe}1-x\mathrm{co}x)_2\mathrm{as}_2$ thin films. *Applied Physics Letters*, 95(19):192501, 2009.

[209] P. Chekhonin W. Skrotzki D.V. Efremov S. Oswald K. Iida R. Huhne J. Hanisch M. Hoffmann F. Kurth L. Schultz J. Engelmann, V. Grinenko and B. Holzapfell. Strain induced superconductivity in the parent compound $BaFe_2As_2$. *Nature Communications*, 4(2877), 2013.

[210] M. S. Torikachvili, S. L. Bud'ko, N. Ni, P. C. Canfield, and S. T. Hannahs. Effect of pressure on transport and magnetotransport properties in cafe$_2$as$_2$ single crystals. *Phys. Rev. B*, 80:014521, Jul 2009.

[211] K. Prokeš, A. Kreyssig, B. Ouladdiaf, D. K. Pratt, N. Ni, S. L. Bud'ko, P. C. Canfield, R. J. McQueeney, D. N. Argyriou, and A. I. Goldman. Evidence from neutron diffraction for superconductivity in the stabilized tetragonal phase of $CaFe_2As_2$ under uniaxial pressure. *Phys. Rev. B*, 81:180506, May 2010.

[212] S. L. Budko, N. Ni, S. Nandi, G. M. Schmiedeshoff, and P. C. Canfield. Thermal expansion and anisotropic pressure derivatives of T_c in Ba(Fe$_{1-x}$Co$_x$)$_2$as$_2$ single crystals. *Phys. Rev. B*, 79:054525, Feb 2009.

[213] Takehiro Yamazaki, Nao Takeshita, Ryosuke Kobayashi, Hideto Fukazawa, Yoh Kohori, Kunihiro Kihou, Chul-Ho Lee, Hijiri Kito, Akira Iyo, and Hiroshi Eisaki. Appearance of pressure-induced superconductivity in $BaFe_2As_2$ under hydrostatic conditions and its extremely high sensitivity to uniaxial stress. *Phys. Rev. B*, 81:224511, Jun 2010.

[214] M. A. Tanatar, E. C. Blomberg, A. Kreyssig, M. G. Kim, N. Ni, A. Thaler, S. L. Bud'ko, P. C. Canfield, A. I. Goldman, I. I. Mazin, and R. Prozorov. Uniaxial-strain mechanical detwinning of $CaFe_2As_2$ and crystals: Optical and transport study. *Phys. Rev. B*, 81:184508, May 2010.

[215] Christoph Meingast, Frédéric Hardy, Rolf Heid, Peter Adelmann, Anna Böhmer, Philipp Burger, Doris Ernst, Rainer Fromknecht, Peter Schweiss, and Thomas Wolf. Thermal expansion and grüneisen parameters of Ba(fe$_{1-x}$co$_x$)$_2$as$_2$: A thermodynamic quest for quantum criticality. *Phys. Rev. Lett.*, 108:177004, Apr 2012.

[216] W. Yu, A. A. Aczel, T. J. Williams, S. L. Bud'ko, N. Ni, P. C. Canfield, and G. M. Luke. Absence of superconductivity in single-phase $CaFe_2As_2$ under hydrostatic pressure. *Phys. Rev. B*, 79:020511, Jan 2009.

[217] R. Mittal, S. K. Mishra, S. L. Chaplot, S. V. Ovsyannikov, E. Greenberg, D. M. Trots, L. Dubrovinsky, Y. Su, Th. Brueckel, S. Matsuishi, H. Hosono, and G. Garbarino. Ambient- and low-temperature synchrotron x-ray diffraction

study of bafe$_2$as$_2$ and cafe$_2$as$_2$ at high pressures up to 56 gpa. *Phys. Rev. B*, 83:054503, Feb 2011.

[218] S. Ran, S. L. Bud'ko, D. K. Pratt, A. Kreyssig, M. G. Kim, M. J. Kramer, D. H. Ryan, W. N. Rowan-Weetaluktuk, Y. Furukawa, B. Roy, A. I. Goldman, and P. C. Canfield. Stabilization of an ambient-pressure collapsed tetragonal phase in cafe$_2$as$_2$ and tuning of the orthorhombic-antiferromagnetic transition temperature by over 70 k via control of nanoscale precipitates. *Phys. Rev. B*, 83:144517, Apr 2011.

[219] S. Ran. *Combined effects of post-growth thermal treatment and chemical substitution on physical properties of* $CaFe_2As_2$. PhD thesis, Iowa State University, 2014.

[220] M. A. Tanatar, A. Kreyssig, S. Nandi, N. Ni, S. L. Bud'ko, P. C. Canfield, A. I. Goldman, and R. Prozorov. Direct imaging of the structural domains in the iron pnictides AFe_2As_2 ($a = \mathrm{Ca, Sr, Ba}$). *Phys. Rev. B*, 79:180508, May 2009.

[221] S. Ran, S. L. Bud'ko, W. E. Straszheim, J. Soh, M. G. Kim, A. Kreyssig, A. I. Goldman, and P. C. Canfield. Control of magnetic, nonmagnetic, and superconducting states in annealed $Ca(Fe_{1-x}Co_x)_2As_2$. *Phys. Rev. B*, 85:224528, Jun 2012.

[222] E. Gati, S. Köhler, D. Guterding, B. Wolf, S. Knöner, S. Ran, S. L. Bud'ko, P. C. Canfield, and M. Lang. Hydrostatic-pressure tuning of magnetic, nonmagnetic, and superconducting states in annealed ca(fe$_{1-x}$co$_x$)$_2$as$_2$. *Phys. Rev. B*, 86:220511, Dec 2012.

[223] H. Suderow, I. Guillamon, and S. Vieira. Compact very low temperature scanning tunneling microscope with mechanically driven horizontal linear positioning stage. *Review of Scientific Instruments*, 82(3):033711, 2011.

[224] A. Alberca, C. Munuera, J. Tornos, F. J. Mompean, N. Biskup, A. Ruiz, N. M. Nemes, A. de Andres, C. León, J. Santamaría, and M. García-Hernández. Ferroelectric substrate effects on the magnetism, magnetotransport, and electroresistance of la$_{0.7}$ca$_{0.3}$mno$_3$ thin films on batio$_3$. *Phys. Rev. B*, 86:144416, Oct 2012.

[225] Juan de la Figuera, Zbynek Novotny, Martin Setvin, Tijiang Liu, Zhiqiang Mao, Gong Chen, Alpha T. N'Diaye, Michael Schmid, Ulrike Diebold, Andreas K. Schmid, and Gareth S. Parkinson. Real-space imaging of the verwey transition at the (100) surface of magnetite. *Phys. Rev. B*, 88:161410, Oct 2013.

[226] G. Shirane. *Ferroelectric Crystals*. International Series of Monographs on Solid State Physics. Pergamon Press, 1996.

[227] Miao Gao, Fengjie Ma, Zhong-Yi Lu, and Tao Xiang. Surface structures of ternary iron arsenides AFe_2As_2 ($a =$ Ba, sr, or ca). *Phys. Rev. B*, 81:193409, May 2010.

[228] Hiroshi Maeda, Yoshiaki Tanaka, Masao Fukutomi, and Toshihisa Asano. A new high- t c oxide superconductor without a rare earth element. *Japanese Journal of Applied Physics*, 27(2A):L209, 1988.

[229] S.L. Tomlinson, A.N. Farley, S.R. Hoon, and M.S. Valera. Interactions between soft magnetic samples and mfm tips. *Journal of Magnetism and Magnetic Materials*, 157:557 – 558, 1996. European Magnetic Materials and Applications Conference.

[230] L. Luan. *MagneticForce Microscopy studies of unconventional superconductors: single vortex manipulation and magnetic penetration depth measurements*. PhD thesis, StandfordUniversity, 2011.

[231] A. M. Chang, H. D. Hallen, L. Harriott, H. F. Hess, H. L. Kao, J. Kwo, R. E. Miller, R. Wolfe, J. van der Ziel, and T. Y. Chang. Scanning hall probe microscopy. *Applied Physics Letters*, 61(16):1974–1976, 1992.

[232] A. Wadas, O. Fritz, H. J. Hug, and H. J. Güntherodt. Magnetic force microscopy signal of flux line above a semi-infinite type ii-superconductor. *Zeitschrift für Physik B Condensed Matter*, 88(3):317–320, Oct 1992.

[233] L Ozyuzer, Y Simsek, H Koseoglu, F Turkoglu, C Kurter, U Welp, A E Koshelev, K E Gray, W K Kwok, T Yamamoto, K Kadowaki, Y Koval, H B Wang, and P MÃijller. Terahertz wave emission from intrinsic josephson junctions in high- t c superconductors. *Superconductor Science and Technology*, 22(11):114009, 2009.

[234] H. Murakami and R. Aoki. Lt-stm/sts observation on different atomic laybers of bscco (2212). *Journal of Physics and Chemistry of Solids*, 56(12):1807 – 1808, 1995. Proceedings of the Conference on Spectroscopies in Novel Superconductors.

[235] S. H. Pan, E. W. Hudson, J. Ma, and J. C. Davis. Imaging and identification of atomic planes of cleaved $Bi_2Sr_2CaCu_2O_{8+\delta}$ by high resolution scanning tunneling microscopy. *Applied Physics Letters*, 73(1):58–60, 1998.

[236] M. Nideröst, R. Frassanito, M. Saalfrank, A. C. Mota, G. Blatter, V. N. Zavaritsky, T. W. Li, and P. H. Kes. Lower critical field h_{c1} and barriers for vortex entry in $bi_2sr_2cacu_2O_{8+\delta}$ crystals. *Phys. Rev. Lett.*, 81:3231–3234, Oct 1998.

[237] R. Cubitt, E. M. Forgan, G. Yang, S. L. Lee, D. McK Paul, H. A. Mook, M. Yethiraj, P. H. Kes, T. W. Li, A. A. Menovsky, Z. Tarnawski, and K. Mortensen. Direct observation of magnetic flux lattice melting and decomposition in the high-tc superconductor bi2.15sr1.95cacu2o8+x. *Nature*, 365(6445):407–411, Sep 1993.

[238] B. Khaykovich, E. Zeldov, D. Majer, T. W. Li, P. H. Kes, and M. Konczykowski. Vortex-lattice phase transitions in $Bi_2Sr_2CaCu_2O_8$ crystals with different oxygen stoichiometry. *Phys. Rev. Lett.*, 76:2555–2558, Apr 1996.

[239] A. Oral, J. C. Barnard, S. J. Bending, I. I. Kaya, S. Ooi, T. Tamegai, and M. Henini. Direct observation of melting of the vortex solid in $Bi_2Sr_2CaCu_2o_{8+\delta}$ single crystals. *Phys. Rev. Lett.*, 80:3610–3613, Apr 1998.

[240] L. Embon, Y. Anahory, A. Suhov, D. Halbertal, J. Cuppens, A. Yakovenko, A. Uri, Y. Myasoedov, M. L. Rappaport, M. E. Huber, A. Gurevich, and E. Zeldov. Probing dynamics and pinning of single vortices in superconductors at nanometer scales. *Scientific Reports*, 5:7598 EP –, Jan 2015. Article.

[241] Th. Kebe and A. Carl. Calibration of magnetic force microscopy tips by using nanoscale current-carrying parallel wires. *Journal of Applied Physics*, 95(3):775–792, 2004.

[242] A. N. Grigorenko, S. J. Bending, A. E. Koshelev, John R. Clem, T. Tamegai,

and S. Ooi. Visualization of interacting crossing vortex lattices in the presence of quenched disorder. *Phys. Rev. Lett.*, 89:217003, Nov 2002.

[243] V. Vlasko-Vlasov, A. Koshelev, A. Glatz, C. Phillips, U. Welp, and W. Kwok. Flux cutting in high-T_c superconductors. *Phys. Rev. B*, 91:014516, Jan 2015.

[244] A. Glatz, V. K. Vlasko-Vlasov, W. K. Kwok, and G. W. Crabtree. Vortex cutting in superconductors. *Phys. Rev. B*, 94:064505, Aug 2016.

[245] E. Zeldov, A. I. Larkin, V. B. Geshkenbein, M. Konczykowski, D. Majer, B. Khaykovich, V. M. Vinokur, and H. Shtrikman. Geometrical barriers in high-temperature superconductors. *Phys. Rev. Lett.*, 73:1428–1431, Sep 1994.

[246] M.V. Indenbom, H. Kronmuller, T.W. Li, P.H. Kes, and A.A. Menovsky. Equilibrium magnetic properties and meissner expulsion of magnetic flux in bi2sr2cacu2ox single crystals. *Physica C: Superconductivity*, 222(3):203 – 211, 1994.

[247] M. Benkraouda and John R. Clem. Magnetic hysteresis from the geometrical barrier in type-ii superconducting strips. *Phys. Rev. B*, 53:5716–5726, Mar 1996.

[248] Ernst Helmut Brandt. Irreversible magnetization of pin-free type-ii superconductors. *Phys. Rev. B*, 60:11939–11942, Nov 1999.

[249] Ernst Helmut Brandt. Geometric barrier and current string in type-ii superconductors obtained from continuum electrodynamics. *Phys. Rev. B*, 59:3369–3372, Feb 1999.

[250] Th. Schuster, M. V. Indenbom, H. Kuhn, E. H. Brandt, and M. Konczykowski. Flux penetration and overcritical currents in flat superconductors with irradiation-enhanced edge pinning: Theory and experiment. *Phys. Rev. Lett.*, 73:1424–1427, Sep 1994.

[251] John R. Clem. Geometrical barriers and the growth of flux domes in thin ideal superconducting disks. *Journal of Superconductivity and Novel Magnetism*, 21(6):343–352, Oct 2008.

[252] Y. Segev, I. Gutman, S. Goldberg, Y. Myasoedov, E. Zeldov, E. H. Brandt, G. P. Mikitik, T. Katagiri, and T. Sasagawa. Suppression of geometrical bar-

rier in $Bi_2Sr_2CaCu_2O_{8+\delta}$ crystals by josephson vortex stacks. *Phys. Rev. B*, 83:104520, Mar 2011.

CHAPTER 8

Publications

2015 E. Herrera, I. Guillamón, J.A. Galvis, A. Correa-Orellana, A. Fente, R.F. Luccas, F.J. Mompean, M. Garcia-Hernandez, S. Vieira, J.P. Brison, H. Suderow, *Magnetic field dependence of the density of states in the multiband superconductor* β-Bi_2Pd **Phys. Rev. B 92, 054507**

2015 R. F. Luccas, A. Fente, J. Hanko, A. Correa-Orellana, E. Herrera, E. Climent-Pascual, J. Azpeitia, T. Perez, M. R. Osorio, E. Salas-Colera, N. M. Nemes, F. J. Mompeán, M. García- Hernández, J. G. Rodrigo,M. A. Ramos I. Guillamón S. Vieira. *Charge density wave in layered* $La_xCe_{1-x}Sb_2$, **Phys. Rev. B 92, 235153**.

2016 J. Kacmarcik, Z. Pribulova, T. Samuely, P. Szabo, V. Cambel, J. Soltys, E. Herrera, H. Suderow, A. Correa-Orellana, D. Prabhakaran, P. Samuely. *Single gap superconductivity in* β-Bi_2Pd **Phys Rev. B 93, 144502**.

2017 E. Herrera, I. Guillamón, J. A. Galvis, A. Correa-Orellana, A. Fente, S. Vieira, H. Suderow, A. Yu. Martynovich, and V. G. Kogan. *Influence of stray magnetic fields in the intervortex interaction in superconductors for magnetic fields nearly parallel to the surface.* **Accepted at Phys Rev. B**

2017 A. Fente, A. Correa-Orellana, A. Bohmer, A. Kreyssig, S. Ran, S. L. Budko, P. C. Canfield, F. Mompeán, M. García-Hernández, C. Munuera, I. Guillamón and H. Suderow. *Direct visualization of phase separation between superconducting and ne-*

matic domains in Co-doped $CaFe_2As_2$ close to a first order quantum phase transition, **Accepted at Phys Rev. B**

A.Correa-Orellana, R.F. Luccas, J. Azpeitia, E. Herrera, F. J. Mompeán, M. García-Hernández, I. Guillamón, C. Munuera, H. Suderow, L. Embon, E. Zeldov, Y. Anahory. *From vortex clusters to the vortex lattice in the low Îž superconductor β-Bi_2Pd*, **in preparation**

A.Correa-Orellana, C. Munuera, F. J. Mompean, M. García-Hernández, I. Guillamón, H. Suderow, K Kadowaki. *Manipulation of Pancake and Josephson vortices in $BiSr_2CaCu_2O_8$*, **in preparation**

R. F. Luccas, A. Correa-Orellana, F. J. Mompeán, M. García-Hernández and H. Suderow. *Magnetic phase diagram in single crystals of the noncollinear antiferromagnet Mn_5Si_3*, **in preparation**